Localization of ultracold atoms in quasi-periodic optical lattices

Henrik Lüschen

München, 2017

Localization of ultracold atoms in quasi-periodic optical lattices

Dissertation
an der Fakultät für Physik
der Ludwig-Maximilians-Universität
München

vorgelegt von
Henrik Lüschen
aus Stuttgart

München, 19. Dezember 2017

Zusammenfassung

Ein hoch angeregtes Vielteilchensystem relaxiert normalerweise in einen Gleichgewichtszustand, in dem alle Observablen ihre thermischen Werte annehmen. Das Verhalten des Systems wird dann effektiv klassisch. Dieses Verhalten, bekannt als Thermalisierung, tritt in fast allen Systemen auf. Bekannte Ausnahmen sind integrierbare Systeme, bei denen eine extensive Anzahl von Erhaltungsgrößen die Dynamik einschränkt, und Vielteilchenlokalisierung, die in nicht-periodischen Potenzialen auftritt.

Diese Arbeit befasst sich mit Experimenten zur Lokalisierung von ^{40}K-Atomen in einem quasiperiodischen optischen Gitter. Mithilfe von Messungen der Ausdehnung der Atomwolke, sowie dem Zerfall eines mikroskopischen Dichtemusters im Anfangszustand, charakterisieren wir zunächst das Verhalten einzelner Teilchen in unserem quasiperiodischen Potenzial. Unsere Messungen zeigen, dass sich individuelle Teilchen von einer ausreichend starken Quasiperiodizität lokalisieren lassen. Wir finden ein Parameterregime, in dem sich das System durch den Aubry-André Hamiltonoperator beschreiben lässt. Außerhalb dieses Regimes können delokalisierte und lokalisierte Zustände, getrennt von einer Mobilitätskante, koexistieren. Des Weiteren untersuchen wir das Verhalten von Vielteilchensystemen und zeigen, dass die Lokalisierung auch in der Gegenwart von Wechselwirkungen zwischen den Teilchen bestehen bleiben kann. Wir studieren die Dynamik in der Nähe des Phasenübergangs und leiten daraus eine untere Grenze für die kritische Stärke des quasiperiodischen Potenzials ab. Zusätzlich wird ein neu entwickeltes Verfahren zur Implementierung eines gut kontrollierbaren externen Bades vorgestellt. Dieses Bad wird verwendet, um Vielteilchenlokalisierung in offenen Systemen zu erforschen.

Abstract

The long-time dynamics of a highly excited many-body system typically bring it into an equilibrium state, where observables take their thermal values and its behavior becomes effectively classical. This thermalizing behavior is generic in the sense that it occurs in almost all systems with only two major exceptions: integrable systems, where an extensive amount of conserved quantities restrict the dynamics, and many-body localized systems, where non-periodic changes of local potentials result in a non-ergodic behavior.

In this thesis, we report on experiments investigating the localization of ^{40}K atoms in a quasi-periodic optical lattice. Using the global expansion of the cloud and the decay of an initially imprinted microscopic density pattern, we first characterize the behavior of single particles in the quasi-periodic potential, finding localization if the quasi-periodic detuning is sufficiently strong. We distinguish parameter regimes where a single-particle mobility edge is present from regimes where the system is well described by the Aubry-André Hamiltonian, which does not exhibit a single-particle mobility edge. Further, we investigate the behavior of the many-body systems, showing that localization can persist in the presence of interactions. We present a detailed study of the dynamics close to the many-body localization phase transition and derive a lower bound on the critical detuning strength. Additionally, a newly developed method to implement a controllable external bath to the system via scattering of near-resonant photons is applied to the many-body localized system.

Contents

Introduction

There are two vastly different approaches to studying quantum-mechanical many-body systems. One approach focuses on properties of the ground state, while the other investigates dynamics in highly excited states. Close to the ground state, the low energy properties of condensed matter systems are studied in thermal equilibrium and phases of matter are classified via e.g. spontaneous symmetry breaking [1], where the ground state breaks a symmetry of the underlying Hamiltonian when the system is driven across a phase transition. Popular examples include the transition of a metal into a ferromagnet below the Curie temperature, where the direction of the magnetization is chosen spontaneously, as well as the condensation of Bosons into a macroscopic matter wave which spontaneously chooses a phase. Such low energy phases host many intriguing quantum phenomena, such as superfluidity [2, 3] and superconductivity [4, 5], and have been the subject of intense research. Also, quantum phase transitions, such as the superfluid to Mott-insulator transition [6], have received a vast amount of attention. Here, the phase of a system changes as a Hamiltonian parameter is tuned at zero temperature.

At elevated temperatures, however, spontaneously broken symmetries are forbidden via the Mermin-Wagner theorem [7–9], at least in lower dimensions. Here, research focuses on the out-of-equilibrium dynamics ensuing after a quantum quench, i.e. a sudden change of a Hamiltonian parameter. In a generic many-body system, the expectation is that such dynamics will result in the full thermalization of the system [10–12], yielding an equilibrium state that can effectively be described by classical statistical mechanics. While local equilibrium is usually achieved after only few collisions, slow relaxation of hydrodynamic tails of globally conserved quantities typically continues to much longer times [13]. However, the basic ingredients necessary for a thermalizing behavior, i.e. a quantum mechanical equivalent of dynamical chaos [14, 15], are yet to be understood in quantum mechanics. Following the current understanding, the dynamics after a quench are indeed not at the core of thermalization, which rather occurs on the level of individual eigenstates. This notion is known as the *Eigenstate Thermalization Hypothesis* [16, 17] (ETH), which states that individual eigenstates are thermal themselves. Just after a quench, coherences between eigenstates hide their thermal nature. In the ensuing time evolution, however, local degrees of freedom become entangled with the rest of the system and hence proper-

ties of the initial state become non-retrievable for local observables, which therefore take their (classical) thermal values.

Experiments have already demonstrated, that these ideas are not true for all many-body systems. Especially, it was shown that an array of interacting Bose gases does not equilibrate in one dimension [18]. This is explained by the presence of an extensive set of conserved quantities, making the system integrable and preventing the relaxation to thermal equilibrium. It is clear though, that integrability cannot be seen as a generic alternative to thermalization, as it appears only in a small range of fine-tuned systems. Small changes, which break the integrability, result in a thermalizing behavior.

Recently, a more generic alternative to thermalization has been found in disordered systems, where single particles are Anderson localized [19–21]. In Anderson localized systems, interferences from wavefunction reflections off the disorder pattern result in an exponential localization of the single-particle wavefunctions, already at infinitesimal strengths of the disorder pattern in one dimension. The generalization of this phenomenon to interacting systems is known as *Many-Body Localization* (MBL) [22–24]. In the MBL phase, eigenstates violate the ETH and out-of-equilibrium dynamics after a quench do not result in a thermal state with an effective classical description. Instead, a full quantum description is necessary to describe the time evolution of the system up to infinite times. Key properties of the MBL phase, such as a logarithmic growth of the entanglement entropy after a quench, can be derived from a picture of 'emergent integrability' [25–27], which describes the MBL phase using an extensive number of local integrals of motion. Due to the localization of excitations, the MBL phase is a candidate for quantum memories and can also prevent the thermalization of phases typically only occurring in the ground state, a phenomenon known as 'localization protected order' [28–33]. Recent reviews on the MBL phase can be found in Refs [34, 35]. Apart from the MBL phase itself, the transition between the thermal and the MBL phase is of considerable interest [36–38]. The transition is fundamentally distinct from conventional quantum phase transitions, as it occurs not only in the ground state but over a broad range of energy densities. Instead, it is a novel type of eigenstate phase transition, where the eigenstates themselves change from obeying to violating the ETH in a singular manner [28, 33]. Numerical investigations of the phase transition are difficult, as the possible existence of increasingly large Griffiths regions, small inclusions that are locally in the other phase, prevent access to the universal scaling regime in simulations of small systems [39–41].

Other than in disordered systems, MBL can also occur in quasi-periodic geometries [42–44], where single particle eigenstates become exponentially localized above a finite critical strength of the quasi-periodic detuning [45–47]. While MBL is traditionally studied in random systems, recently quasi-periodic systems have received an increase of interest as numerical investigations of the localization transition promise to be more feasible due to the a-priori absence of Griffiths regions in the deterministic potentials [41, 48]. Quasi-periodic models further allow for the construction of single-particle mobility edges [49, 50], which enable localization studies in more complex scenarios where only a part of the underlying single-particle system is localized [51–53].

While there is an immense amount of theoretical work on disordered systems in general, and specifically on MBL, experimental work is much rarer. The localization of single particles in random potentials has been explored in a multitude of settings [54–56] including cold-gases [21, 57, 58], where quasi-periodic single-particle localization was also observed [47]. In the presence of interactions, initial experiments mostly focused on disorder driven transitions in the ground state [59–62]. Initial results on a finite temperature insulator were reported in Refs. [62, 63]. Only recently, however, did experiments give convincing evidence for localization at high energy densities in cold-gases experiments [43, 64] and ion traps [65]. Further, an experiment with NV-centers reported critical thermalization [66] and signatures of MBL were found in systems of nuclear spins [67] and superconducting qubits [68].

Experimental efforts in observing MBL are usually hindered by the presence of (small) couplings to external baths [69, 70] (via. e.g. particle loss or scattering of photons) which are unavoidable in practical situations. Such couplings generally result in a full thermalization of the open system [71, 72] on a timescale proportional to the inverse of the coupling rate. This limits the observation of MBL features to intermediate timescales, similarly to how finite temperatures limit the study of quantum effects of the ground states [73]. Strong limitations against the realization of an MBL state exist in solid state materials, where the presence of phonons generally results in rapid thermalization [74]. The effects of couplings to thermal systems are also studied in the context of small baths [75, 76], i.e. extended systems with only a few degrees of freedom. These studies are e.g. relevant in the context of possible Griffiths regions and their potential role in destabilizing MBL in higher dimensions [77, 78], as well as the question of the existence of a many-body mobility edge [79, 80].

In this thesis, localization will be investigated experimentally in the setting of ultra-cold atoms in optical lattices. Such systems are routinely used to study condensed matter problems in a controlled environment [81, 82], thereby implementing Feynman's idea of a quantum simulator [83]. They rely on loading either a Bose-Einstein condensate [84–86] or a Fermi-sea [87–89] into an optical standing wave, called an optical lattice [90]. Atoms trapped in such a periodic potential can be well described by Hubbard Hamiltonians [91], which characterize the system via a hopping rate between neighboring potential wells, as well as an on-site interaction term. Varying lattice geometries allow for the implementation of a multitude of different models [47, 92–96]. Via the lattice depth, the strength of the tunnel coupling can be accurately controlled, and even phases can be imprinted [97, 98]. The on-site interactions can be adjusted via a Feshbach resonance [99, 100]. Cold gases in optical lattices thus provide an exceptional control over a defect-free implementation of condensed matter Hamiltonians, which even extends to the level of individual atoms [101]. They have not only been extensively used to investigate ground states, e.g. Mott-insulators [6, 102, 103], but have also proven well suited for probing out-of-equilibrium dynamics of excited states [18, 104–106]. Thus, cold gases are an ideal platform to study the localization of interacting particles in various geometries by employing dynamic observables. Additionally, cold gases systems provide the very good

isolation from their surroundings that is required for the creation of MBL states. Residual couplings to the environment can often be tuned experimentally [107], allowing for systematic studies of their effects.

Contents of this thesis: In this thesis, we experimentally study localization in quasi-periodic potentials in a cold-gases setting. We create the quasi-periodic potential via the superposition of two optical lattices with incommensurate wavelengths as in Ref. [47] and probe the properties of the system using measurements of its out-of-equilibrium dynamics. Specifically, we probe the relaxation of an initial charge-density wave state, as well as the expansion dynamics of the initially confined cloud. The thesis is divided into two parts: Part I focuses on the non-interacting system and part II on many-body localization.

In part I, **chapter 2**, we introduce the setup used for our experiments and establish connections to theoretical models studied in the context of single-particle localization. We also discuss differences between our quasi-periodic system and the more popular Anderson Hamiltonian with random disorder. We introduce the observables and discuss the experimental implementation of the used methods for state preparation and readout of the observables. In **chapter 3**, we show exemplary behavior of the employed observables in the quasi-periodic lattice. This data is then used to map out the full non-interacting phase diagram. We find a localized and an extended phase, which are separated by an intermediate phase where a single-particle mobility edge exists. We also identify a parameter regime where the intermediate phase vanishes and the experimental system accurately maps onto the Aubry-André (AA) Hamiltonian.

In part II, we study the localization of interacting particles (MBL) in the context of the AA-model. **Chapter 4** discusses the current understanding of highly excited systems, i.e. the expectation that the system will thermalize, in both classical and quantum mechanics. Many-body localization is introduced as the opposite of thermalization and its basic properties are briefly reviewed. The numerical and experimental challenges in investigating interacting systems as compared to non-interacting systems are discussed in **chapter 5**. Especially, we give a detailed characterization of the experimental initial state and show how changes in the initial state influence the system. Additionally, we show initial results on MBL in our experimental system which serve as a basis for the following chapters. **Chapter 6** focuses on the transition between the thermalizing and the MBL phase. We review the differences between typical quantum phase transitions and the MBL phase transition, as well as the current understanding of the MBL transition in disordered models. We then present a detailed analysis of the dynamical behavior of our observables to determine the MBL critical point. In the analysis of the dynamics, we find unexpected similarities to the case of random disorder. We discuss various ideas on the origins of these similarities. In **chapter 7**, we present a newly developed method for implementing controlled openness via the scattering of near-resonant photons in cold-gases setups, which can be used in a large variety of scenarios. We then employ this method to our MBL system and find a linear susceptibility of the localized system to the photon bath. Finally, in **chapter 8**, we summarize the presented results and give an outlook on the prospects of

studying interaction effects in a regime of our quasi-period lattice, where a single-particle intermediate phase is present.

Publications: The main results described in this thesis are published in the following papers:

- Michael Schreiber, Sean S. Hodgman, Pranjal Bordia, **Henrik P. Lüschen**, Mark H. Fischer, Ronen Vosk, Ehud Altman, Ulrich Schneider and Immanuel Bloch. **Observation of many-body localization of interacting fermions in a quasirandom optical lattice.**
  Science, 349(6250):842-845, 2015 [43]

- **Henrik P. Lüschen**, Pranjal Bordia, Sean S. Hodgman, Michael Schreiber, Saubhik Sarkar, Andrew Daley, Mark Fischer, Ehud Altman, Immanuel Bloch and Ulrich Schneider. **Signatures of Many-Body Localization in a Controlled Open Quantum System.**
  Physical Review X, 7, 011034, March 2017 [70]

- **Henrik P. Lüschen**, Pranjal Bordia, Sebastian Scherg, Fabien Alet, Ehud Altman, Ulrich Schneider and Immanuel Bloch. **Observation of Slow Dynamics near the Many-Body Localization Transition in One-Dimensional Quasi-Periodic Systems.**
  Physical Review Letters, 119:260401 Dec 2017 [108]

- **Henrik P. Lüschen**, Sebastian Scherg, Thomas Kohlert, Michael Schreiber, Pranjal Bordia, Xiao Li, S. Das Sarma and Immanuel Bloch. **Exploring the Single-Particle Mobility Edge in a One-Dimensional Quasiperiodic Optical Lattice**.
  Preprint on ArXiv:1709.03478 [109]

Additionally, I contributed to the following publications which are not described in this thesis:

- Pranjal Bordia, **Henrik P. Lüschen**, Sean S. Hodgman, Michael Schreiber, Immanuel Bloch and Ulrich Schneider. **Coupling identical one-dimensional many-body localized systems.**
  Physical Review Letters, 116:140401, Apr 2016 [69]

- Pranjal Bordia, **Henrik P. Lüschen**, Ulrich Schneider, Michael Knap and Immanuel Bloch. **Periodically driving a many-body localized quantum system.**
  Nature Physics (2017) [110]

- Pranjal Bordia, **Henrik P. Lüschen**, Sebastian Scherg, Sarang Gopalakrishnan, Michael Knap, Ulrich Schneider and Immanuel Bloch. **Probing Slow Relaxation and Many-Body Localization in Two-Dimensional Quasi-Periodic Systems.**
  Physical Review X, 7, 041047, November 2017 [111]

Part I

Single-particle localization

Experimental setup and theoretical models

In this chapter, we will introduce the experimental apparatus used to perform the presented experiments. Especially, we will discuss the implementation of the quasi-periodic potential and distinguish it from randomly disordered systems. We will show to what extent the experimental system implements the well known Aubry-André model and present the observables used to experimentally probe for localization.

2.1 Quasi-periodicity

Since Anderson's discovery that single particles localize in random potentials [19], localization phenomena are most commonly studied in systems with uncorrelated potential landscapes. In such systems, the potential at a certain location $\mathbf{x}$ does not give any information on the potential at any other location in the system, as correlations are absent on both long and short length scales. However, this randomness is not necessary for the localization of particles, which can also occur in quasi-periodic potentials [46]. In contrast to randomly disordered systems, quasi-periodic systems do show a certain amount of recurrence, without actually being periodic. While a periodic function $p(t)$ will have the same value after a full period T, i.e. $p(t) = p(t+T)$, a quasi-periodic function $qp(t)$ is only

| Quasi-Periodic | Random |
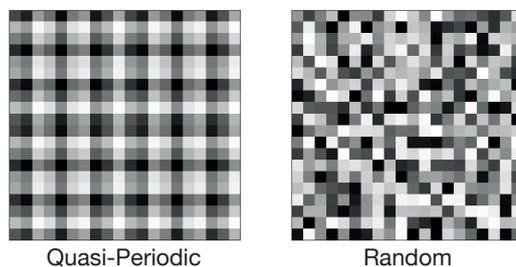
Figure 2.1: Quasi-periodic geometry: Comparison of a discrete quasi-periodic versus a random pattern. The quasi-periodic pattern is generated as a superposition of two incommensurate frequencies along the two directions with incommensurable ratios of ~ 1.4. A two-dimensional pattern was chosen for a better visualization.

almost periodic in a sense that it approximately retains its value after a quasi-period, i.e. $qp(t) \approx qp(t + T)$.

Typically, quasi-periodic functions are characterizable by a finite number of one or more frequencies, e.g.

$$qp(t) = \sum_{i=2}^{i<\infty} cos(\omega_i t) \tag{2.1}$$

where the most basic example is the superposition of two frequencies ω_1 and ω_2. This will result in a quasi-periodic function, as long as the two frequencies are incommensurate, i.e. no relation $n\omega_1 = m\omega_2$ exists, with n, m being integers. Should such a relation exist, the resulting function would be periodic when $n \times m$ cycles of the faster frequency have passed. In the limit of an infinite number of contributing frequencies, the function would become random.

Quasi-periodic systems are distinctively different from randomly disordered systems, as is illustrated in Fig. 2.1. Here, a two-dimensional quasi-periodic pattern is compared to a random pattern. It is visible that the quasi-periodic pattern possesses a certain almost-regularity while the random pattern is fully uncorrelated. As a result of the lack of correlations, the random pattern can show statistically rare inclusions, where a small subregion is only very slightly, or even non-disordered. A similar effect in quasi-periodic patterns is not possible. This creates fundamental differences between localization in quasi-periodic and randomly disordered systems (see chapter 6), as the localization properties in random systems can change locally [41]. As in this thesis we will discuss and compare results from both kinds of systems, we will explicitly distinguish between random *disorder* and quasi-periodic *detuning* to emphasize the discussed type of potential pattern.

2.2   Experimental setup

In this section, we will give a brief introduction to the experimental setup. All experiments described in this thesis were performed using ultracold ^{40}K Potassium atoms in optical lattices. As the cooling of gases to quantum degeneracy has become a well established tool [84–89], the standard methods currently in use for cooling and trapping atoms will not be discussed in this thesis. However, the general sequence of the cooling and trapping of ^{40}K atoms in our setup will be briefly outlined and the optical setup introduced. A more detailed description of the apparatus and the sequence used for cooling the atoms can be found in previous Ph.D. theses performed on the same setup [112–115].

2.2.1   Creation of a degenerate gas of ^{40}K

Cooling: The cloud of ^{40}K atoms is cooled to quantum degeneracy using a multi-step process: Initially, the ^{40}K atoms are loaded together with a large cloud of bosonic ^{87}Rb atoms in a dual-species magneto-optical trap (MOT). Subsequently, forced evaporation is
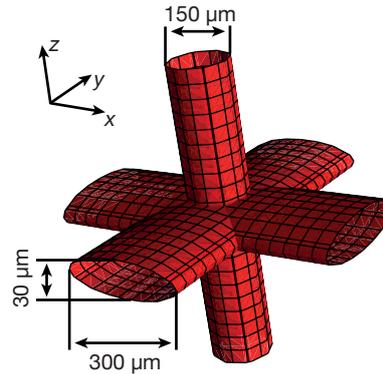
Figure 2.2: Dipole trap setup: Geometry of the three dipole beams employed to confine the atom cloud. The shown dimensions refer to the beam diameters.

performed on the ^{87}Rb atoms in an optically-plugged magnetic quadrupole trap to sympathetically cool the ^{40}K atoms. The final evaporative cooling steps are performed in a three-beam optical dipole trap [116]. At the end of the cooling procedure, only ^{40}K atoms remain, as the trap is too weak to hold the much heavier ^{87}Rb atoms against gravity. For the experiments described in this thesis, we generate clouds of typically $N = 10^5$ atoms of ^{40}K at a temperature of $T/T_F = 0.15$, where T_F is the Fermi temperature in the dipole trap. Both atom numbers and temperatures show fluctuations of about 10% between different runs of the experiment.

Spin composition of the atomic cloud: During sympathetic cooling, the fermionic cloud is prepared in its lowest hyperfine state $|F, m_F\rangle = |\frac{9}{2}, -\frac{9}{2}\rangle \equiv |\downarrow\rangle$. For a detailed summary of the properties of ^{40}K see Ref. [117]. Populations of unwanted spin states are selectively removed via Feshbach resonances [118] during the evaporative cooling in the dipole trap: Tuning the magnetic field to a Feshbach resonance between a specific hyperfine state and ^{87}Rb results in a strong loss of atoms in said hyperfine state due to three-body recombinations. This reduces the population of unwanted hyperfine states to below the imaging detection threshold ($\sim 1\%$ of atoms). A list of the resonances can be found in Ref. [119]. Afterwards, a mixture of the two lowest hyperfine states $|\downarrow\rangle$ and $|F, m_F\rangle = |\frac{9}{2}, -\frac{7}{2}\rangle \equiv |\uparrow\rangle$ can be created using a radio-frequency sweep. For the non-interacting experiments described in part I of this thesis, we load a spin-polarized gas, where all atoms are in the absolute ground state $|\downarrow\rangle$. Since fermionic atoms of the same spin cannot interact with each other at ultra-low temperatures, the spin-polarized configuration is fully non-interacting. For the interacting experiments in part II, we load an equal mixture of $|\downarrow\rangle$ and $|\uparrow\rangle$, where the interaction strength between the two spins can be tuned via a Feshbach resonance [100].

Dipole traps: To confine and support the atomic cloud versus gravity during the last cooling steps and the experiments, we employ three tightly focused red-detuned laser beams, commonly referred to as dipole traps. The geometry of the optical dipole traps is

presented in Fig. 2.2. It consists of three orthogonal beams, running along the spatial $\mathbf{x}, \mathbf{y}$ (horizontal) and $\mathbf{z}$ (vertical) direction respectively. All three beams have a wavelength of approximately 1064 nm and are created by Coherent's 'Mephisto MOPA' lasers. Orthogonal polarizations, as well as small detunings relative to each other, ensure that the beams do not interfere. Atoms are supported versus gravity by two beams traveling along the horizontal $\mathbf{x}$ and $\mathbf{y}$ direction. These beams are tightly focused in the vertical $\mathbf{z}$ direction with beam diameters of 33 μm, to minimize the influence of the gravitational potential on the experiments. However, they have large diameters of approximately 300 μm in the horizontal directions and hence, the horizontal trapping frequency is dominated by the vertically traveling dipole beam with a diameter of 150 μm.

2.2.2 Optical lattices

All optical lattices used in our setup are created by retro-reflected laserbeams, resulting in the formation of a standing wave pattern with period $\lambda/2$, where λ denotes the wavelength of the laser. We employ lattices at wavelengths of 738 nm, 1064 nm and 532 nm. The 738 nm laser light is generated by a Coherent Titanium-Sapphire 'MBR' laser system pumped by a Coherent 'Verdi-V18', generating approximately 4.5 W of laser light. The laser is locked to its internal reference cavity, achieving short-term linewidths on the order of ~ 1 MHz. The 1064 nm light is created by an NP Photonics 'Rock' laser source and amplified by a Nufern fiber amplifier. This setup can produce up to 45 W of power, however, usually the amplifier is running on a lower current resulting in only about 10 W output power, which vastly extends the lifetime of the amplifier. The 'Rock' laser source is locked to a stable reference cavity, achieving a linewidth of ~ 100 kHz. The 532 nm light is powered by another Coherent 'Verdi-V18', generating 18 W of laser light. This laser is locked relative to the 1064 nm light with a linewidth of ~ 1 MHz. Details of this lock are described in Ref. [114].

Most lattices (all except 1064 nm) are blue detuned relative to the atomic resonance frequency of ^{40}K. Blue detuned lattices have the advantage, that the Gaussian shape of the lattice beam does not create an additional confining potential on top of the dipole beams, but instead produces an anti-confinement. Due to this anti-confinement, different strengths of the dipole traps can create not only globally trapped but also anti-trapped and homogeneous potential landscapes [112, 120]. Especially the homogeneous case is important, as it is necessary for the expansion of atoms, which is one of the used observables (see section 2.4.2). In order to be able to compensate the anti-confinement of the lattices with the confinement of the dipole trap in the horizontal directions, the lattice beams have the same geometry as the vertical dipole trap, i.e. a beam diameter of 150 μm.

Another important aspect of the Gaussian shape of the lattice beams is, that atoms on the outer edge of the cloud experience slightly smaller lattice depths than those in the center. The cloud has a diameter of about 40 μm in the horizontal, and 12 μm in the vertical direction, resulting in a maximum deviation of the lattice depths of about 10 %.
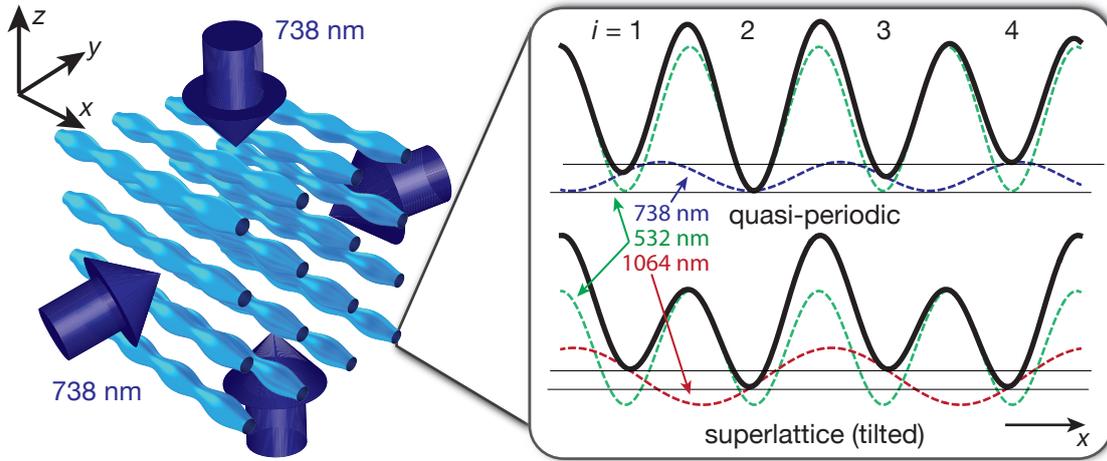
Figure 2.3: Optical lattice setup: The optical lattice setup consists of two deep 738 nm lattices along the orthogonal **y** and **z** directions, which split the system into an array of one-dimensional tubes. Along these tubes, the combination of the 532 nm 'primary' (green), 1064 nm 'long' (red) and 738 nm 'detuning' (purple) lattices can be used to create various geometries. Shown on top is the superposition of primary and detuning lattice, resulting in a quasi-periodic geometry, where on-site energies do not repeat. On the bottom, a tilted superlattice geometry is illustrated, as resulting from the superposition of primary and super-lattice. Here, every second site has the same energy.

One dimensional optical lattice: We employ optical lattices along all three spatial directions **x**, **y** and **z**. The experiments reported in this thesis are performed in a one-dimensional quasi-periodic structure which is generated parallel to the **x** direction. In order to achieve a one-dimensional behavior of the atoms in the three-dimensional cloud, we employ two deep lattices along the 'orthogonal' **y** and **z** directions, as is illustrated in Fig. 2.3. These lattices use 738 nm light and achieve depths of up to $45 E_r^{738\,\text{nm}}$, where $E_r^{\lambda} = h^2/2m\lambda^2$ denotes the recoil energy at a wavelength of λ with the mass m of ^{40}K and h being the Planck constant. At these depths, they effectively freeze the dynamics along the orthogonal directions, resulting in the creation of effectively one-dimensional 'tubes'. Note that the term 'one-dimensional optical lattice' is also often used to describe systems with optical lattices along only one direction, as in e.g. Ref. [47]. In such systems, one-dimensional behavior can also be studied, but only if the spatial directions are separable. As interactions break this separability, this limits experiments to single-particle physics.

The superlattice setup: Along the one-dimensional tubes which are generated as described above, we employ a superlattice setup, which enables us to differentially address even and odd sites. The superlattice consists of the 'primary' lattice at 532 nm and a 'long' lattice at 1064 nm. The lattices can achieve depths of up to $25 E_r^{532\,\text{nm}}$ and $\sim 100 E_r^{532\,\text{nm}}$, respectively. Due to the relative lock between the 532 nm and 1064 nm light, the phase between the two lattices is long-term stable. Since the optical lattices are required to have a node at the retro-reflection mirror, their relative phase at the position of the atoms is

set by the distance between mirror and atoms, as well as their wavelength. Hence, the relative phase of primary and long lattice at the position of the atoms can be controlled via small changes in the wavelength of, in our case, the primary lattice. This allows for the creation of arbitrarily tilted superlattice patterns [121, 122] by superimposing the long and primary lattice with different relative phases (see Fig. 2.3). Since the long lattice has exactly twice the wavelength of the primary lattice, these patterns will repeat every second site and are hence known as double-wells.

The quasi-periodic lattice: In addition to the 1064 nm lattice, the primary 532 nm lattice can also be superimposed with some 738 nm light, called the 'detuning' lattice. This creates a quasi-periodic pattern which explicitly does not repeat itself like the superlattice pattern. The detuning lattice is usually much weaker than the primary lattice and hence has only enough power for approximately $4 E_r^{738}$. Note that the primary and the detuning lattice are not locked relative to each other, and hence their relative phase is not long-term stable. Over the short times on which the experiments are performed, the passive stability is, however, good enough. Also, the relative phase can be actively changed via the frequency of the MBR. This can, however, not be done while the optical lattices are switched on since the orthogonal lattices along the **y** and **z** direction experience the same wavelength change and hence would move as well.

2.2.3   The quasi-periodic system

The system studied in this thesis is the one-dimensional, quasi-periodic lattice, created by the superposition of the primary 532 nm and the 738 nm detuning lattice. The behavior of atoms with mass m in this potential is described by the continuum Hamiltonian

$$\hat{H}_{\text{cont}} = -\frac{\hbar^2}{2m}\frac{d^2}{dx^2} + V_p \sin^2(k_p x) + V_d \sin^2(k_d x + \phi), \tag{2.2}$$

where the V_i ($i \in \{p, d\}$) are the strength of the primary and detuning lattice and the k_i denote the respective lattice's wavevector. As the primary and detuning lattices share a common retro-reflection mirror, their relative phase ϕ can be changed via slight changes of the wavelength of the detuning lattice.

In order to implement a quasi-periodic potential (as compared to a periodic potential) the two superimposed lattices need to have incommensurable wavelengths. This is typically characterized via the incommensurability

$$\beta = k_d / k_p. \tag{2.3}$$

The incommensurability will take an irrational value if the two wavelengths are incommensurate. Should β be rational, the above Hamiltonian describes a periodic system which can be easily solved to have extended Bloch waves as its eigenstates [123]. Hence, only irrational β are suitable for studying localization [124].

In our setup, the incommensurability is approximately $\beta \approx 0.72$. Note that the experimental β is definitely irrational, as the individual wavelengths of the two lattices are irrational themselves. As the experiment implements a finite-sized system, it would, however, be sufficient to require that there are no repeating patterns in the range that is populated by atoms. The finite-size characteristics of the system further require that experimental results are averaged over the detuning phase ϕ, to ensure that all possible realizations of the quasi-periodic pattern are probed. In the thermodynamic limit of infinite system size, the detuning phase would become irrelevant as all possible realizations of the quasi-periodic pattern occur in some part of the infinitely sized system.

2.3   Theoretical model systems

In theoretical studies of localization, continuum Hamiltonians as e.g. in eq. (2.2) are barely used. Instead, theoretical studies use model Hamiltonians typically formulated in a tight-binding description. There are two notable models that are most often used: the Anderson [19] and the Aubry-André (AA) model [46]. The by far most popular model is the Anderson Hamiltonian [19], where on-site energies are randomly distributed. Considering quasi-periodic models, the AA Hamiltonian [46] is the most popular choice. In this section, we will give a brief introduction to this model Hamiltonian and discuss how it corresponds to the experimentally implemented system.

Note that localization can occur in a much broader class of systems than the one-dimensional lattice models discussed in this thesis. This especially includes both higher dimensional systems [57, 58, 62, 66, 111, 125, 126], as well as non-lattice models [21].

In the literature, the term 'Anderson-localization' is often used to depict the single-particle (non-interacting) case in the context of both the Anderson and the AA model. Throughout this thesis, the focus will be on the AA model, but especially in the discussion of interacting systems (part II) also results obtained for the Anderson model will be used in the discussion. To avoid confusion, in this thesis the considered model will always be clearly stated.

2.3.1   The Aubry-André Hamiltonian

The Aubry-André Hamiltonian is a tight-binding lattice model with a quasi-periodic distribution of on-site energies. The Hamiltonian can be written as

$$\hat{H}_{AA} = -J \sum_{i,\sigma} \left(\hat{c}_{i,\sigma}^{\dagger} \hat{c}_{i+1,\sigma} + \text{h.c.} \right) + \Delta \sum_{i,\sigma} \cos(2\pi\beta i + \phi) \hat{n}_{i,\sigma}, \tag{2.4}$$

with the fermionic creation (annihilation) operators $\hat{c}_{i,\sigma}$ ($\hat{c}_{i,\sigma}^{\dagger}$) on lattice site with index i and spin $\sigma \in [\uparrow, \downarrow]$. The local density operator is $\hat{n}_i = \hat{c}_i^{\dagger} \hat{c}_i$. The first term depicts the usual hopping term between nearest neighbors with amplitude J that is commonly present in Hubbard models [91]. The second term denotes the quasi-periodic modulation of the

on-site energies with overall amplitude Δ, incommensurability β and relative phase ϕ. In the literature, Δ is often referred to as the 'disorder strength'. However, as was illustrated in Fig. 2.1, quasi-periodicity is distinctly different from randomness. Hence, in order to clearly separate the quasi-periodic AA model from models with actual randomness, in this thesis we will refer to Δ as the 'detuning strength'.

The Aubry-André Hamiltonian exhibits a localization transition at a finite detuning strength of $\Delta = 2J$, where all single-particle eigenstates simultaneously become localized. Here, we call an eigenstate $|\Phi_i(x)\rangle$ localized around x_0, if for every $\epsilon > 0$ one can find a distance $d > 0$ such that

$$|\Psi_i(x_0 \pm d)|^2 < \epsilon. \tag{2.5}$$

Intuitively, this means that the probability of finding a particle in eigenstate $|\Phi_i(x)\rangle$ has to go to zero far away from its center x_0. On the localized side of the AA model, the eigenstates are exponentially localized, i.e. they can be written as

$$|\Phi_i(x, x_0)\rangle = f(x, x_0) e^{-|x-x_0|/\lambda}, \tag{2.6}$$

where $f(x, x_0)$ is an arbitrary function and λ is called the localization length. This localization length is the same for all eigenstates and given by [46]

$$\lambda = \frac{1}{\ln\left(\frac{\Delta}{2J}\right)}. \tag{2.7}$$

The localization length is infinite in the extended phase and at the transition. Above the transition it rapidly decreases with increasing Δ to below one lattice site.

As in the experimental quasi-periodic lattice, a crucial condition for localization in the AA model is the irrationality of the incommensurable ratio β. Should β be rational, the second term in eq. (2.4) will become periodic on long distances, and hence the system will be delocalized at all Δ in the infinite size limit. Again, in finite-sized systems, it is sufficient to choose β such that the period is larger than the system size and results need to be averaged over the relative phase ϕ.

Experimentally, localization in the Aubry-André model has been studied both in optical lattices [43, 47], as well as with light waves in photonic lattices [55].

2.3.2   Mapping of the experimental lattice to the Aubry-André Hamiltonian

In this section, we will discuss in what sense the experimental system is an implementation of the AA model. We will show the mathematical mapping between the two models and discuss the approximations that are made. This will allow us to find parameter regimes in which the experimental system accurately maps to the Aubry-André model. The accuracy of the mapping is also experimentally investigated in section 3.3.

We start from the continuum description of the quasi-periodic optical lattice

$$\hat{H}_{\text{cont}} = -\frac{\hbar^2}{2m}\frac{d^2}{dx^2} + V_p \sin^2(k_p x) + V_d \sin^2(k_d x + \phi), \tag{2.8}$$

where the V_i ($i \in \{p, d\}$) are the strength of the primary and detuning lattice, the k_i denote the respective lattice's wavevector and ϕ the relative phase between the two lattices. The mapping to the Aubry-André Hamiltonian is performed (following Ref. [127]) by expanding this continuum Hamiltonian in the Wannier basis of the lowest band [128, 129] of the primary lattice:

$$\hat{H} = \sum_{i,j} |w_i\rangle \langle w_i|\hat{H}|w_j\rangle \langle w_j|. \tag{2.9}$$

Here $|w_j\rangle$ labels the Wannier state maximally localized around the lattice site with index j. Note that the Wannier states of the primary lattice used here are only a meaningful basis in the presence of a weak detuning lattice. Should the detuning lattice be similarly strong as the primary lattice, the Wannier states of the system would differ significantly. However, the expansion in this basis still remains valid, as long as sufficiently high order terms are considered.

For the derivation of the matrix elements $\langle w_i|\hat{H}|w_j\rangle$, it is convenient to write the Hamiltonian in terms of the recoil energy $E_r^p = \hbar^2 k_p^2 / 2m$ of the primary lattice and to change coordinates to $\xi = k_p x$, yielding

$$\frac{\hat{H}_{\text{cont}}}{E_r^p} = -\nabla_\xi^2 + \frac{V_p}{E_r^p} \sin^2(\xi) + \frac{V_d \beta^2}{E_r^p} \sin^2(\beta\xi + \phi)$$
$$= \hat{H}_0 + \frac{V_d \beta^2}{E_r^p} \sin^2(\beta\xi + \phi), \tag{2.10}$$

where $\hat{H}_0$ is the continuum Hamiltonian of the periodic system (the system in the absence of the detuning lattice).

Tight-binding limit: We will first evaluate the Wannier expansion in the tight-binding limit of a deep primary lattice weakly perturbed by the detuning lattice. In this limit, it is sufficient to consider the overlap of nearest-neighbor Wannier functions with the periodic Hamiltonian to obtain the standard hopping term of Hubbard-models J [90] and the on-site contribution of the detuning lattice [130, 131] to compute the matrix elements

$$\langle w_i|\hat{H}|w_j\rangle \approx -J\delta_{i,j\pm1} + \delta_{i,j} \frac{V_d \beta^2}{E_r^p} \langle w_i|\sin^2(\beta\xi + \phi)|w_j\rangle. \tag{2.11}$$

On-site contributions of the periodic Hamiltonian $\langle w_i|\hat{H}_0|w_i\rangle$ give constant terms that can be neglected by choosing an appropriate energy offset. Corrections to the nearest-neighbor hopping J due to the detuning lattice $\sim \langle w_i|\sin^2(\beta\xi + \phi)|w_{i\pm1}\rangle$ tend to be small compared to J [131], just as any terms beyond the nearest neighbors.

Equation 2.11 can be further simplified (see Ref. [127]) to read

$$\langle w_i|\hat{H}|w_j\rangle \approx -J\delta_{i,j\pm1} + \delta_{i,j}\Delta\cos(2\pi\beta i + \phi') \tag{2.12}$$

with the detuning strength

$$\Delta = \frac{V_d \beta^2}{2E_r^p} \langle w_0|\cos(2\beta\xi)|w_0\rangle. \tag{2.13}$$
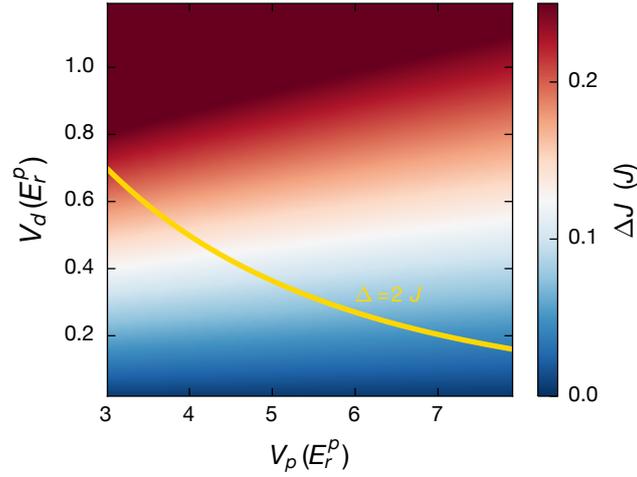
Figure 2.4: Applicability of the Aubry-André model: Corrections to the nearest-neighbor hopping ΔJ as a function of the primary and detuning lattice strengths V_p and V_d. Note that both lattice depths are given in units of the recoil energy of the primary lattice E_r^p. The yellow line marks the location where the transition would be located in a pure Aubry-André description, i.e. where $\Delta = 2\,J$.

Writing the resulting, simplified Hamiltonian in the form of a tight-binding model gives the AA model in equ. (2.4).

Beyond the tight-binding limit: Outside of the tight-binding limit, the nearest-neighbor approximation is no longer valid and higher order terms need to be considered. Dominant corrections come from variations in the nearest-neighbor tunneling rate due to the detuning lattice given by

$$\Delta J = \frac{V_d \beta^2}{2 E_r^p} \langle w_0 | \cos(2\beta\xi) | w_1 \rangle \tag{2.14}$$

and next-to-nearest-neighbor hopping terms

$$J_1 = \langle w_i | \hat{H}_0 | w_{i\pm2} \rangle. \tag{2.15}$$

This gives rise to the additional Hamiltonian terms

$$\hat{H} = \hat{H}_{\mathrm{AA}} + J_1 \sum_{i,\sigma} \left(\hat{c}_{i,\sigma}^\dagger \hat{c}_{i+2,\sigma} + \mathrm{h.c.} \right) + \Delta J \sum_{i,\sigma} \cos\left(2\pi\beta \left(i + \frac{1}{2} \right) + \phi \right) \left(\hat{c}_{i,\sigma}^\dagger \hat{c}_{i+1,\sigma} + \mathrm{h.c.} \right). \tag{2.16}$$

Note that the expansion of the continuum Hamiltonian to the Wannier basis is also valid in this regime, only the restriction to nearest-neighbor terms is no longer possible.

To assess the range in which the Aubry-André Hamiltonian gives a valid description of the bichromatic lattice, Fig. 2.4 shows the corrections to the nearest-neighbor tunneling ΔJ as a function of V_d and V_p. The figure also illustrates the location of the non-interacting phase transition (at $\Delta = 2J$) in a pure Aubry-André description via the yellow line. As expected, ΔJ shows a strong increase with the depth of the detuning lattice, as well as a
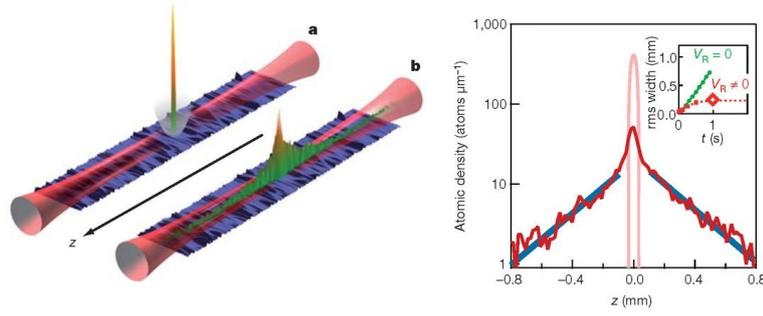
Figure 2.5: Exponential localization: Releasing an initially strongly confined Bose-Einstein condensate (a) into a speckle pattern reveals the exponential localization (b). The static density distribution of the localized state is shown on the right. Blue lines are exponential fits to the tails of the distribution. Figure reused from Ref. [21] with permission. Copyrighted by Springer Nature.

slight tendency to increase at lower strengths of the primary lattice. Whether a description by the Aubry-André model is valid or not, however, is mostly given by the location of the localization transition, which moves to lower depths of the detuning lattice if the primary lattice depth is increased. At e.g. a primary lattice depth of $V_p = 8 E_r^p$, a ratio of $\Delta J/J \approx 4\%$ is present at the phase transition. At weaker primary lattice depths, however, the correction terms are already much more significant at the transition. Note that in principle the mapping between the two systems becomes more accurate the deeper the primary lattice is. In practice, however, choosing arbitrarily deep primary lattice depths is not possible, as the hopping timescale in the primary lattice $\tau = \hbar/J$ becomes too large.

2.3.3 The Anderson Hamiltonian

While in this thesis localization is studied in quasi-periodic systems, the most famous model system for localization is the Anderson model. As we will be using theoretical results obtained from the Anderson Hamiltonian in the discussion of our results, a brief introduction to the model will be given here.

In 1958, Anderson first showed the absence of diffusion in certain random lattices [19]. The typical lattice Hamiltonian studied in this context reads

$$\hat{H} = -J \sum_{i,\sigma} \left(\hat{c}_{i,\sigma}^{\dagger} \hat{c}_{i+1,\sigma} + \text{h.c.} \right) + \Delta \sum_{i} V_i \hat{n}_{i,\sigma}. \tag{2.17}$$

As in the AA model, the first term depicts the usual hopping term between nearest neighbors with amplitude J that is commonly present in Hubbard models [91]. The second term depicts the disorder potential with global amplitude Δ and a random distribution of the $V_i \in [-1, 1]$, which are usually drawn from a box distribution. Note that in the Anderson model we will refer to Δ as the disorder strength.

The Anderson model shows a transition from all eigenstates being spatially extended Bloch waves at $\Delta = 0$ to all eigenstates being localized at infinitesimally small disorder strengths $\Delta > 0$. In contrast to the AA model, its localization transition thus does not occur

at a finite disorder strength. Similarly to the AA model, the localized eigenstates show exponential localization, as was directly experimentally observed in Ref. [21]. As shown in Fig. 2.5, releasing an initially tightly confined Bose-Einstein condensate into a waveguide in the presence of a speckle pattern, and waiting for the system to equilibrate, reveals the exponential envelope of the particle density and allows for a direct measurement of the localization length. Note that this experiment was not performed in an optical lattice, but instead in a continuum system, where Anderson localization also occurs. An experimental realization of a randomly disordered two-dimensional lattice system was presented in Ref. [64].

The mechanism underlying Anderson localization is that of waves being reflected from (small) potential barriers. These reflections interfere destructively traveling forward, but constructively backward, resulting in the localization of the wavefunction. Accordingly, Anderson localization has also been observed in classical wave-mechanic systems (see e.g. [54, 132] and references therein). Considering the localization of particles, however, it is a purely quantum effect, as classical trajectories of high energy states would be delocalized.

2.4   Observables

To characterize the quasi-periodic system, two complementary observables are employed. The density imbalance $\mathcal{I}$ between even and odd sites sensitively captures the presence of localized states based on the decay of an initially imprinted charge-density wave. The global expansion $\mathcal{E}$ probes for localization in the most intuitive manner, as it is closely related to transport. It is sensitive to the presence of extended states. In order to be able to directly compare results between the two observables, we choose to use the same initial state for both observables. As the imbalance requires a charge-density wave pattern as an initial state, the charge-density wave is hence also employed for measurements of the expansion. The preparation of this initial state is described in section 2.4.1.

2.4.1   Local density imbalance

The primary observable used in the described experiments is the density imbalance $\mathcal{I}$ between even and odd sites. This observable is based on the idea that microscopic patterns not present in the Hamiltonian cannot persist in ergodic time evolution. As is illustrated in Fig. 2.6, we monitor the time evolution of an initial charge-density wave (CDW) pattern, where atoms can only occupy even sites. In an extended system, time evolution will erase this initial pattern, resulting in an equilibrium state where all sites are equally occupied. In the presence of localized states, however, remnants of the initial CDW will persist. Note that while a persisting pattern always indicates the presence of localized states, a vanishing pattern does not necessarily mean that the system is ergodic.
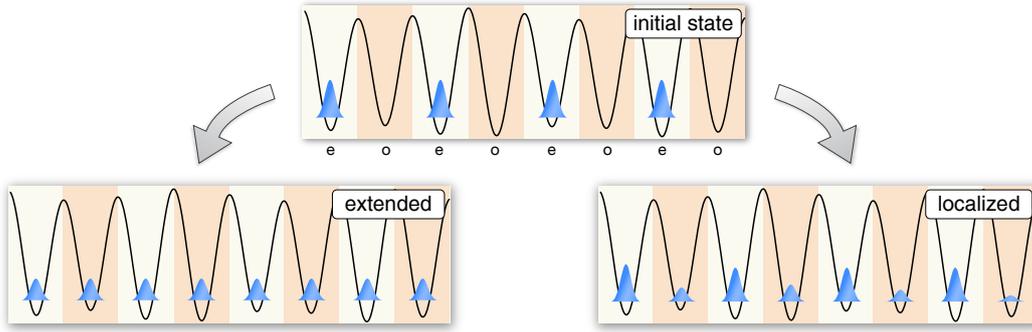
Figure 2.6: Relaxation of a charge-density wave: Illustration of the time evolution of an initially prepared charge-density wave, where only even sites are occupied. In a fully extended system, the charge-density wave will fully relax and all sites are occupied with the same probability. In the presence of localized states parts of the initial state remain.

We quantify the imbalance $\mathcal{I}$ as the normalized population difference between the atom number on even N_e and on odd N_o sites

$$\mathcal{I} = \frac{N_e - N_o}{N_e + N_o}. \tag{2.18}$$

With this definition, the imbalance of the initial state ideally is $\mathcal{I}_{\text{initial}} = 1$. In an extended system, the imbalance decays to zero, while a finite imbalance $0 \leq \mathcal{I} \leq 1$ indicates a localized system. However, initial imbalances measured are usually only about $\mathcal{I}_{\text{initial,real}} = 0.92$, indicating that the preparation of the CDW and the detection of atoms are not perfect. Whether this reduced initial imbalance is mostly caused by the preparation or the detection sequence is unknown. It is, however, not problematic, since the basic observations of whether a system is localized or not can be made independent of the exact initial imbalance.

The charge-density wave can in principle relax on the microscopic timescale of a single tunneling time $\tau = \hbar/J$, as no long-distance mass transport is necessary to reach an equilibrium state. This makes the imbalance an intrinsically fast observable, which is able to resolve even very slow dynamics. Slow dynamics is e.g. expected close to phase transitions. In contrast, global observables, like the expansion, require mass transport over long distances to relax and are expected to show slow hydrodynamic tails [13].

Initial state preparation: To create the charge-density wave, the atom cloud is loaded into the ground band of a three-dimensional optical lattice, formed by deep lattices along the orthogonal directions as well as the long 1064 nm lattice along the one-dimensional tubes in the longitudinal direction. During the loading of the lattice, the atom cloud is tightly confined by strong dipole traps. If a spin mixture is present, the interaction strength can be set anywhere in-between strongly repulsive ($110\,a_0$, where a_0 is the Bohr radius), or attractive ($-90\,a_0$) to favor or suppress the formation of doubly occupied sites.

a   CDW preparation

b   CDW readout

$$\mathcal{I} = \frac{N_e - N_o}{N_e + N_o}$$
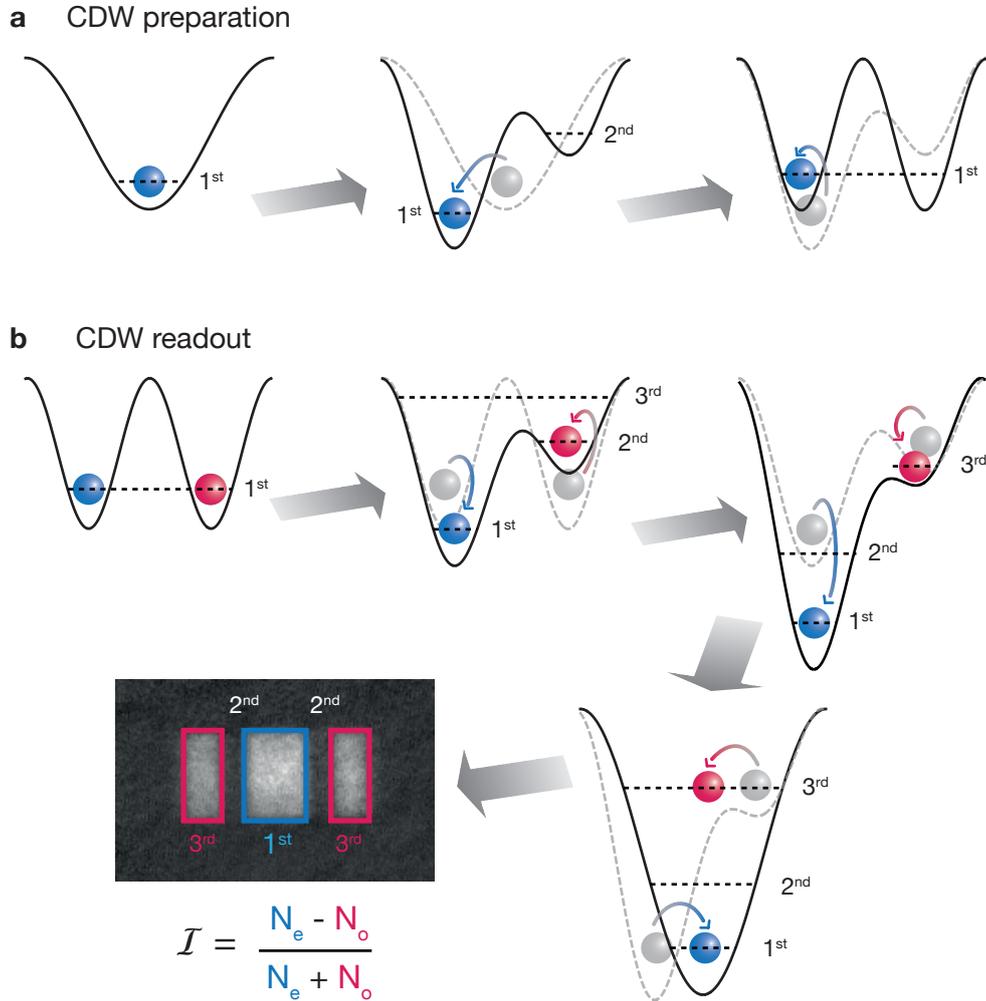
Figure 2.7: Charge-density-wave preparation and readout: a) Schematic illustration of the creation of the CDW for a single double-well. Black dashed lines indicate energy bands of the lattice, which are labeled with their band index, where the 1st band is the ground band. b) Schematics of the imbalance readout. The atom sitting on an even (blue) and odd (red) site are indicated by different colors, which do not (necessarily) imply different spin states. The color coding is further used to indicate the location of atoms on even/odd sites on the shown band-mapped picture, which was taken after $8\,\mathrm{ms}$ of time-of-flight. Since there are no atoms in the 2nd band, atoms on even and odd sites are clearly spatially separated and their respective numbers can be extracted from the pixel count. The imbalance $\mathcal{I}$ can then be calculated as their normalized difference.

In this initial state, the central tube along the **x** direction typically fills about 100 sites of the long lattice (corresponding to 200 sites in the primary lattice). The system is about 120 tubes broad in the **y** direction, as well as about 25 tubes in the **z** direction. Since the lattices are relatively deep, the coherence between the lattice sites dephases due to the dipole trap and technical heating. Hence, the system is well described by a product state of the individual particles occupying Wannier states on their respective sites.

The sequence for the creation of the charge-density-wave is illustrated in Fig. 2.7a for a single double-well. The exact sequence, involving all lattice depths and ramp durations, can be found in Appendix A. The density imbalance onto the even sites is created by splitting the long lattice asymmetrically with the primary lattice to create a tilted configuration. The asymmetry is achieved by choosing a relative phase of $\pi/3$ between the lattices. The splitting causes the lowest energy band of the long lattice to split into two. Since the process is performed adiabatically, atoms stay in the lowest energy band, which is now located on the even sites. Holding in this tilted configuration, the magnetic field is ramped to set the interaction strength to its final value (i.e. the value wanted during the evolution time). A full calculation of the band structure throughout the sequence can be found in Ref. [122].

In the last preparation step, the long lattice is suddenly switched off, thereby projecting the populations onto the primary lattice. Simultaneously, the detuning lattice is overlapped. Then, the primary lattice is quenched down to allow tunneling, thereby initiating the time-evolution in the quasi-periodic system.

Final state readout: The evolution time is ended by suddenly freezing the atoms, which is achieved by quickly increasing the depth of the primary lattice. The readout of the imbalance $\mathcal{I}$ is then performed using the superlattice in combination with a band-mapping technique [104]. This sequence is illustrated for a single double-well with an atom on an even and an atom on an odd site in Fig. 2.7b. In a first step, the atoms are diabatically transferred into the tilted superlattice configuration which was also used in the preparation by overlapping the primary with the long lattice. Simultaneously, the detuning lattice is switched off. Since this first step is diabatic, the atoms do not both tunnel onto the site with lower energy but remain at their respective sites. This excites atoms that were on odd sites to the second band. As in the loading procedure, in this configuration, the magnetic field is ramped again to set the interactions to zero, which is required for the band-mapping steps.

Afterwards, the long lattice is, again diabatically, ramped to extremely deep values of almost $90\,E_r^{1064\,\mathrm{nm}}$. This causes a crossing of the 2nd and the 3rd band which the atoms cannot follow. Hence, after switching off the primary lattice adiabatically, atoms initially located on odd sites are in the 3rd band of the long lattice, while atoms initially on even sites remain in the 1st (ground) band. Band-mapping the system, i.e. mapping the lattice momenta onto real-space momenta, results in the shown picture, which was taken after a time-of-flight of 8 ms. Since the atoms from the third and the first bands are clearly
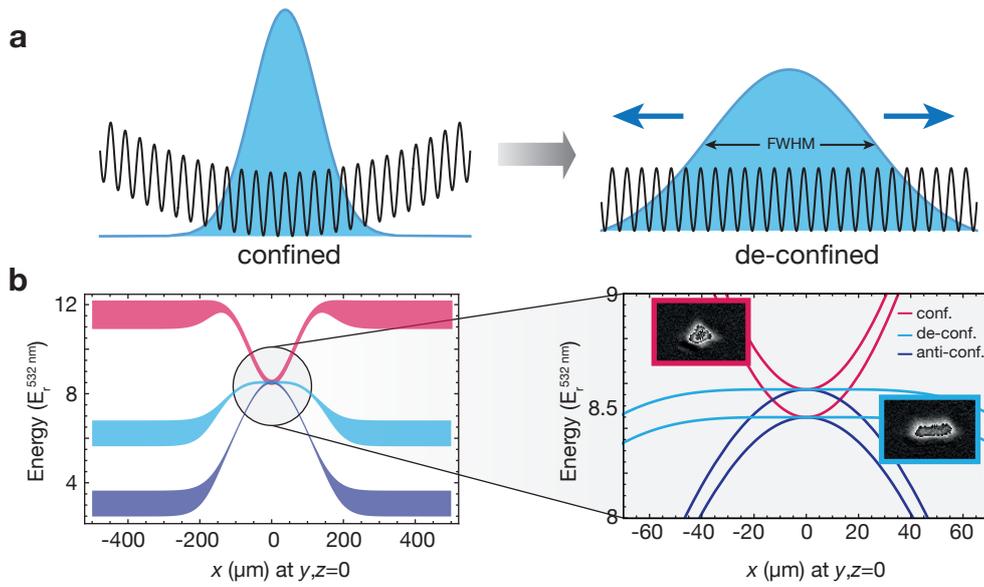
Figure 2.8: Expansion of a cloud: a) Schematics of expansion measurements. A cloud (blue), initially confined in a harmonic trap, is released into a homogeneous lattice. After expansion, the full-width-at-half-maximum cloud size is extracted from in-situ measurements. b) Calculation of the structure of the lowest band for the experimental parameters with a strong (red), zero (dark blue) and intermediate dipole trap strength (light blue). The dipole trap potential is individually defined such that it is zero in the trap center. In the absence of a dipole trap, the cloud is strongly anti-confined due to the blue-detuned lattices. At the correct depth of the dipole trap the harmonic terms of the confinement and the anti-confinement cancel. However, higher order terms cannot be canceled, and hence the band is not fully flat. The inset shows a zoom of the trap center to better visualize the comparison of the bandwidth to the harmonic trap in the three cases. Typical in-situ images, taken after $60\,\tau$ expansion time in the deconfined and the confined geometry, are shown.

spatially separated, simply counting pixels yields the relative atom numbers on even and odd sites respectively.

2.4.2 Global expansion

The expansion of an initially confined atom cloud is a natural probe for localization, as it intuitively connects to the idea of transport. Furthermore, its experimental implementation in e.g. waveguides [21, 47] is, compared to measurements of the imbalance, rather straightforward. Accordingly, it has been used to investigate localization in a variety of different systems and settings [21, 47, 57–61, 64, 125, 126]. The expansion of interacting and non-interacting systems is also interesting in its own right and has been studied experimentally in homogeneous systems [105, 133–135]. It can be quantified in a large variety of ways. While the most straightforward quantification is the actual size of the cloud, it can e.g. also be understood as the melting of domain walls [64], where the atom

cloud is initially confined to one half of the system and the expansion is quantified via the fraction of atoms that moved to the initially unoccupied side. The defining characteristic of expansion, namely global mass transport, remains the same in this case.

Limits of expansion dynamics: Studying expansion is performed by preparing an atom cloud in an initially tightly confined trap, which is then removed to start the expansion (Fig. 2.8a). This is most easily implemented in one-dimensional geometries consisting of a single dipole beam and optical lattice (potentially overlapped with a second optical lattice to create a quasi-periodic pattern), as e.g. performed in [21, 47]. In such a setup, the dipole beam and the lattices create a strong trapping potential in the transverse directions, but the longitudinal direction is essentially unconfined. This is important for the expansion of the cloud, as a trapping (or anti-trapping) potential in the longitudinal direction would restrict the expansion of the cloud. The maximally achievable cloud size in the presence of a trap can be estimated as

$$4J \approx \frac{1}{2}m\omega^2\sigma_{\max}^2 \tag{2.19}$$

where $\sigma_{\max}$ denotes the maximally achievable cloud size and ω the trapping frequency. This equation states that a cloud can only expand to the point where the energy of the trap becomes similar to the bandwidth. This is intuitive as the bandwidth is equivalent to the maximum kinetic energy a particle can have.

Unfortunately, the above-described lattice geometry of a single beam along the longitudinal direction does not confine the motion of the atoms in the perpendicular direction. Instead, the motion along the orthogonal directions is that of particles in a two-dimensional homogeneous system. While this is unproblematic in a non-interacting system, where the motion along the respective directions is separable, interactions will couple the spatial directions and the two-dimensional planes start acting as a bath [136].

In our setup, this is avoided by employing deep lattices along the transverse directions, which freeze out those motional degrees of freedom. The evolution in the resulting one-dimensional tubes then implements a one-dimensional system also in the presence of interactions. However, studying expansion in such a geometry is far more challenging, as the (anti-)confinement of the transverse lattices creates strong trapping potentials in the longitudinal direction, thereby inhibiting the expansion of the cloud.

Creating flat potentials to enable expansion: In the presented setup, expansion measurements are realized by first loading the atom cloud into the charge-density wave configuration as described in section 2.4.1. In this configuration, the atoms are held in a three-dimensional optical lattice and are strongly confined by three dipole beams. To initiate the evolution time, the primary lattice along the **x** direction is ramped low to enable tunneling. Simultaneously, the trapping along the longitudinal direction is removed by compensating the anti-confinement of the lattice beams with the confinement of the dipole beams. Specifically, the vertical dipole beam is set to a strength where it cancels

the anti-confinement created by the blue-detuned transverse lattice beams. Since the horizontal dipole traps have a different geometry than the lattice beams (see section 2.2.2), they cannot be used to compensate the anti-confinement and are hence switched off during the evolution time. The longitudinal beams do not contribute a confinement along the longitudinal direction. This results in a geometry where the cloud see a flat potential in the longitudinal direction, but is anti-confined along the orthogonal directions. This anti-confinement is unproblematic, as the dynamics in this direction are frozen out by the deep orthogonal lattices.

The structure of the lowest band along the longitudinal **x** direction is shown in Fig. 2.8b for three different strengths of the vertical dipole trap. In the absence of any dipole trap (dark blue), the cloud is strongly anti-confined. In the typical configuration used for loading the charge-density wave (red), the cloud is strongly confined. At an intermediate strength of the dipole trap, however, the harmonic terms of the trapping and anti-trapping potentials cancel, allowing the cloud to expand along the **x** direction. Note that a perfectly flat potential can never be achieved, as only the quadratic terms of the trapping and anti-trapping potential cancel, but higher order terms remain. Additionally, misalignments of the beams and slightly different shapes limit the achievable flatness in the experiment.

After the time evolution, the expanded cloud is imaged in-situ. Typical pictures after times of $60\,\tau$ for a confined and a deconfined system are shown in the inset of Fig. 2.8. It is clearly visible, that the deconfined cloud shows a pronounced elongation resulting from the expansion, while the almost round shape of the confined cloud suggests that it barely expanded.

Quantification of the cloud size: We quantify the expansion of the cloud via the full-width-at-half-maximum (FWHM) cloud size σ. To extract this parameter from the in-situ images, we first integrate the pictures along the **y** direction, thereby suppressing imaging noise. The half-maximum points in the integrated density profile are then determined as the location of the first pixel whose value is above half-maximum when moving inwards from both directions. The cloud size σ can then be calculated from the pixel index difference, multiplied by the pixel size, which was calibrated to be $\sim 2\,\mu$m.

Details of the experimental procedures, as well as the FWHM observable, are described in more detail in Ref. [112]. There, also the experimental advantages and problems of different quantities characterizing the expansion are discussed. In our work, we have found the FWHM to be most reliable for the experimental data. In numerical studies, however, other quantities yield better results (see section 3.1.4).

Single-particle localization in a quasi-periodic lattice

In this chapter, we will show experimental measurements and numerical simulations analyzing the localization of non-interacting particles in the quasi-periodic lattice. Specifically, we employ both observables (the imbalance and the expansion) to map out the full phase diagram of the quasi-periodic optical lattice. Our measurements demonstrate the existence of an intermediate phase, in which extended and localized states coexist at different energies. This intermediate phase vanishes when the tight-binding limit is approached. In the tight-binding limit, we compare experimental measurements of the imbalance to numerical simulations of the AA model, thereby verifying that the model indeed accurately describes the experimental system.

Fig. 3.6 illustrates the various phases present in the quasi-periodic lattice model. At low depths of the detuning lattice, we expect the system to be fully in the extended phase. In this regime, the initial CDW-pattern should rapidly vanish and the atomic cloud should show a continuous expansion. In the opposite limit of a deep detuning lattice, we expect a fully localized phase where no expansion is visible and remnants of the CDW pattern remain. In-between those two phases, a third, more intriguing 'intermediate' phase can exist. In this phase, the system is neither fully localized nor extended. Instead, both extended and localized states can exist simultaneously, but at different energies. Note that a coexistence at the same energy is generally not possible [137]. As is shown in the illustration of the density of states $n(\epsilon)$, the localized and extended states are separated by a critical energy ϵ_c, known as the 'single-particle mobility edge' (SPME).

Distinguishing the intermediate phase from the localized or extended phase is not possible based on measurements of a single observable, as e.g. the presence of an extended state in an otherwise localized system will only give a quantitative change in the imbalance. However, the combination of imbalance and expansion are suited to distinguish the intermediate phase as the regime where both quantities have finite values. While we can accurately detect the intermediate phase, in our setup a direct measurement of the critical energy ϵ_c is not possible. This is because of the charge-density wave initial state required for measurements of the imbalance. In the charge-density wave state,
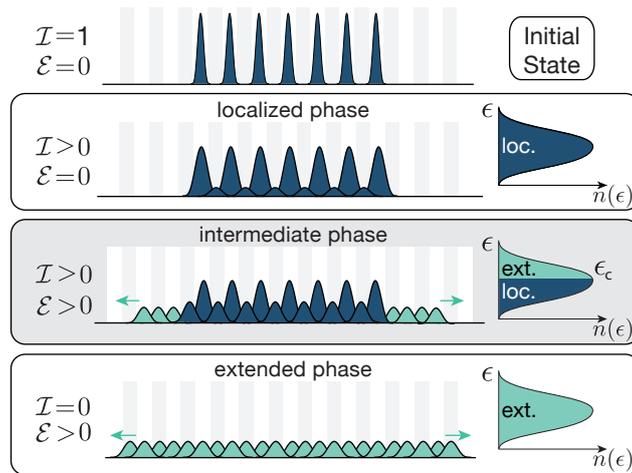
Figure 3.1: Schematic illustration of the phases in the quasi-periodic lattice: Schematic illustration of the phases and the dynamical behavior of an initial CDW state in the quasi-periodic lattice. A finite imbalance ($\mathcal{I} > 0$) indicates the presence of localized states, a finite expansion $\mathcal{E} > 0$ the presence of extended states. In the intermediate phase, where extended and localized states coexist, both quantities are simultaneously finite.

single-particle eigenstates throughout the entire spectrum are occupied and hence it is not possible to address specific energy intervals.

Intermediate phases are expected in almost all systems with some form of quasi-periodicity [49, 138–143], as well as in randomly disordered systems in three dimensions [20, 144], where they have been observed experimentally [58, 125, 126] (although the interpretation of the experimental results is still under discussion [145]). Especially, the intermediate phase has also been theoretically predicted for our lattice model [50, 114, 146]. Note, however, that neither the one-dimensional Anderson nor the AA model possesses an intermediate phase.

3.1   Time evolution in the quasi-periodic system

In this section, we will show typical time traces of the imbalance and the expansion. We will discuss their dynamical behavior and describe how we can investigate the phases of the quasi-periodic lattice with measurements after certain, finite evolution times. We will give the time in units of the tunneling time $\tau = \hbar/J$ in the primary lattice, which is the characteristic timescale of the Hamiltonian. Here, J denotes the coupling between nearest neighboring sites as in section 2.3.2. Note that while J is independent of the strength of the detuning lattice V_d, it heavily depends on the depth of the primary lattice V_p and is therefore not constant throughout the phase diagram. Typical values of the tunneling time lie in-between $\tau(V_p = 4\,E_r^p) \approx 0.1\,\mathrm{ms}$ and $\tau(V_p = 8\,E_r^p) \approx 0.3\,\mathrm{ms}$. Note that we will give all lattice depths in recoil energies of the *primary* lattice E_r^p.
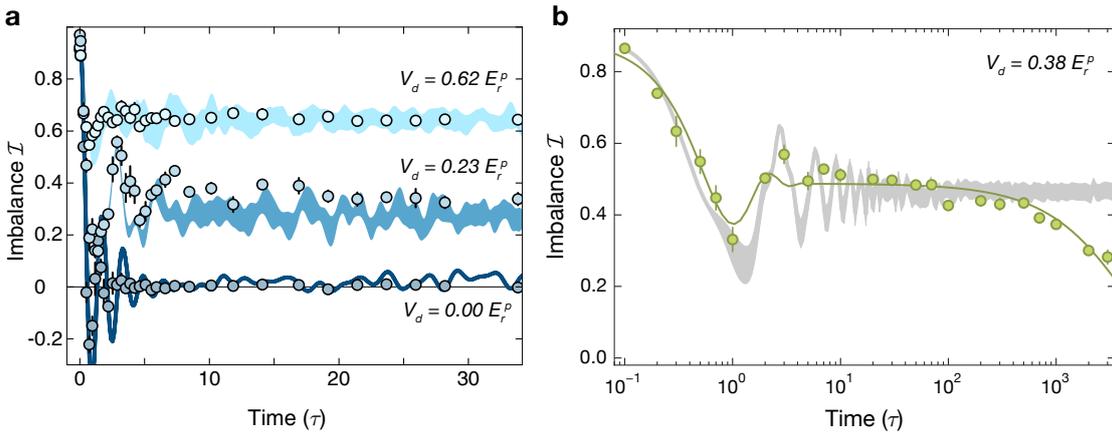
Figure 3.2: Time evolution of the imbalance: a) Time traces of the imbalance $\mathcal{I}$ for various depths of the detuning lattice V_d at a primary lattice depth of $V_p = 8\,E_r^p$. Points are experimental measurements, averaged over 6 different detuning realizations ϕ. Errorbars denote the standard deviation of the mean. Lines are theoretical simulations, which correctly take into account the trapping potential and the averaging over neighboring tubes, which are present in the experiment. However, they are performed on the AA Hamiltonian. b) Long-term time trace on a logarithmic time axis. The gray shaded region is the result of a numerical simulation on the AA model, the solid line is a stretched exponential guide-to-the-eye. Numerical data calculated by Pranjal Bordia [43, 69].

3.1.1 Time traces of the imbalance $\mathcal{I}$

As described in section 2.4.1, measurements of the imbalance are performed by first preparing the initial CDW-state, quenching to the quasi-periodic system and letting the system time evolve under its intrinsic dynamics until finally extracting the imbalance with a band-mapping technique. Any measurement of the imbalance is averaged over six realizations of the detuning pattern ϕ to ensure that different detuning realizations are sampled by the finite size system, and to suppress noise. Fig. 3.2 shows exemplary time traces at a primary lattice depth of $V_p = 8E_r^p$ for various strengths of the detuning lattice V_d. Time traces at other primary lattice depths look qualitatively similar.

We find that the imbalance quickly decays from its starting value $\mathcal{I}(t = 0) \approx 0.95$ to a steady state value, reached after only few tunneling times. The starting imbalance is not exactly one, due to the limited fidelity of the initial state preparation and readout procedure. In the absence of detuning ($V_d = 0$) the imbalance quickly decays to zero, in agreement with the expectations for an extended system. At $V_d = 0$, this decay should follow a Bessel function, whose average value quickly decays to zero, but which shows long-lived oscillations with an envelope that decays as $1/\sqrt{t}$. These oscillations are, however, not present in the experimental data. This is predominantly due to two effects: (1) An inherent averaging over many neighboring one-dimensional systems (tubes). Due to the Gaussian shape of the beams creating the optical lattice, the lattice depth in a tube sightly decreases towards the edges of the system, resulting in stronger tunneling strengths J and a slightly weaker detuning lattice depth V_d and (2) the overall harmonic confinement. In

the presence of the detuning lattice, the same sharp decay of the imbalance from its initial value is observed. However, the steady-state value reached afterward is finite and depends on the strength of the detuning lattice, indicating that the system is indeed localized.

The experimental measurements are compared to theoretical simulations, which include the dipole trap and the averaging over many tubes. In the presence of the detuning lattice, these simulations additionally need to be averaged over the realizations of the detuning lattice. The statistical uncertainty, resulting from this averaging, is indicated in Fig. 3.2a via the width of the lines. We find a very good agreement between the theoretical and experimental results, indicating a good understanding of the effects of the tube averaging and the dipole trap. Furthermore, the presented calculations have been performed not for the full lattice model, but instead on the AA-Hamiltonian. The good agreement suggests that a primary lattice depth of $V_p = 8\,E_r^p$ is sufficiently close to the tight-binding regime for the experimental system to accurately map to the AA-model. This is further investigated in section 3.3.

Problems with the imbalance arise at longer times, as is shown in Fig. 3.2b. At such long times, the imbalance does not remain at its stationary value, as is expected from theoretical simulations, but instead shows a slow decay to zero. This is due to couplings of the system to its environment slowly resulting in the thermalization of the system. From the shown time trace we find that these external couplings become relevant after about $200\,\tau$. However, this timescale depends heavily on the depth of the detuning lattice, as well as on the value of τ [69]. A detailed study of the effects of external baths is presented in chapter 7.

Our observations suggest that the behavior of the system does not require a full dynamical analysis, but can instead be captured accurately enough via a single measurement of the equilibrium value of the imbalance. We choose to access the equilibrium imbalance after an evolution time of $200\,\tau$. This time was chosen as the longest possible time where effects from external decays are not significant yet. It is important to choose the evolution time as long as possible to avoid finite-time effects close to the phase transition, where we expect slow dynamics (see section 6.3). In order to suppress noise and access various realizations of the detuning pattern, finite-time measurements will be averaged over six phases of the detuning lattice ϕ.

3.1.2   Estimation of finite time errors in the imbalance

In order to estimate the magnitude of the finite-time error resulting from slow dynamics and the measurement of the imbalance after only $200\,\tau$, we compare the experimental non-interacting imbalance to the numerically simulated imbalance after $3000\,\tau$ in Fig 3.3. The comparison is shown for various depths of the detuning lattice V_d at a primary lattice depth of $V_p = 4\,E_r^p$, where the finite-time error is most significant. We find that the experiment agrees well with the numerics for most V_d. However, there is a small regime where significant deviations are observable. We will later identify this regime to be largely consistent with the intermediate phase. Importantly, the deviations between $200\,\tau$ and
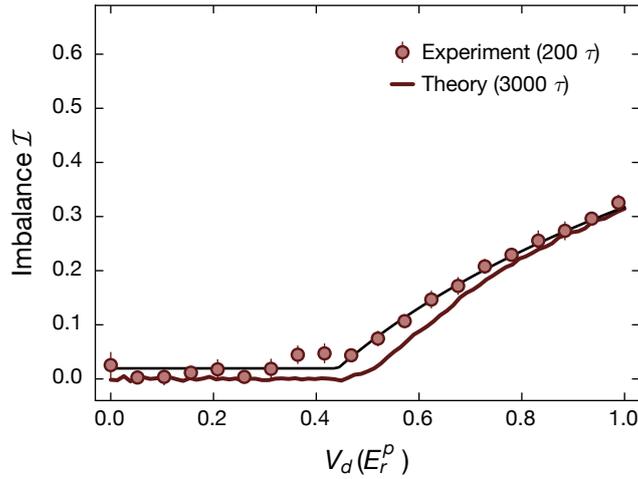
Figure 3.3: Finite time errors in the imbalance: Experimentally measured imbalance after $200\,\tau$ and numerically calculated imbalance after $3000\,\tau$ at a primary lattice depth of $V_p = 4\,E_r^p$. Errorbars denote the standard deviation of the mean. The solid black line is a guide-to-the-eye. Numerical data was calculated by Xiao Li.

$3000\,\tau$ are only of quantitative nature. The detuning lattice depth, where the imbalance first becomes finite, is essentially unaffected.

3.1.3 Time traces of the expansion $\mathcal{E}$

We extract the expansion of the cloud by comparing the in-situ cloud size σ before and after time evolution. For this, we employ the same state preparation sequence as for the imbalance, but instead of the detection sequence, an in-situ picture is taken. The size is extracted as the full-width at half maximum (FWHM) width of the cloud, which was found to be the most stable quantity as in Refs. [105, 112, 120, 133]. The expansion can then be defined as $\mathcal{E} = A * (\sigma - \sigma_0)$, where σ_0 is the initial cloud size at $t = 0$ and $A = 0.01\,\text{site}$ is a constant scaling factor which enables an easy comparison of the imbalance and the expansion on the same scale. Exemplary time traces of the cloud size σ at a primary lattice depth of $V_p = 4E_r^p$ for various depths of the detuning lattice are shown in Fig. 3.4a. Later, we will find that the three detuning lattice depths correspond to the extended, intermediate and localized phase, respectively. We find a very fast expansion in the extended phase and a constant cloud size in the localized phase. The intermediate phase exhibits a very slow expansion, which demands long observation times in order to be properly resolved.

We compare our experimental measurements to numerical simulations of the edge density, which gives a more direct description of extended states and is numerically more stable than the FWHM (see section 3.1.4). The edge density $\mathcal{D}$ is defined as the fraction of atoms that leave an initially populated center third of a simulated system of size $L = 369\,\text{sites}$, i.e. $\mathcal{D} = 1 - N_c/N$, where N is the total particle number and N_c the number of
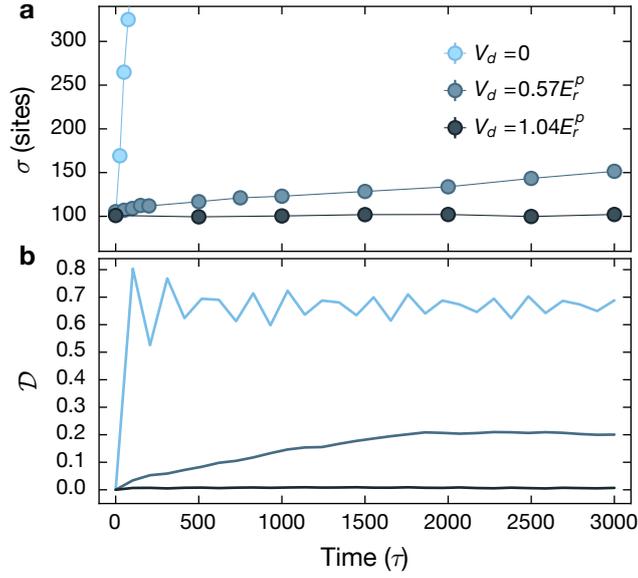
Figure 3.4: Time evolution of the cloud size: Time traces of the a) experimentally measured FWHM cloud size σ and b) the theoretically calculated edge density $\mathcal{D}$. Traces are shown for the extended ($V_d = 0$), the intermediate ($V_d = 0.57\,E_r^p$) and the localized ($V_d = 1.04\,E_r^p$) phase. In the numerical analysis the cloud sizes eventually saturate due to the finite size of the simulated system. Numerical data was calculated by Xiao Li.

particles remaining in the center third. The edge density is also simulated from a slightly different initial state. While the experimental initial state is a product of Wannier states with an overall Gaussian envelope and a charge-density wave configuration, the numerical initial state is chosen to be the eigenstates of the center third of the system. However, we do not expect the initial state to have a qualitative impact, as it is also a high energy state after the quench to the full system. A detailed comparison of different expansion observables for the experimental state can be found in section 3.1.4.

As Fig. 3.4 shows, we indeed find that the edge density shows a qualitatively similar behavior compared to the cloud size σ. In the extended phase, it rapidly increases until it saturates due to the limited system size. In the localized phase, the edge density does not register any dynamics. In the intermediate phase, the edge density is significantly slower than in the extended phase, but also eventually saturates to a maximum value. This maximum value is smaller than the corresponding one in the extended phase, as not all particles participate in the expansion dynamics.

To enable the cloud to expand in the experiment, the confining potential of the dipole traps needs to be removed. This is achieved by reducing the strength of the dipole traps such that they just compensate the anti-confinement of the blue-detuned optical lattices (see section 2.4.2). However, slight unevennesses might remain, as only the harmonic term can be compensated. Additionally, any misalignment or fringes will result in inhomogeneities. As will be discussed in detail in section 3.1.4, this unevennesses potentially heavily affects the expansion dynamics, especially in the presence of a strong detuning
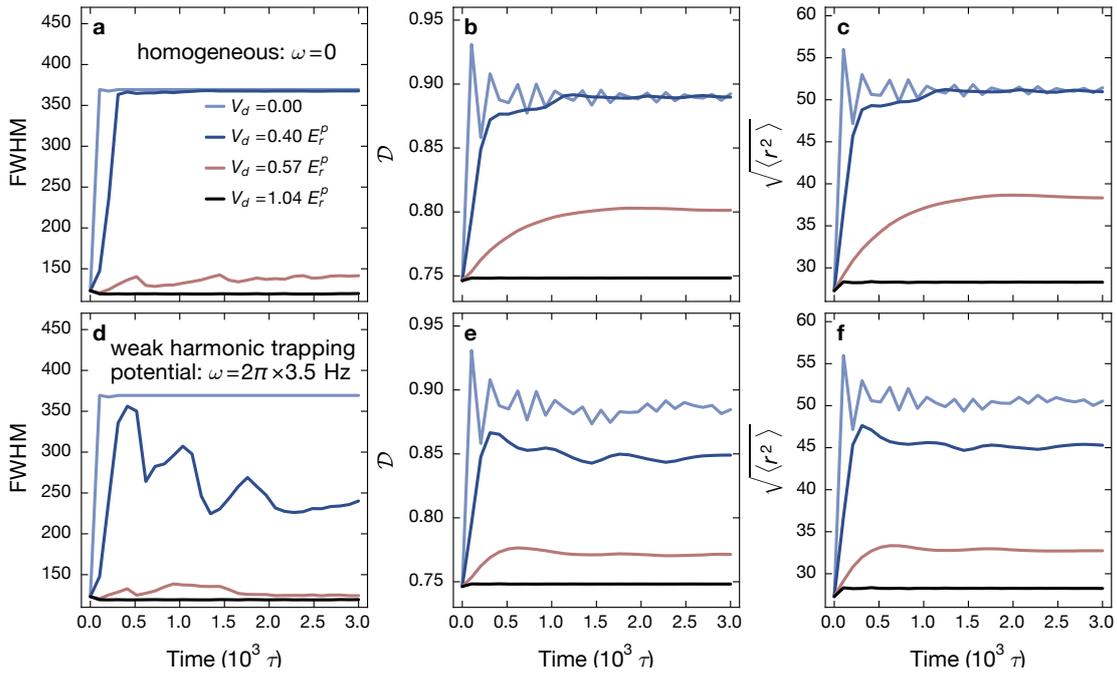
Figure 3.5: Comparison of various expansion obervables: Comparison of the FWHM cloud size, the edge density $\mathcal{D}$ and the root mean expectation value of the squared radius $\sqrt{\langle r^2 \rangle}$ in a homogeneous system (a-c) and in the presence of a slight dipole trap (d-f). The initial state is, in all cases, a product of Wannier states with a Gaussian envelope of size $\sigma = 123$ sites. The dipole trap employed in d)-f) was chosen to have a trapping frequency of $\omega = 2\pi \times 3.5$ Hz. Data was calculated by Xiao Li [109].

lattice. In the extreme case, the unevenness could cause the absence of expansion dynamics even if extended states are present. However, a finite expansion still always marks the presence of extended states and the very good agreement between the experimental and theoretical phase diagram in section 3.2.1 suggests that the influence of remaining unevennesses cannot halt the expansion dynamics completely if extended states are present.

In order to capture the presence or absence of expansion dynamics from a single finite-time measurement of the cloud size, the very slow expansion speed in the intermediate phase requires a long evolution time. Indeed, we choose an evolution time as long as $3000\,\tau$. This is potentially problematic, as the imbalance shows that at such long times the system is already heavily influenced by external couplings. However, such effects should influence a global quantity, like the expansion, only on much longer timescales than a local quantity like the imbalance.

3.1.4 Numerical comparison of different expansion observables

In this section, we will motivate the use of a different observable for the expansion in theory than in the experiment, and show numerical simulations illustrating the effects of

a (very) weak trapping potential on the expansion. Fig. 3.5 shows simulated time traces of three different expansion observables. The simulations have been performed on a model of the experimental initial state, i.e. a product of Wannier states with a Gaussian envelope. For a simple box-shaped initial state, the FWHM would not capture the expansion if less than half the particles were extended.

The FWHM and the edge density are calculated as described earlier. Further, the expectation value of the square of the radius is calculated as $\langle r^2 \rangle = \sum_i (i - i_c)^2 \langle \hat{n}_i \rangle$, where i_c is the index of the central site and $\hat{n}_i$ is the density operator on site i. We find that all three observables show a similar behavior of fast expansion in the extended phase, slow expansion in the intermediate phase and no expansion in the localized phase. Further, a comparison with Fig. 3.4b shows that the edge density is not qualitatively influenced by the different initial state. We find, however, that the simulated FWHM is much noisier than the other quantities. This is likely due to the FWHM depending mostly on the local densities of only a few sites, whereas the other quantities inherently average densities over all sites of the system. Hence, much more averaging would be needed to get a noise-free signal from the FWHM, making its simulation much harder in numerics.

Fig. 3.5d)-f) studies the effects of inhomogeneities in the global potential on the example of a weak dipole trap. For these simulations, we choose a trapping frequency of $\omega = 2\pi \times 3.5\,\mathrm{Hz}$, which is chosen from a rough estimate of the expected inhomogeneity in the experimental system. For this frequency and the simulated system size, the effects of the dipole trap remain very weak compared to the bandwidth of the homogeneous system. Accordingly, we find that the expansion in the absence of the detuning lattice is barely influenced. However, in the presence of the detuning lattice, we do find lower saturation values, even within the fully extended phase. This is even more pronounced in the intermediate phase, suggesting that any inhomogeneities indeed become increasingly relevant with increasing strengths of the detuning lattice. Hence, the experimental expansion dynamics are certainly influenced by the remaining inhomogeneities eventually.

3.2   Observation of the intermediate phase

Based on the finite time measurements of the imbalance $\mathcal{I}$ and the expansion $\mathcal{E}$, we probe the phases of the quasi-periodic lattice at infinite temperature as a function of the primary and the detuning lattice depth V_p and V_d. As was discussed in the previous section, the two observables show dynamics on vastly differing timescales, necessitating measurements at different timescales of $200\,\tau$ for the imbalance and $3000\,\tau$ for the expansion. Exemplary measurements for three different primary lattice depths are shown in Fig. 3.6a)-c). We find, that for all primary lattice depths there exist three different phases. At low depths of the detuning lattice, we always find a phase where the imbalance is zero. This directly shows the absence of any localized states and hence this phase is fully extended. At deep detuning lattices, we find a phase where the expansion is zero. As this excludes any extended states, this phase is fully localized. In between, we find a phase where both the
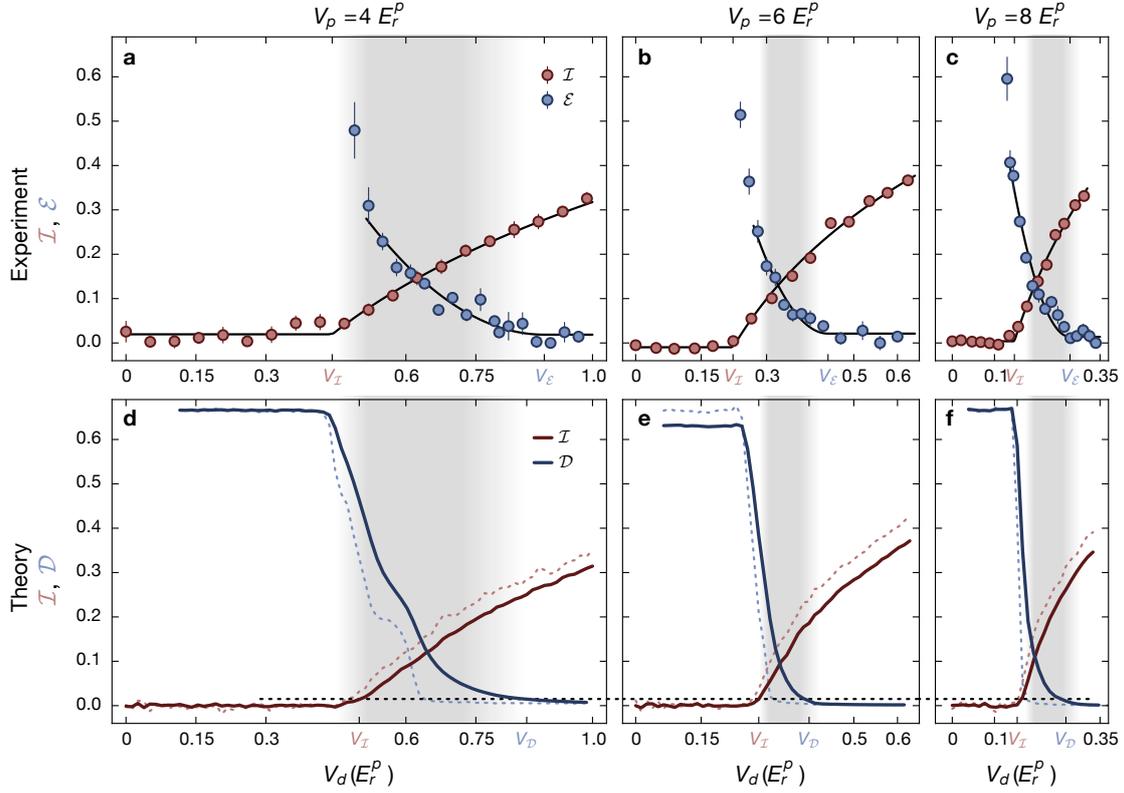
Figure 3.6: Direct measurement of the intermediate phase: a)-c) Measurement of the stationary imbalance $\mathcal{I}$ after $200\,\tau$ and the expansion $\mathcal{E}$ after $3000\,\tau$. Experimental data is averaged over six realizations of the detuning phase ϕ, error-bars denote the standard error of the mean. The gray shading illustrates the approximate extent of the intermediate phase and black solid lines are fitting functions to extract the critical detuning strengths $V_{\mathcal{I}}$ and $V_{\mathcal{E}}$. d)-f) Numerical simulations for the imbalance and the edge density $\mathcal{D}$, both evaluated after approximately $3000\,\tau$. Solid lines denote the results including an averaging over many tubes with slightly different lattice depths. Dashed lines show the result for the central tube. The horizontal black dashed line marks the threshold of 0.015 that is used to determine $V_{\mathcal{I}}$ and $V_{\mathcal{D}}$ from the theoretical simulations. Theoretical simulations were performed by Xiao Li [109].

imbalance and the expansion is simultaneously finite. This directly shows the coexistence of extended and localized states and hence marks the intermediate phase.

The experimental results are compared to numerical simulations for the imbalance and the edge density $\mathcal{D}$ (see section 3.1.3), which are performed as in Ref. [146] and shown as dashed lines in Fig. 3.6d)-f). In these simulations, both the imbalance and the edge density are evaluated after $3000\,\tau$. As in the experiment, we always find the described three phases. However, while the imbalance agrees very well between theory and experiment, the edge density predicts a significantly narrower intermediate phase in theory. This is again due to the averaging over many parallel one-dimensional tubes, which is inherently present in the experiment. Due to the finite extent of the beams forming the optical lattices, tubes on the outside of the system have slightly lower lattice depths than those in the center. Including this effect in the numerical simulations (as described in appendix B) gives the results presented as solid lines. These predict an intermediate phase in very good agreement with the experimental measurements.

Note that considering the averaging over tubes, as compared to only considering the central tube, has only a quantitative effect on the imbalance, but actually shifts the detuning lattice depth where the expansion vanishes. This highlights again that the imbalance is most sensitive to the presence of localized states, which initially appear in the center of the system, whereas the expansion is more sensitive to extended states, the last ones of which disappear at the far edges of the system.

To characterize the phase diagram, we extract the phase boundaries between the extended and the intermediate phase as the detuning lattice depth where the imbalance becomes finite $V_{\mathcal{I}}$, as well as the boundary between the intermediate and the localized phase as the detuning lattice depth where the expansion vanishes $V_{\mathcal{E}}$. For the experimental data, this is done via heuristic fit functions. For the imbalance, we choose the fitting function

$$\mathcal{I} = \begin{cases} a \times \ln(V_d/V_{\mathcal{I}}) + o & V_d > V_{\mathcal{I}} \\ 0 & \text{else} \end{cases} \tag{3.1}$$

The logarithmic fit is motivated by the known behavior of the localization length in the non-interacting Aubry-André model [46]. The expansion is fitted as

$$\mathcal{E} = \begin{cases} b \times (V_{\mathcal{E}} - V_d)^2 + o & V_d < V_{\mathcal{E}} \\ 0 & \text{else} \end{cases} \tag{3.2}$$

The quadratic form was chosen as it fitted the expansion best for most values of V_p. Fitting with a variable exponent gave bad results as small exponents can often be readily compensated by large amplitudes b and a significant shift in $V_{\mathcal{E}}$. For the fits to the expansion also the fitting range had to be manually restricted to exclude datapoints in the fully extended phase, as there the expansion is much faster and the quadratic function no longer describes the data well.

The theoretical phase boundaries are extracted via a simple threshold value, which is possible due to the low noise. As in Ref. [146], we chose this value to be 0.015, which is just above the noise floor.
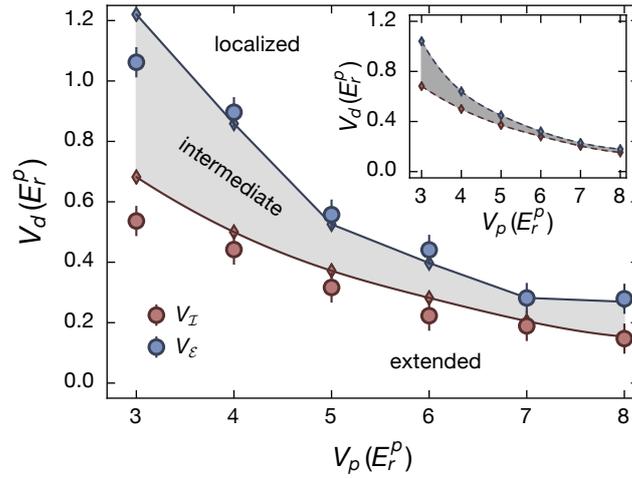
Figure 3.7: Phase diagram of the quasi-periodic lattice: Extracted phase boundaries from Fig. 3.6 based on experimental data (points) and numerical calculations (lines). Errorbars denote the uncertainty of the fits used to extract the experimental phase boundaries and the gray shading marks the intermediate phase. The inset shows the numerical result for the central tube. Numerical simulations were performed by Xiao Li.

3.2.1   Phase diagram of the bichromatic lattice

Fig. 3.7 shows the phase diagram resulting from the extracted phase boundaries. We find that at all strengths of the detuning lattice an intermediate phase exists in between the fully localized and the fully extended phases. This intermediate phase is broadest at low depths of the primary lattice and shrinks, as well as moves towards lower depths of the detuning lattice when the primary lattice depth is increased. These observations are true for both the central tube and the full, averaged system. We find very good agreement between the theoretical and experimental phase boundaries for the expansion, but a systematic trend of the experiment to slightly underestimate the lower phase boundary, extracted from the imbalance measurements. We attribute this to finite time errors due to the comparatively short time evolution used for the imbalance of only $200\,\tau$, which might not fully capture the effects of slow dynamic close to a phase transition.

The comparison of the numerical results for the averaged system and the central tube shows that the width of the intermediate phase in the experiment is almost fully due to the averaging over tubes when the tight-binding limit is approached. This observation is consistent with the idea that in the tight-binding limit the system should map onto the AA-model, which does not have an intermediate phase. We will further investigate a potential description of the experimental system via the AA-Hamiltonian in the following section.

3.3   Tight-binding description via the Aubry-André model

As was argued in section 2.3.2, in the tight-binding limit of nearest-neighbor tunneling, which is approached with increasing depths of the primary lattice V_p, our quasi-periodic lattice should map onto the AA-Hamiltonian. Evidence of this mapping being accurate enough already at a primary lattice depth of $V_p = 8E_r^p$ was given in section 3.2, where we found that the intermediate phase is essentially absent. This is a necessary condition as the AA-model does not have an intermediate phase. Also, in section 3.1.1 we found that time traces of the imbalance were well reproduced by simulations based on the AA-Hamiltonian. In this section, we will briefly discuss the absence of the intermediate phase in the AA-model and show further data showing a good description of the experimental setup by the AA-model in the tight-binding limit.

3.3.1   Absence of a single-particle mobility edge in the Aubry-André model

The existence of an SPME in an intermediate phase is the generically expected behavior in any system that exhibits a localization transition. This is true for both generic quasi-periodic geometries [49, 138–143], as well as for randomly disordered systems [20, 58, 125, 126, 144]. However, both typically studied model systems (the Anderson and the Aubry-André Hamiltonians) in one dimension explicitly do not show an SPME. Instead, eigenstates of all energies localize at the same critical disorder/detuning strength. Both model systems are fine-tuned in this regard, as any deviations would result in an SPME. For example, an experimental realization of the one-dimensional Anderson model has found an effective mobility edge due to a finite correlation length in their disorder pattern [21].

In the Anderson model, the absence of a SPME is easily explained as all eigenstates already localize at infinitesimal disorder strengths. In the Aubry-André model, however, the transition does occur at a finite detuning strength, making the absence of an intermediate phase very remarkable. The absence of a SPME in this model arises from a self-duality in the Hamiltonian [46]. This self-duality can be easily seen by considering the AA Hamiltonian

$$\hat{H}_{AA} = -J\sum_n\left(\hat{c}_n^\dagger\hat{c}_{n+1} + \text{h.c.}\right) + \Delta\sum_n\cos(2\pi\beta n)\hat{c}_n^\dagger\hat{c}_n \tag{3.3}$$

and then Fourier transforming the hopping term using

$$\hat{c}_n = \frac{1}{L}\sum_k e^{i2\pi\beta kn}\hat{c}_k, \tag{3.4}$$

giving

$$\hat{H}_{AA} = 2J\sum_k\cos(2\pi\beta k)\hat{c}_k^\dagger\hat{c}_k + \Delta\sum_n\cos(2\pi\beta n)\hat{c}_n^\dagger\hat{c}_n. \tag{3.5}$$

From this form it is obvious that the extended k-modes and the localized n-modes swap their roles at the transition point $\Delta = 2J$. Note, however, that a self-duality is not sufficient to rule out the existence of a SPME, as it is possible to construct self-dual models that do exhibit an intermediate phase [147]. The crucial aspect is the energy-independence of
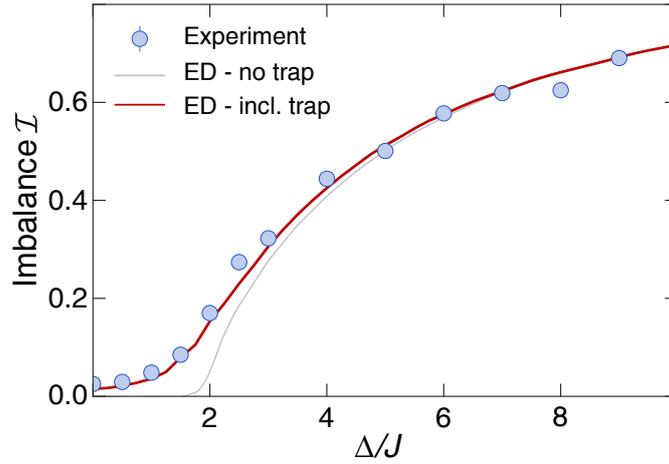
Figure 3.8: Finite-time imbalance in the experiment versus the AA-model: Steady state imbalance after $\sim 20\,\tau$ as a function of Δ. Points are experimental data, averaged over three times (close to $20\,\tau$) and 4 phases ϕ. Errorbars denoting the standard error of the mean are smaller than the point size. The gray line is a numerical simulation of the AA-model. The red line shows the same calculation, but considers the difference in tunneling between neighboring tubes and the harmonic trap. Numerical data was calculated by Pranjal Bordia [43].

the self-duality, which guarantees that states at all energies localize at the same detuning strength.

3.3.2   Direct comparison to the Aubry-André model

To establish full confidence in a description of our lattice model at $V_p = 8\,E_r^p$ by the AA-model, we compare finite-time measurements of the imbalance to AA simulations. In order to avoid any influence of external couplings, for this comparison, we choose short observation times of only about $20\,\tau$. Oscillations of the imbalance and experimental noise are reduced by averaging over 3 randomly chosen times in an interval approximately $5\,\tau$ broad. Additionally, we average over 4 detuning phases ϕ. Fig. 3.8 shows the measured data, as well as the simulations as a function of the detuning strength Δ/J, which are the parameters in the AA-model. The experimental data has been scaled to this axis by converting the detuning lattice depth V_d using the calculations presented in section 2.3.2.

As expected, we find that the simulations of the clean AA-model, presented as the gray line, shows a sharp localization transition at around $\Delta = 2J$. The experimental measurements, however, show a much more smeared out transition and values of the imbalance agree with the simulation only deep in the localized phase. We find that this smearing of the transition can be fully attributed to the presence of a dipole trap in the experiment, which effectively gives a finite localization length also in the extended phase. Including the harmonic confinement in the simulations (red line) gives a very good agreement with the experimental values.

Note that also the theoretical simulation without the dipole trap does not show a transition at exactly $\Delta = 2J$, but at slightly lower detuning strengths. This is dominantly due to a finite time effect, as the dynamics close to the phase transition are critically slow, and hence the finite observation time of $20\,\tau$ chosen in the experiment does not fully capture the imbalance after an infinite evolution time in this regime.

From the good agreement of the non-interacting experimental data with the numerical simulations, we find that our system is indeed well described by the Aubry-André model. A similar comparison with the expansion dynamics might give additional confidence but is much harder to perform as the calculations would need to implement the detailed, global experimental state (i.e. simulations would need to be performed on the actual scale of the experimental cloud size).

Part II

Many-body localization

Thermalization versus many-body localization

In this chapter, we will discuss the behavior of closed many-body systems, that are prepared in a highly excited initial state. From classical statistical mechanics [148] we know that generic systems will tend towards a thermal equilibrium state whose properties can be described by the microcanonical ensemble. As all systems are quantum, we expect the same behavior to emerge from a quantum description. Exceptions to this generic behavior do exist in so-called integrable systems, where an extensive amount of conserved quantities restricts the relaxation of the system. Typical examples of integrable systems are non-interacting systems, but integrability can also occur in interacting systems. Integrable systems are, however, very fine-tuned in the sense that slight changes of the Hamiltonian will result in a thermal behavior. Another exception occurs in disordered/detuned systems. Here, the localization of interacting particles, known as many-body localization (MBL), presents a more robust alternative to thermalization.

In this chapter, we will introduce the concepts of thermalization and many-body localization, focusing on closed quantum systems at high energy densities. We will first discuss the basic concepts and ingredients necessary for thermalization in classical systems and then expand these concepts to quantum systems, where the notion of thermalization will be discussed in the context of the eigenstate thermalization hypothesis [12, 16, 17] (ETH). We will then show how many-body localized systems break the ETH and give a brief review of their phenomenology.

4.1   Themalization in classical systems

In classical statistical physics, the process of thermalization describes the relaxation of a system prepared in an arbitrary initial state to thermal equilibrium. Once a system has reached thermal equilibrium, there are no macroscopic flows of e.g. energy or atom numbers occurring and the system is in a macrostate that can be described by few macroscopic quantities (e.g. the temperature). Properties of the macrostate can be calculated by averaging over all possible microscopic realizations of the macrostate, known as the microcanonical ensemble. In closed systems, the number of microscopic realizations is

limited by the condition that they have to have an energy in the interval $E + \delta E$, where E is the total energy of the closed system and $\delta E \to 0$.

In order to reach thermal equilibrium based on the ideas above, a closed system in an arbitrary initial microstate needs to evolve such that it eventually does indeed sample all available microstates. This is for example the case if the time evolution is fully random. In this case, the probabilities of finding the system in any specific microstate will become equal for sufficiently long times and the time average of the system will become equal to the ensemble average. This property is known as ergodicity. More specifically, a system is considered ergodic if its behavior averaged over time $\hat{f}$ is equal to the average over all possible microstates $x \in X$ of the system $\bar{f}$

$$\hat{f} = \bar{f}, \tag{4.1}$$

where f is any function acting on a microscopic realization x in the ensemble of possible microstates X, i.e. an observable. The averages are defined as

$$\begin{aligned}
\hat{f}(x_0) &= \lim_{n \to \infty} \frac{1}{n} \sum_{k=0}^{n-1} f(T^k x_0) \\
\bar{f} &= \frac{1}{\mu(X)} \sum_{x \in X} f(x),
\end{aligned} \tag{4.2}$$

where T is the (discrete) time evolution operator acting on the initial realization x_0 (i.e. $x_1 \equiv x_{t=1} = T x_{t=0} \equiv T x_0$, where t denotes the discrete time). The function μ is the measure of the space of possible realizations.

The central question whether a certain classical system can thermalize thus strongly relates to the question of whether the system is ergodic. In general, most systems behave ergodically, as long as they are interacting, or more generally contain a non-linearity. However, as the Fermi-Pasta-Ulam-Tsingou experiment [149, 150] showed, this alone need not be sufficient to guarantee ergodicity. Instead, next to being interacting, systems typically need to be dynamically chaotic. In dynamically chaotic systems, the future time evolution is extremely sensitivity on the exact details of the initial state. Hence, while the dynamics is in principle deterministic, it is very hard to predict as even slight uncertainties can cause an exponentially different behavior [151]. This causes an effective randomness in the dynamics, helping the system to dynamically explore the full set of available microstates.

Note that also in classical systems the conditions for ergodicity and its role in thermalization are not finally resolved, but remain an active field of research [152].

4.2   Thermalization in quantum mechanics

As all systems are quantum, a quantum-mechanical description of generic systems necessarily needs to recover the intuitive classical result of thermalization known from everyday life. However, applying the previously discussed concepts of ergodicity and dynamical chaos to quantum mechanics is not straightforward at all. As the quantum-mechanical

time evolution under a Hamiltonian is inherently linear, dynamical chaos is absent in quantum systems [15]. Also, it is not possible to define a direct analog of classical ergodicity on the level of wavefunctions, which are the direct analog to the classical notion of microstates [153].

An analog of classical ergodicity can, however, be defined via the expectation value of observables [16, 154] as

$$\left\langle \langle \Psi_t | \hat{A} | \Psi_t \rangle \right\rangle_t = \frac{1}{D} \sum_{\alpha : E_\alpha \in [E, E+\delta E]} \langle \Phi_\alpha | \hat{A} | \Phi_\alpha \rangle, \tag{4.3}$$

where the left hand side denotes the infinite time average of the expectation value of an observable $\hat{A}$ in a quantum state $|\Psi_t\rangle$ and the right hand side the expectation value of $\hat{A}$ in the microcanonical ensemble. In equivalence to the classical microcanonical ensemble, this expectation value is calculated by averaging the expectation value of $\hat{A}$ from all eigenstates $|\Phi_\alpha\rangle$ with corresponding eigenenergies E_α in the interval $[E, E + \delta E]$, where E is the total energy of the system and $\delta E \to 0$. The principle of equal a priori probability is fulfilled by weighing contributions from all eigenstates equally with the probability $1/D$, where D is the number of eigenstates in the considered energy interval. Note that the thermodynamic limit can be taken such that D tends to infinity even though δE tends towards zero. The definition of quantum ergodicity in eq. (4.3) is a formulation of the trivial requirement that the behavior *observed* in classical systems needs to emerge from the expectation values of observables in a quantum mechanical formulation. However, as we will show below, eq. (4.3) has some highly non-trivial implications.

The left-hand side of eq. (4.3) can be explicitly derived from the time evolution of the initial state

$$|\Psi_t\rangle = \sum_\alpha c_\alpha e^{-\frac{i}{\hbar} E_\alpha t} |\Phi_\alpha\rangle \tag{4.4}$$

where the c_α are the occupations of the eigenstates. The time average can then be calculated as

$$\begin{aligned}
\left\langle \langle \Psi_t | \hat{A} | \Psi_t \rangle \right\rangle_t &= \sum_{\alpha, \beta} c_\alpha c_\beta^* \left\langle e^{-\frac{i}{\hbar}(E_\alpha - E_\beta)t} \right\rangle_t \langle \Phi_\beta | \hat{A} | \Phi_\alpha \rangle \\
&= \sum_\alpha |c_\alpha|^2 \hat{A}_{\alpha, \alpha},
\end{aligned} \tag{4.5}$$

because oscillating phases average to zero. Here $\hat{A}_{\alpha, \alpha} = \langle \Phi_\alpha | \hat{A} | \Phi_\alpha \rangle$.

The right hand side of eq. (4.3) denotes the expectation value of $\hat{A}$ in the microcanonical ensemble $\left\langle \hat{A} \right\rangle_{\mathrm{mc}}(E)$, which depends only on the energy E. This expectation value can be calculated from the microcanonical density matrix $\hat{\rho}_{\mathrm{mc}}$ as

$$\left\langle \hat{A} \right\rangle_{\mathrm{mc}}(E) = \mathrm{tr}(\hat{\rho}_{\mathrm{mc}} \hat{A}) \tag{4.6}$$

with the micro-canonical density matrix

$$\hat{\rho}_{\mathrm{mc}} = \frac{1}{D} \sum_{\alpha : E_\alpha \in [E, E+\delta E]} |\Phi_\alpha\rangle \langle \Phi_\alpha|. \tag{4.7}$$
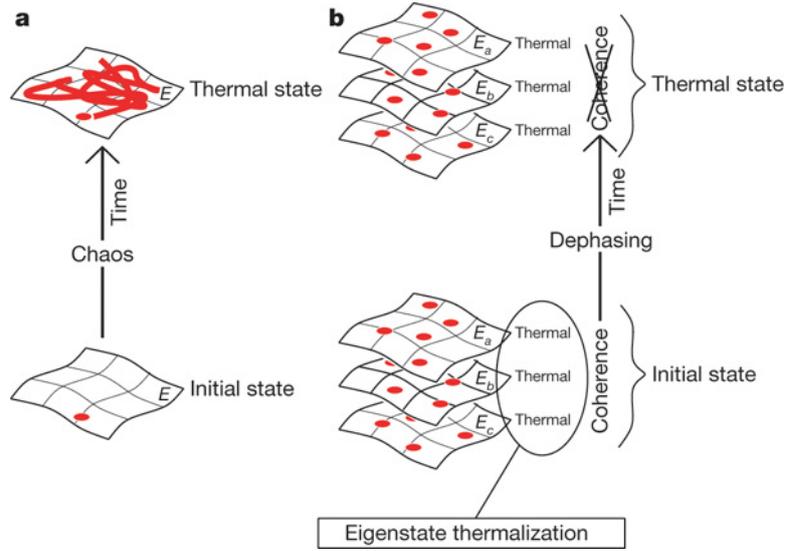
Figure 4.1: Thermalization in classical versus quantum mechanics: a) In classical mechanics thermal equilibrium emerges from chaotic dynamics. b) In quantum mechanics, according to the ETH, every eigenstate of the Hamiltonian is thermal. The coherence between the eigenstates hides the thermal nature in the initial state. During the time evolution, these coherences dephase, revealing the thermal nature. Figure reused from Ref. [12] with permission. Copyrighted by Springer Nature.

Using the calculations presented above, the definition of quantum ergodicity can be rewritten as

$$\sum_{\alpha} |c_{\alpha}|^2 \hat{A}_{\alpha,\alpha} = \frac{1}{D} \sum_{\alpha: E_{\alpha} \in [E, E+\delta E]} \hat{A}_{\alpha,\alpha}. \tag{4.8}$$

From this form the strong implications of the definition of quantum ergodicity are easily recognizable. The expression on the left hand side is heavily dependent on the initial conditions set by the c_{α}, while the right hand side only depends on the total energy. Trivially, the above equation is not necessarily true, as a randomly chosen initial state need not fulfill $|c_{\alpha}|^2 = 1/D$. With this in mind, however, eq. (4.8) can only be generically fulfilled if the expectation values $\hat{A}_{\alpha,\alpha}$ are independent of the exact eigenstate α. This idea is known as the Eigenstate Thermalization Hypothesis.

4.2.1   The Eigenstate Thermalization Hypothesis

Definition: The expectation value $\langle \Phi_{\alpha} | \hat{A} | \Phi_{\alpha} \rangle$ of an observable $\hat{A}$ in an eigenstate $|\Phi_{\alpha}\rangle$ with eigenenergy E_{α} of a large, interacting many-body Hamiltonian equals the microcanonical ensemble average at energy E_{α}

$$\langle \Phi_{\alpha} | \hat{A} | \Phi_{\alpha} \rangle = \langle \hat{A} \rangle_{\mathrm{mc}} (E_{\alpha}). \tag{4.9}$$

The Eigenstate Thermalization Hypothesis [16, 17] (ETH) states, that the expectation values of an observable $\hat{A}_{\alpha,\alpha}$ in an eigenstate $|\Phi_\alpha\rangle$ are essentially independent of the exact eigenstate and only depend on the energy. In this scenario, eq. (4.8) holds for most initial conditions. Exceptions are initial states with macroscopic uncertainties in the energy, i.e. superpositions of very high and very low energy eigenstates. The ETH implies that in quantum systems thermalization happens at the level of individual eigenstates, which are thermal themselves. Further, it directly states that the knowledge of a single eigenstate is sufficient to calculate thermodynamic expectation values. Hence, ensemble averages over all possible eigenstates are not required.

Fig. 4.1 illustrates the process of thermalization in quantum systems (assuming the ETH is true) and highlights the difference to classical systems. In classical systems, the thermal state is constructed via the dynamics. Due to dynamical chaos, the system samples possible microstates seemingly randomly, resulting in an equal probability of finding the system in any microstate after sufficiently long times. As was already mentioned before, such dynamical chaos is absent in quantum mechanics. However, in the context of the ETH dynamical chaos is not required, as the dynamics play a mere auxiliary role in the emergence of thermal equilibrium, which is already present in the individual eigenstates. While coherences hide these properties in the initial state, the time evolution dephases these coherences and the underlying thermal nature becomes visible.

While the ETH is well supported by numerical evidence (see e.g. [12] and references therein), it is important to remember that it remains a hypothesis without formal proof. Also, there are several exceptions to the ETH, e.g. restrictions on the observable $\hat{A}$, as well as on the energy density.

Conditions on observables for which the ETH holds: From the definition of the ETH in eq. (4.9) it quickly becomes apparent that the ETH will not hold for arbitrary observables $\hat{A}$. For example, the projection operator on an individual eigenstate $\hat{A} = \hat{P}_\gamma = |\Phi_\gamma\rangle\langle\Phi_\gamma|$ is clearly not thermal and not ergodic in the quantum sense, as $\hat{P}_\gamma$ in equation 4.3 gives

$$\left|c_\gamma\right|^2 = \frac{1}{D} \tag{4.10}$$

which would pose tight restrictions on the initial state. This is related to the fact that projection operators are highly non-local and reveal long-distance entanglement in the system. Indeed, the ETH only holds for local observables that are defined on a small subsystem [155]. Another way to see this is that thermalization in quantum mechanics is the thermalization of subsystems, that use the rest of the system as their bath. Initial local correlations in a subsystem will spread through the entire system, resulting in an effective dephasing in the subsystem. Hence, the subsystem's reduced density matrix will be fully mixed and observables defined in the subsystem will approach their thermal values. Considering the full system, however, correlations cannot be lost and hence appropriately chosen global observables will always be able to retrieve the information of the initial state.

Note that the locality condition on the observables does not restrict the intuitive picture of thermalization, nor the experimentally available observables in large quantum systems, as all typical and (easily) realizable observables are local (such as e.g. densities).

Restrictions on the ETH by the energy density: In this thesis, we focus on the behavior of systems in highly excited states at high energy densities. The energy density is defined as in [155] as

$$\rho_E = \lim_{V \to \infty} \frac{E - E_0}{V}, \tag{4.11}$$

where E_0 is the energy of the ground state and V the Volume of the system. Note that a high energy density is essentially equivalent to a high temperature. However, the temperature is only well defined in thermal systems, and hence the concept of energy density is more practical.

At finite $\rho_E \neq 0$, the ETH is expected to hold for large system sizes. However, the ground state and low lying excitations over the ground state, with an energy density of $\rho_E = 0$ often explicitly violate the ETH. This is because the ground states often exhibit spontaneously broken symmetries, like e.g. a ferromagnetic spin system. Its ground state exhibits a spontaneous symmetry breaking in that it chooses to be either spin-up or spin-down. Once it chose an alignment, however, it will not explore the other alignment even though both states are equally energetically favorable. Ergodicity would thus require that the system explores both cases. Low lying excitations to this ground state can be expressed as the sum of few spin-flip terms. Such excitations still have an energy-density of zero and do clearly not result in thermalization. Only when the excitations are high enough that the number of required spin-flip operators becomes extensive will the energy-density become finite and the system will thermalize.

4.3   Integrable systems

While the overwhelming majority of systems thermalizes, exceptions occur e.g. in integrable systems. Integrable systems present fine-tuned exceptions to thermalization in the sense that even small changes in the Hamiltonian will restore a thermalizing behavior. In classical mechanics, integrable systems are characterized by the existence of an extensive amount of integrals of motion, which restrict the dynamics of the system and thus prevent thermalization. A well-known example of such a system is Newton's cradle.

In quantum mechanics, integrability is much harder to define than in the classical sense. Especially, the classical definition of having an extensive set of conserved quantities trivially fails, as in quantum mechanics these could be constructed by the projectors on eigenstates, making every quantum system integrable. In fact, a commonly agreed upon definition of integrability in the quantum sense is lacking. A review of common definitions and their (dis)advantages can be found in Ref. [156]. In general, all non-interacting systems are integrable, as it is usually easy to diagonalize their Hamiltonians via Fourier transformations. Other integrable models are usually characterized by the existence of

many non-trivial integrals of motion that have a significant effect on the dynamics of the system.

Note that while some integrable systems simply show oscillations up to infinite times, most integrable systems do show a relaxation to an equilibrium state similar to thermal systems. The difference lies in the equilibrium state, which is not describable by the microcanonical ensemble, but instead by the generalized Gibbs ensemble [157–159] which takes the restrictions in the dynamics into account. Such systems are non-thermal in the sense that local observables can be found that have non-thermal values. However, it is possible that most local observables still do take their thermal values. A special, and for this thesis directly relevant, example of such an integrable system is the one-dimensional Fermi-Hubbard model.

Integrability in the Fermi-Hubbard Hamiltonian: The one-dimensional Fermi-Hubbard Hamiltonian (or simply Hubbard Hamiltonian [91])

$$\hat{H} = -J \sum_{\langle i,j \rangle} \sum_{\sigma} \hat{c}_{i\sigma}^{\dagger} \hat{c}_{j\sigma} + U \sum_{i} \hat{n}_{i\uparrow} \hat{n}_{i\downarrow} \qquad (4.12)$$

models the hopping J of fermions with on-site interactions U in a one-dimensional lattice. It is not only integrable at $U = 0$ but was shown to be integrable at all U [160, 161] in the sense that it can be solved using the Bethe-Ansatz [162].

The Hubbard Hamiltonian is of special interest for this thesis, as both the interacting Anderson and the AA model reduce to the Fermi-Hubbard Hamiltonian in the absence of disorder/detuning. Hence, it is important to understand how the integrability of the underlying model affects the investigations of localization due to detuning. First, it is important to note that the addition of disorder or detuning breaks the integrability of the Hubbard Hamiltonian. Hence, the integrability can only affect the measurements in (and close to) the limits of zero detuning. We will first consider the case of $U = 0$. In this limit, the Hamiltonian can be diagonalized via a Fourier transformation and the conserved quantities are the quasi-momenta. It is easy to see that while these restrictions will stop a full thermalization, the relaxation of a real-space pattern (i.e. a charge-density wave) should not be affected. In the presence of interactions, the conserved quantities come from a solution from the Bethe Ansatz and are not easily visualizable. However, as in the non-interacting case, there are no restrictions on the relaxation of density patterns.

4.4   Many-body localization

Another, more generic, exception to thermalization occurs in systems with a sufficiently strong disorder/detuning [22–24], known as many-body localization (MBL). Here, 'more generic' means that small changes of the Hamiltonian will indeed not restore a thermalizing behavior. MBL can be considered as the interacting generalization of single-particle localization discussed previously. However, thermalization of interacting systems is a much

more robust phenomenon than the relaxation of single particles, and hence the existence of localization in the presence of interactions is a much more surprising result. Indeed, it is generally found that in the presence of interactions much higher disorder/detuning strengths are required to localize a system. Note that MBL explicitly considers localization in high energy density states, as ground states might be non-thermal even in non-disordered systems.

First evidence for many-body localization was obtained through perturbative arguments. Starting from fully localized states in heavily disorder systems with no tunneling ($J = 0$), weakly hybridized many-body states can be constructed via perturbation theory in J and U [163–165]. Comparing the level spacing to the coupling J results in the conclusion that e.g. energy transport is absent and hence the system is localized. Later, numerical simulations established the existence of MBL over a much wider range of parameter regimes [23, 29, 166].

As was discussed in section 4.3, breaking of quantum ergodicity is not an exclusive feature of many-body localization, but also occurs in integrable systems. In these systems, the breaking of ergodicity is associated with the presence of an extensive set of conserved quantities. A similar structure of conserved quantities can also be constructed in MBL systems. However, while in integrable systems the conserved quantities only restricted full thermalization, the conserved quantities of a localized MBL system need to actually prevent changes in the density pattern. Such a constraint is not present for generic integrable systems, which may relax in real-space but be non-ergodic in a different sense (as e.g. the Fermi-Hubbard model).

The idea of such an emergent integrability in MBL systems was substantiated in Refs. [25, 26, 167] (and reviewed in Ref. [27]). In these references, it was shown that MBL Hamiltonians can be written as a non-linear function of a complete set of *local* integrals of motion (so called LIOMs $\hat{I}_\alpha$). The Hamiltonian then takes the form

$$\hat{H} = h_0 + \sum_\alpha h_\alpha \hat{I}_\alpha + \sum_{\alpha,\beta} h_{\alpha,\beta} \hat{I}_\alpha \hat{I}_\beta + ..., \tag{4.13}$$

where the dots indicate the presence of higher order terms up to infinite order. While this expansion is in principle generic, only for MBL systems it implies a locality of both the $\hat{I}_\alpha$ and the coefficients h. The operators $\hat{I}_\alpha$ are local in the sense that if expanded in terms of the local operators in the Hamiltonian $\hat{O}$ (i.e. expanded in terms of annihilation and creation operators)

$$\hat{I}_\alpha = \sum_i A_i^{(\alpha)} \hat{O}_i \tag{4.14}$$

the amplitudes A_i decay exponentially as a function of the distance d from a certain point in space around which the operator acts, i.e.

$$|A_i| \sim e^{-d/\xi}, \tag{4.15}$$

where ξ is a length scale describing the spatial extent of the operator. Hence, the $\hat{I}_\alpha$ are only weak deformations of the local operators $\hat{O}$.

Due to the locality of the $\hat{I}_\alpha$, also the $h_{\alpha,\beta}$ in eq. (4.13) decay exponentially with the distance between the two operators $\hat{I}_\alpha$ and $\hat{I}_\beta$. Additionally assuming that the $\hat{I}_\alpha$ have a binary structure (like spin degrees of freedom) is indeed sufficient to derive the full phenomenology of strongly localized MBL systems [27]. Note though, that the presented description via LIOMs is only useful deep in the localized phase as it cannot be applied close to the phase transition.

4.4.1 Phenomenology of MBL

In this section, we discuss some signatures of many-body localized systems used in theory and experiment. Note that the given list is not complete, but only a mentioning of the most important observables. Further observables are e.g. a direct violation of the ETH or the absence of level repulsion [166].

Eigenstate entanglement: In the theoretical analysis of many-body localization, where the eigenstates of a system can be accessed, a classification between a thermal and an MBL system can be performed based on the entanglement scaling of the eigenstates [29]. The entanglement can be characterized by the von Neumann entanglement entropy.

$$S(t) = -\mathrm{Tr}(\hat{\rho}\log(\hat{\rho})), \tag{4.16}$$

where $\hat{\rho}$ denotes the density operator. While the entanglement of the full eigenstate is zero, as it is a pure state, the entanglement S_A of a subsystem $\hat{\rho}_A$ will scale with the size of the subsystem L_A^d, where d denotes the dimensionality. Thermal systems at elevated temperatures will typically show eigenstates with a volume-law entropy, i.e. $S_A \sim L_A^d$. Intuitively, this implies that entanglement spreads through the entire system. In contrast, many-body localized systems (and single-particle localized systems) show area-law entanglement $S_A \sim L_A^{d-1}$. The scaling of the entanglement entropy with the boundary of the subsystem implies that entanglement only spreads over short distances, and two distant points are not entangled, which is consistent with the picture of localization.

Note that for the analysis of the eigenstate entanglement it is important to work at elevated temperatures. The behavior in the ground state can be vastly different as area-law scaling occurs even in non-disordered systems [168].

Out-of-equilibrium dynamics: While theoretical calculations can identify violations of the ETH by simply looking at many-body eigenstates, considering local observables a localized system can only be distinguished from a thermal system via its out-of-equilibrium dynamics after a quench. This becomes obvious when considering a thermal and a localized system, each prepared in a thermal equilibrium state. Measurements of local quantities will, in both cases, return thermal values. Also, the states will not change under time evolution, as the thermal system already is in equilibrium and the localized system is localized. To distinguish localized from thermalizing systems, it is thus required to prepare an initial state far from thermal equilibrium (i.e. a state with large local differences
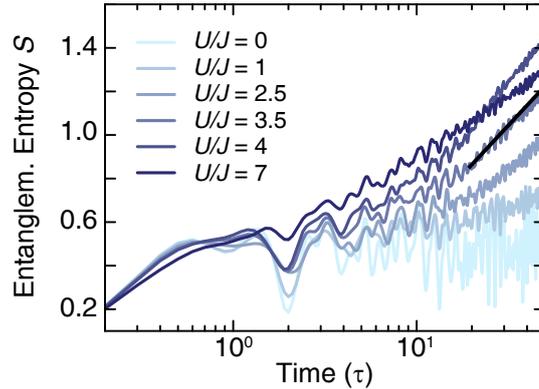
Figure 4.2: Time-evolution of the entanglement entropy: Growth of the entanglement entropy with time at a detuning strength of $\Delta = 5\,J$. The calculations have been performed for a Aubry-André Hubbard model. At long times, a logarithmic growth is visible. In a non-interacting system ($U = 0$) the entanglement entropy S does not grow. Calculations were performed by Ronen Vosk, Mark Fischer and Ehud Altman [43].

in energy or atom number) and monitor its time evolution. While thermalizing dynamics will tend towards a thermal equilibrium state, the time evolution in a localized system preserves a memory of the initial state (see e.g. [37, 166, 169, 170]). This also means that e.g. the expansion of a cloud in a localized system must be zero and local patterns like the charge-density wave employed for measurements of the imbalance are preserved.

Time evolution of the entanglement entropy: Another experimentally inaccessible, but theoretically often used observable to characterize many-body localized states is the time evolution of the entanglement entropy starting from an unentangled initial state. This is often a more sensitive probe than the monitoring of the out-of-equilibrium dynamics of local quantities, as the key signature of MBL systems is a logarithmic growth of $S(t)$ as compared to the simple absence of dynamics. Also, it is numerically more accessible than a full computation of the many-body eigenstates.

The time evolution of the entanglement entropy has most often been used in one-dimensional systems and the subsystem is typically chosen such that $L_A = L/2$, where L denotes the length of the entire system. In non-disordered/detuned thermal systems, typically a ballistic growth of the entanglement was observed, i.e. $S_A(t) \sim t$ [171–173]. Note that this growth of entanglement typically saturates after a certain time to a maximum value, which scales with the volume of the subsystem (see section 4.4.1).

In many-body localized systems, the growth of the entanglement entropy was found to be logarithmic in time $S_A \sim \log(t/\tau)$ [174, 175]. An example of this is illustrated in Fig. 4.2. Here, the entanglement entropy was calculated in the setting of an interacting Aubry-André model at a detuning strength of $\Delta = 5\,J$ for various interaction strengths. At long times, the logarithmic growth of S is clearly visible for all interaction strengths except

for $U = 0$, where S does not grow in time. Note that in the single-particle extended phase the entanglement entropy would grow due to particle transport. A detailed investigation of the entanglement entropy was performed in Ref. [175], where the growth of the entanglement entropy was found to be unbounded. Saturation only occurs after exponentially long times, and the saturation values follow a volume law, a behavior expected for thermal systems. However, the saturation values are still sub-thermal. A naive interpretation of this behavior can be given as interactions causing a scrambling of phases through the entire system. However, this does not actually result in the movement of particles and hence the system remains localized.

Observing localization in interacting systems

This thesis reports on two experiments on many-body localization of interacting particles. The first experiment investigates the MBL-to-ergodic phase transition in chapter 6 (Ref. [108]), the second experiment is a controlled study of MBL in open quantum systems in chapter 7 (Ref. [70]). Both experiments have been performed in the context of the AA-model (at a primary lattice depth of $V_p = 8\,E_r^p$). An outlook on interacting experiments at lower primary lattice depths, where an SPME is present, will be given in section 8.1.1.

In this chapter, we discuss the differences and challenges of studying interacting many-body systems compared to studying single-particle physics. We further give some basic results on many-body localization in our experimental setup as a basis for the following chapters.

5.1 Modelling the interacting system

Both the Anderson (section 2.3.3) and the AA Hamiltonian (section 2.3.1) can in principle be easily modified to include interactions by adding the standard on-site interaction term commonly used in Hubbard models, i.e.

$$\hat{H} = \hat{H}_{sp} + \hat{H}_U, \quad \hat{H}_U = U \sum_i \hat{n}_{i,\uparrow} \hat{n}_{i,\downarrow}, \tag{5.1}$$

where $\hat{H}_{sp}$ denotes the single-particle Hamiltonian describing either the Anderson or the AA model. The interaction term adds an energy of U if two Fermions of opposite spin occupy the same lattice site. In the absence of any disorder/detuning, the interacting Anderson or AA Hamiltonians are both equivalent to the Fermi-Hubbard Hamiltonian (equ. (4.12)).

Numerically studying the interacting Hamiltonian is much harder than simulating the corresponding non-interacting Hamiltonians, as numerical tools struggle with the large Hilbert space of the many-body system. Especially, exact diagonalization studies are limited to approximately 20 lattice sites, and approximate methods such as DMRG work only deep in the localized phase.

5.1.1   Hubbard versus spin systems

A useful method for reducing the size of the Hilbert space in numerical studies is to consider spin systems instead of Hubbard models. Spin models describe qualitatively the same physics as the Hubbard models, but quantitative differences emerge due to differences in the interaction term. The most common spin-model used to study localization is the XXZ-Hamiltonian, which models the behavior of spin one-half particles fixed to specific lattice sites with overall filling one. Hence, the local Hilbert space of an individual lattice site has only two possible states (spin-up or spin-down) instead of four as in the Hubbard models (empty, spin-up, spin-down, spin-up and spin-down). The behavior of the spins is described by the Hamiltonian

$$\hat{H} = J_\perp \sum_i \left(\hat{X}_i \hat{X}_{i+1} + \hat{Y}_i \hat{Y}_{i+1} \right) + J_z \sum_i \hat{Z}_i \hat{Z}_{i+1} + \Delta \sum_i V_i \hat{Z}_i, \qquad (5.2)$$

where $\hat{X}, \hat{Y}, \hat{Z}$ denote the Pauli spin operators. The first term of the Hamiltonian swaps neighboring spins and corresponds to the hopping term in the Hubbard models. The second term corresponds to the interaction term. It adds an energy J_z if two Fermions with equal spins sit on neighboring lattice sites. Note that in contrast to the Hubbard Hamiltonians, the interactions are not on-site, but instead nearest-neighbor. The last term adds the disorder/detuning potential of overall strength Δ with the V_i being either random or quasi-periodic. The typical choice of the interaction strength in this model is $J_\perp = J_z = 1$. As for numerical simulations, $J_\perp$ is simply a normalization, this choice of J_z corresponds to fixing the interaction strength to $U = J$ in the Hubbard models.

The XXZ-model can be mapped to a Hubbard type Hamiltonian via the Jordan-Wigner transformation [176]. However, the resulting Hubbard Hamilton differs from the Hamiltonians describing the experimental system in several aspects: It describes spinless Fermions instead of spinful Fermions, the particle number is fixed to $L/2$, where L is the system size, and the interactions are nearest-neighbor. In this setting, it becomes clear, that the XXZ-model describes qualitatively similar physics as the Hubbard models in eqs. (2.17), (2.4). This is especially true in the absence of interactions, where no differences are expected.

Numerical simulations for our system are always performed on Hubbard models. However, stand-alone theoretical studies usually prefer spin-models. In comparing the presented experimental results to such studies, quantitative differences in e.g. the exact transition point are expected. Qualitatively, however, the described physics is expected to be similar.

5.1.2   SU(2)-symmetry in the Hubbard model

In Hubbard type systems, interactions are only possible between fermions of different spins, as interactions are on-site and two fermions of the same spin cannot occupy the same lattice site. Implementing an interacting system thus requires the addition of a second spin component. However, the second spin component comes with a subtle problem

that results in the absence of full MBL in Hubbard systems [177, 178]. Specifically, the detuning pattern is typically not spin-dependent, enabling a resonant switch of two fermions on neighboring sites even if the two sites are heavily detuned. This process constitutes a bath to the system, which will result in the eventual thermalization of the system.

Full MBL in a Hubbard system thus requires disabling the described spin bath via e.g. spin-dependent detunings/disorder. From an experimental perspective, however, this is not necessary as the timescale of thermalization associated with the spin bath [177] is much longer than the typical system lifetimes of the experimental platforms [69, 70]. Thus the spin-bath only plays a minor role in the more general problem of creating experimental systems that are isolated from their environment as well as possible.

5.2 Implementing interactions experimentally

Generalizing the single-particle measurements described in part I to interacting systems is in principle straight-forward. Instead of loading a spin-polarized atom cloud, a spin-mixture is required to allow the ultracold fermions to interact (see section 2.2.1). In our experiments, the interactions occur between the two lowest hyperfine states of ^{40}K $|F, m_F\rangle = |9/2, -9/2\rangle \equiv |\downarrow\rangle$ and $|9/2, -7/2\rangle \equiv |\uparrow\rangle$. Typically, the spin states are prepared in a 50/50 mixture. The interaction strength U is given by

$$U = \frac{4\pi\hbar^2 a}{m} \int d^3\mathbf{r} \, |w(\mathbf{r})|^4, \qquad (5.3)$$

where a denotes the s-wave scattering length, m the mass of ^{40}K and w a Wannier function. The scattering length can be experimentally tuned via a Feshbach resonance by slightly varying the magnetic field around $\sim 200\,\text{G}$ [100]. At primary lattice depths of $V_p = 8\,E_r^p$, which is used for all interacting measurements in this thesis, interaction strengths of $U/J \in [-20, 20]$ are easily accessible. At $|U/J| = 20$ the Fermions behave much like hardcore particles and a further increase of the interaction strength will not change their behavior.

While implementing an interacting system is thus rather straightforward, in the presence of interaction several aspects have to be considered that were not relevant in the single-particle case, which will be discussed in the following sections.

5.2.1 The interacting initial state

In the interacting AA-Hamiltonian, the only parameter that needs to be considered in addition to those in the single-particle case is the interaction strength U. However, in the presence of interactions, the imbalance is actually influenced by many more parameters than just the detuning strength Δ and the interaction strength U. This quickly becomes apparent when e.g. considering the atom number density of the initial state: If the density is reduced, the effects of interactions are reduced until in the extreme case of very low densities the system should behave essentially non-interacting. Another similar effect is
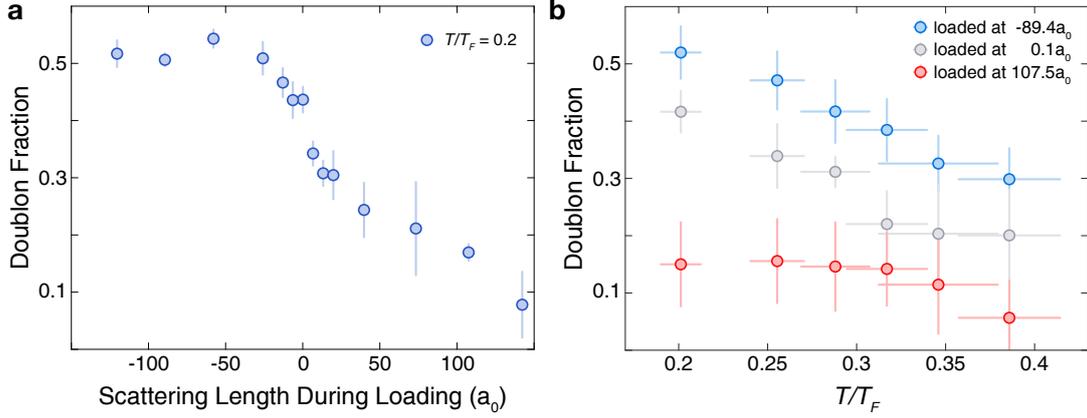
Figure 5.1: Control over the doublon fraction in the initial state: a) Doublon fraction as a function of the scattering length while the atoms are loaded into the lattice. Prior to being loaded into the lattice, the cloud had a temperature of $T/T_F = 0.2$ in the dipole trap. b) Doublon fraction as a function of temperature in the dipole trap for various scattering lengths during loading. Errorbars show the standard deviation.

present due to the distribution of spins in the initial state. Since equal spins cannot interact with each other, clusters of just a single spin species would behave non-interacting, which is in stark contrast to e.g. the expected behavior of a Néel state. Also, numerical studies generally find a strong dependence of the localization transition on the energy density (see e.g. [170]). Meaningful statements about many-body localization thus require a detailed description of the initial state. In our setup, the initial state can be influenced via three control parameters: The atom number, the temperature (entropy) of the atom cloud, and the scattering length while loading into the lattice. The key parameter characterizing the initial state is the overall atom number density, the distribution of spins and the number of doubly occupied lattice sites (doublons).

Atom number density: Throughout all experiments described in this thesis, the initial atom number was kept fix at about $N \approx 100 \times 10^3$. At our lowest achievable temperatures, this results in a filling of the central tube, which has a length of about 200 sites, with about 80 atoms. Note that half of the sites must be empty due to the charge-density wave initial state. As this already corresponds to a rather low density, no measurements were performed with a further reduced initial atom number. The density can additionally be influenced by the temperature of the atom cloud, as the temperature changes the cloud size. As higher temperatures correspond to lower densities, usually only the lowest possible initial temperatures of about $T = 0.15\,T_F$ to $T = 0.2\,T_F$ were employed.

Spin distribution: Even the lowest initial temperatures achieved in our experiments are high compared to the exchange interactions $\sim 4J^2/U$. Hence, we do not expect any corre-

lations between spins to emerge during the loading of the optical lattice. The distribution of spins is thus fully random.

Doublon number: Even at the fixed atom numbers and temperatures of our initial state, we can drastically change the behavior of the system by controlling the number of doubly occupied lattice sites (doublons). The number of doublons can be measured experimentally by comparing a direct measurement of the atom number to a measurement performed after ramping across the Feshbach resonance (i.e. the singularity in the interaction strength U) between the two spin states in our system. Ramping across the Feshbach resonance will convert any pair of atoms sitting on the same lattice site into a molecule [100]. As the molecular transitions are detuned relative to the imaging frequency of individual atoms, atoms paired up in molecules will not appear on the image. The relative difference in atom number between the two images then gives the doublon fraction. Fig. 5.1a shows the experimental control of the doublon fraction as a function of the interaction strength during the loading of atoms into the lattice. Additionally, the effect of the temperature of the atom cloud in the dipole trap is shown in Fig 5.1b. At the lowest reached temperatures of $T/T_F = 0.2$, we can achieve doublon fractions of about 50 %. Repulsive interactions can suppress the doublon fraction down to about 10 %. If the atoms are loaded non-interacting, about 40 % are doublons. As a function of temperature, we observe that lower temperatures greatly favor the formation of doublons. However, for repulsive interactions, the achievable doublon fraction remains low even at the coldest temperatures. We note, that the interaction strengths are a much cleaner way of adjusting the doublon fraction, as the initial temperature changes not only the doublon fraction but also significantly enlarges the in-situ cloud size, thereby reducing the density.

5.2.2 Observables

In principle, both the imbalance, as well as the expansion are able to characterize localization in the interacting system in the same way as in the absence of interactions. However, especially the expansion requires more care in the interpretation of the data, as the expansion speeds can heavily depend on the interaction strength even in the absence of the detuning lattice [105, 133, 179]. An exemplary measurement of the interacting expansion after $3000\,\tau$ at a primary lattice depth of $V_p = 4\,E_r^p$ is shown in Fig. 5.2. As is illustrated there, we generally find that we cannot resolve an interaction effect in the experimental expansion data. However, measurements of the imbalance (section 5.3) indeed show a sizable interaction effect in good agreement with numerical results. Why this effect is not visible in the expansion data is not quite clear. Possible reasons could be that the expansion dynamics in the many-body delocalized (but single-particle localized) phase are much slower than in the single-particle extended phase, and are hence not resolvable on the experimental timescales. Another possible reason could be that such dynamics are influenced even more strongly by any inhomogeneities in the global potential. Since the
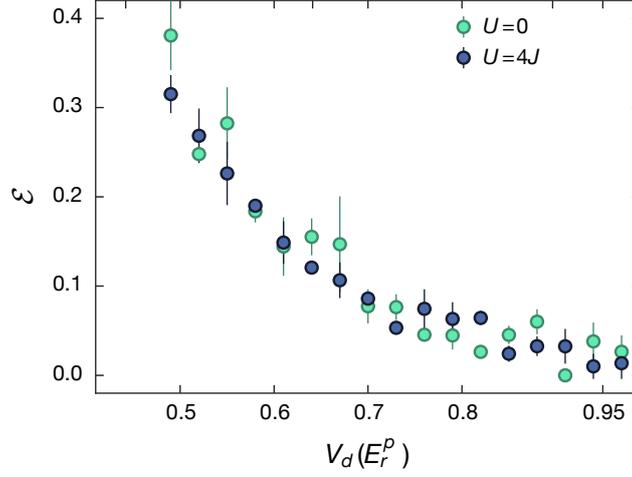
Figure 5.2: Interacting versus non-interacting expansion: Expansion $\mathcal{E}$ after $3000\,\tau$ at a primary lattice depth of $V_p = 4\,E_r^p$ as a function of the detuning lattice depth V_d. The interacting data is shown at an interaction strength of $U = 4\,J$. Points are averaged over six realizations of the detuning pattern, errorbars denote the standard deviation of the individual measurements.

reasons are unclear, we decide to not use the expansion for the interacting system, and hence all interacting results will be only obtained from the imbalance.

In the context of interacting many-body systems, the functionality of the imbalance as a probe for localization can be understood by considering localization as the opposite of thermalization. A thermalizing system prepared in an arbitrary initial state should relax back to thermodynamic equilibrium under its intrinsic time evolution. In this thermodynamic equilibrium state, local observables, like e.g. the density on a specific lattice site, are given by the microcanonical ensemble. As the quasiperiodic system does not break any symmetry between even and odd sites, this means that the expectation value of the density between even and odd sites should be equal. Hence, in a thermalizing system, the initial density pattern should vanish and the imbalance tends to $\mathcal{I}_{\text{thermal}} = 0$. Should the system, however, be many-body localized, parts of the initial density pattern can remain and give a finite imbalance $\mathcal{I}_{\text{MBL}} > 0$. Note that it is essentially impossible to show that a system is actually thermal, as this would require one to show that all local observables are thermal. The opposite is, however, not true: A single local observable yielding a non-thermal value is sufficient to show the absence of thermalization.

While it is conceptually correct to consider localization as the opposite of thermalization for the generic quasiperiodic system, care needs to be taken when no detuning is present. In this limit, the system is described by the Fermi-Hubbard Hamiltonian [91], which is integrable at all interaction strengths. However, while the present integrals of motion prevent a full thermalization in this limit, they do not prevent the relaxation of the imprinted density pattern, and hence this peculiarity has no effect on the measurements.
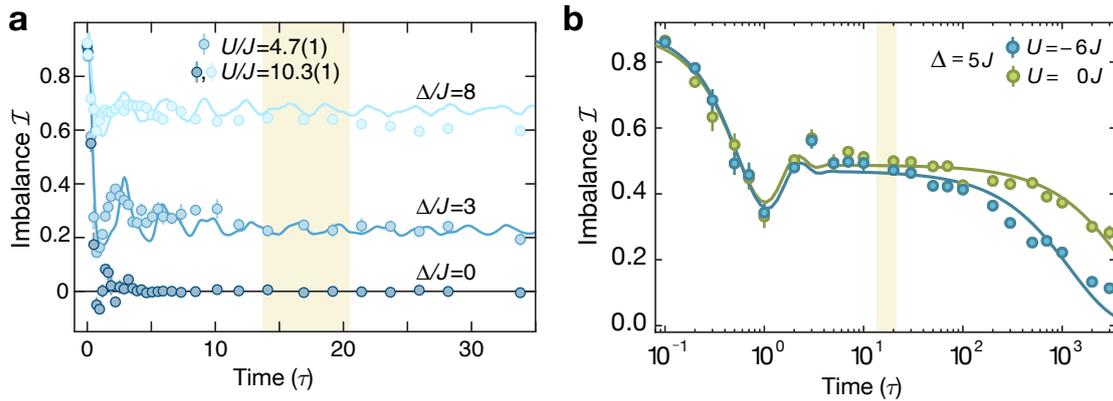
Figure 5.3: Interacting time traces: a) Time traces at various interaction U and detuning Δ strengths. Points indicate experimental measurements, averaged over 6 detuning realizations ϕ. Errorbars denote the standard error of the mean. Solid lines are the result of DMRG simulations. The yellow shaded region marks the times used to extract the equilibrium value of the imbalance. b) Long-term time traces of the imbalance at a detuning strength of $\Delta = 5\,J$ for the interacting and the non-interacting system. Solid lines are guides-to-the-eye. The decay on long timescales is due to external couplings thermalizing the system. DMRG simulations are performed by Ronen Vosk, Mark Fischer and Ehud Altman [43].

5.3 Experimental results on many-body localization

In this section, we will present some basic experimental results on the interacting system, obtained from measurements of the imbalance. We will show that the time evolution of the imbalance behaves qualitatively similar to that in the single-particle case and map out the phase diagram of the interacting Aubry-André model using a finite-time analysis. Further, we will show how strongly the system is affected by changes in the initial state. Note, however, that the finite-time analysis used in this chapter can give inaccurate results in some regimes. Especially, close to the localization transition an analysis of the dynamics is required as performed in chapter 6.

5.3.1 Time evolution of the imbalance

Exemplary time traces for various interaction and detuning strengths are shown in Fig. 5.3. For these traces, the initial state contains approximately 40 % doublons. We observe a generally similar behavior as in the absence of interactions: At $\Delta = 0$, the imbalance quickly decays to zero, whereas in the presence of finite detunings, it equilibrates to a finite steady-state value. This already strongly suggests that localization can indeed persist in the presence of interactions.

We compare the experimental data to theoretical Time-Evolving-Block-Decimation (TEBD) simulations [180], which model the experimental system on 40 sites. The simulations model the details of the experimental initial state, but neglect the effects of the

dipole trap and averaging over many tubes. Note that TEBD simulations are a viable tool only when the entanglement in the system spreads slowly, i.e. in the localized phase. The shown simulations at $\Delta = 3J$ are a borderline case of what is numerically possible. We find very good agreement between the theoretical and experimental time traces, which both suggest that localization will indeed survive in the presence of interactions. However, a slight disagreement is observed between the traces at $\Delta = 8J$. Here, the experimental data seems to indicate a slow decay on a longer timescale, that is not present in the simulations. This is due to the experiment coupling to its environment, which acts as an external bath, ultimately thermalizing the system on long timescales. We find a general reduction of the imbalance lifetime in the presence of interactions, as compared to the non-interacting case (see Fig. 5.3b). External couplings thus seem to be more effective in interacting systems [69, 70].

Due to the limited lifetime of the interacting imbalance, a characterization of the phase diagram via the stationary state requires measurements after a short evolution time, which we choose to be about $20\,\tau$. Note though, that the short evolution time implies finite-time limitations. A good understanding of the basic features of the interacting Aubry-André model can nevertheless be achieved from these steady-state imbalances.

5.3.2   Phase diagram of the interacting AA-model

The phase diagram resulting from the finite-time measurements of the imbalance is shown in Fig. 5.4a over a wide parameter range of both Δ and U. The measurements have been performed at a doublon fraction of approximately 40%. Exemplary traces of the stationary imbalance versus the interaction strength are shown in Fig. 5.4b, together with the results of TEBD simulations where possible.

The dominant observable feature is the increase of the stationary imbalance from close to zero in the delocalized (blue) phase to finite values when the detuning Δ becomes sufficiently large. This is observable at all interaction strengths U, showing that a localized phase exists independent of the interaction strength. The effect of interactions is much weaker and highlighted via equal-imbalance lines (dashed white). They clearly show, that at intermediate interactions ($U \sim 5J$) a slightly larger detuning strength is required to achieve the same imbalance as at $U = 0$. Upon further increasing the interaction strength, the detuning strength required for the same imbalance decreases again and, in the hard-core regime, is slightly lower than at $U = 0$. This trend along the interaction strength is symmetric around $U = 0$, resulting in a 'W'-shape of the stationary imbalance along U, which is observable in Fig. 5.4b. This symmetry emerges from a dynamical symmetry in the Fermi-Hubbard Hamiltonian between negative and positive interactions for initially localized particles [105], which survives in the presence of the detuning [43]. The minima of the 'W'-shape move to higher interaction strengths as Δ is increased. The depth of the 'W'-shape decreases deep in the localized phase, indicating that the role of interactions is most pronounced close to the transition, but decreases deep in the localized phase.
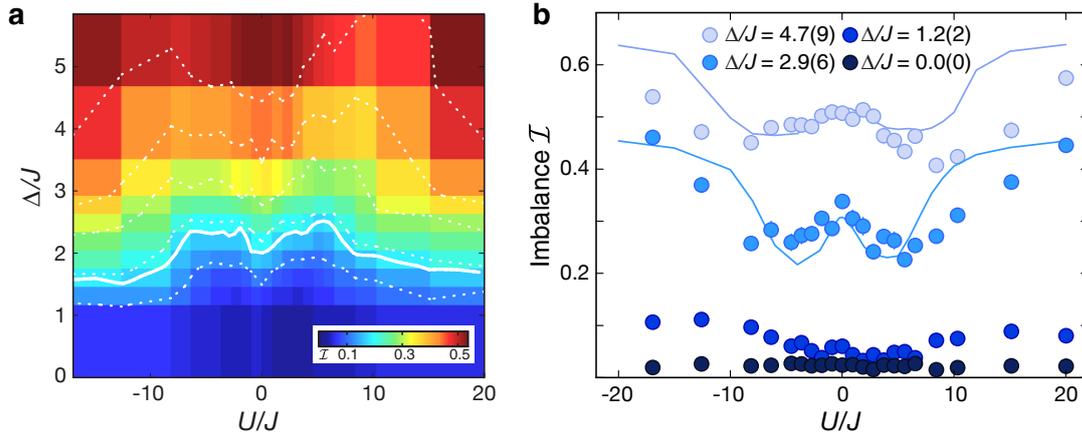
Figure 5.4: Phase diagram: a) Experimental phase diagram extracted from the steady-state imbalance versus the detuning strength Δ and the interaction strength U. The initial state contained approximately 40 % doublons. White lines are equal-imbalance lines, illustrating the effect of interactions. The solid white line denotes the best guess for the phase transition, based on the imbalance of the non-interacting system at $\Delta = 2\,J$. b) Exemplary traces of the stationary imbalance as a function of U, taken from the phase diagram. Solid lines indicate the result of TEBD simulations. All experimental data is averaged over three times (close to $20\,\tau$), and over 4 realizations of the detuning pattern. Errorbars denote the standard error of the mean. TEBD simulations are performed by Ronen Vosk, Mark Fischer and Ehud Altman [43].

These observations suggest, that interactions do indeed destabilize the localized phase in the sense that a larger detuning strength is required for localization at intermediate interactions as compared to the non-interacting case. The decreasing critical detuning strength in the regime of hardcore interactions can be understood from an effective particle description of the present doublons. When the interaction strength U exceeds twice the bandwidth, i.e. $U > 8J$, doublons become new, bound quasi-particles. These quasi-particles exhibit a reduced effective tunnel coupling strength of $J_{\text{eff}} \sim J^2/U \ll J$. Hence, their effective detuning strength Δ/J_{eff} is much larger. As only about 40 % of particles are doublons, the system close to the transition is hence composed of particles that are delocalized and doublons that are localized. Since these particles can interact with each other, the resulting dynamics might be both very complex and very slow. Hence, the short time analysis presented here might not capture the full picture and, for simplicity, doublons are not considered in the following chapters. A more detailed analysis of the doublon dynamics can be found in Ref. [114].

From the phase diagram, it is not immediately obvious where the phase transition between the thermal and the localized system occurs, as the transition is smoothed out by the dipole trap. However, an estimate of the critical detuning strength can be made based on the steady-state imbalance of the non-interacting system at $\Delta = 2J$. Specifically, we estimate the transition as an equal imbalance line starting from this point. This line is illustrated by the solid white line in Fig. 5.4a and shows the characteristic 'W'-shape.
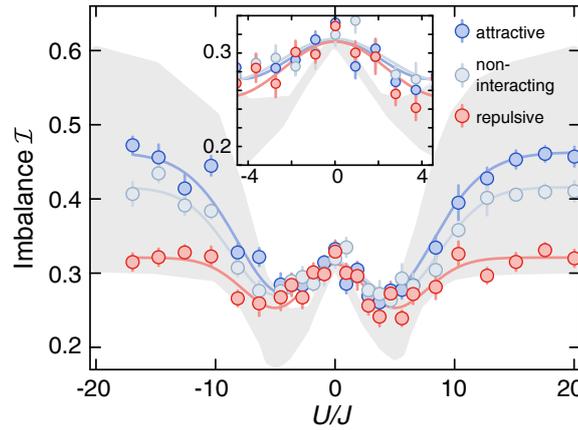
Figure 5.5: Effect of doublons on the steady-state imbalance: Stationary imbalance $\mathcal{I}$ as a function of the interaction strength U at a detuning strength close to the transition of $\Delta = 3\,J$. Curves are shown for attractive ($a_{\mathrm{load}} \sim -90\,a_0$), non-interacting and repulsive ($a_{\mathrm{load}} \sim 140\,a_0$) interactions during the loading of the lattice, resulting in doublon fractions of about 50 %, 40 % and 10 %. The data is averaged over 3 times and 4 phases (as in Fig. 5.4). Errorbars denote the standard error of the mean. The gray shading indicates the results of TEBD simulations for the limiting cases of 50 % and 0 % doublons. The inset shows a zoom into the region of small interaction strengths. TEBD simulations were performed by Ronen Vosk, Mark Fischer and Ehud Altman [43].

However, as will be discussed in chapter 6, the short-time analysis presented in this chapter is insufficient to correctly capture the behavior of the interacting system close to the phase transition, as in this regime slow dynamics are present. Hence this estimation of the critical detuning strength is rather inaccurate.

5.3.3   Effect of the initial state

In the previous section, a measurement of the full phase diagram was shown at a doublon fraction of about 40%. In this section, we will show measurements highlighting how features of this phase diagram change with the initial state.

Effect of doublons in the initial state: To gain a better understanding of the effects of doublons, we consider the stationary imbalance for strong attractive interactions, giving about 50 % doublons, strong repulsive interactions resulting in about 10 % doublons and the non-interacting loading as discussed until now. We will focus on a detuning strength of $\Delta = 3J$, where interaction effects are observed most dominantly. Note that in chapter 6 we will find that at this detuning strength the system is likely still delocalized at intermediate interaction strengths. As the thermalization timescales are, however, very long, for the short-time analysis presented here, the system well approximates the behavior of a localized system. Fig. 5.5 shows traces of the stationary imbalance $\mathcal{I}$ along the interaction strength U for the three different loading interactions. In all three cases, the
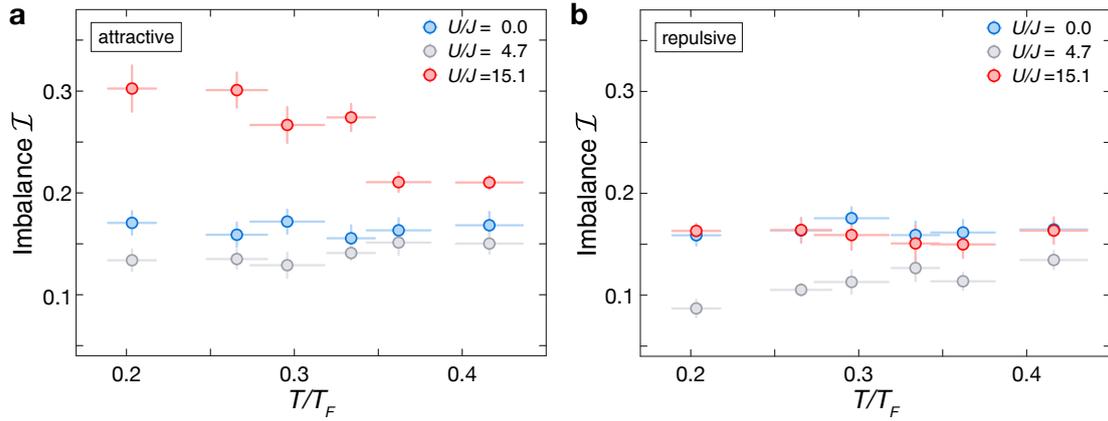
Figure 5.6: Effect of the temperature of the initial state: Stationary imbalance as a function of the temperature of the cloud before loading it into the optical lattice for a) attractive and b) repulsive loading interactions. Data is shown for the three regimes of interaction strengths: Non-interacting ($U = 0$), intermediate ($U \sim 5\,J$) and hard-core ($U \sim 15\,J$) interactions. Data is averaged over 3 times and 4 phases. Vertical errorbars show the standard deviation of the mean, horizontal errorbars the standard deviation.

'W'-shape is clearly observable. Trivially, the doublon fraction is irrelevant in the non-interacting case. Also for intermediate interactions of $U < 8J$ the doublon fraction has a minor impact on the stationary imbalance. Only, when the hardcore regime is approached ($U > 8J$) significant differences appear. In the absence of doublons, we find that the imbalance in the hard-core regime has the same value as in the non-interacting case. This is due to a mathematical exact mapping of hardcore fermions to non-interacting particles [43]. However, this mapping is only valid in the absence of doublons. Hence, the non-interacting and attractively loaded curves significantly deviate and show larger imbalances with an increasing doublon fraction. This is, again, easily understandable via the picture of doublons forming quasi-particles with slower hopping rates, as discussed in the previous section. Note that the interplay of doublons and singlons has not been fully investigated and might happen on a timescale much larger than the $20\,\tau$ chosen for the stationary imbalance. As this interplay is likely complicated and adds an additional timescale, we use repulsive loading for all further experiments.

Effect of the temperature of the initial state: To investigate the effect of the temperature of the cloud on the stationary imbalance, we heat the atom cloud by manipulating the cooling sequence. The stationary imbalance is plotted in Fig. 5.6 as a function of the cloud's relative Fermi-temperature in the dipole trap, prior to loading into the lattice. As the initial temperature also influences the number of doublons that can be loaded (see Fig. 5.1), we distinguish between attractive loading and repulsive loading.

When loading attractively, the dominant mechanism of increased temperature is the decreasing doublon fraction. This becomes apparent from the stationary imbalance at

hard-core interactions, which decreases to the level of the non-interacting imbalance at higher temperatures. When doublons are not present due to initial repulsive loading, additional effects become visible. In this case, the hard-core and the non-interacting imbalances remain constant, but the imbalance at intermediate interactions increases with increasing temperature. This is likely due to the temperature increasing the initial cloud size, thereby decreasing the density. Hence, the effect of interactions is reduced and the imbalance increases.

Thus, we find that varying the temperature of the initial state is not a useful tool to investigate MBL, as higher temperatures simply reduce the effects of interactions due to a reduced density. The doublon fraction can be more accurately controlled via the interaction strength during the lattice loading sequence (compare Fig. 5.1a).

The many-body localization phase transition

In the previous chapter, we have established the existence of a many-body localized phase in our system via a finite-time analysis of the imbalance. However, this analysis is likely not sufficient to understand the regime close to the localization transition, where critically slow dynamics are expected [169]. In this chapter, we will present a more in-depth study of this interesting regime. We will begin with a short discussion of typical quantum phase transitions. On the example of the many-body localization transition in random systems, which was studied much more extensively than the quasi-periodic case, we will then explain in what sense the MBL (de)localization transition is atypical and introduce some concepts and arguments used to discuss its behavior. Apart from being interesting in its own right, we further motivate our study of the quasi-periodic transition by discussing how its understanding can give insights into the transition in randomly disordered systems. We then give a detailed experimental analysis of the transition in quasi-periodic systems via the dynamics of the imbalance and discuss the results in the context of recent numerical investigations.

6.1 Phase transitions

Phase transitions mark a sudden change of a systems' properties at a critical value of a control parameter. Transitions can be classified into first and second order transitions, depending on the first discontinuous derivative of a thermodynamic potential. A common example of a first order transition is the melting of ice into water, which involves latent heat and hence is of first order. At such first-order transitions, the two bordering phases coexist at the critical value of the control parameter, which in this example is the temperature. In contrast, in a second order, also called continuous, transition the two phases do not coexist. A popular example of such a continuous transition is the vanishing of the magnetic moment in iron above a critical temperature. We will focus on continuous phase transitions.

A continuous transition is characterized by an order parameter, which is an observable of the system that takes a finite value in one phase, and continuously vanishes when approaching the critical point. In the other phase, the order parameter is zero on average but shows fluctuations which drive the transition. The typical length scale associated with
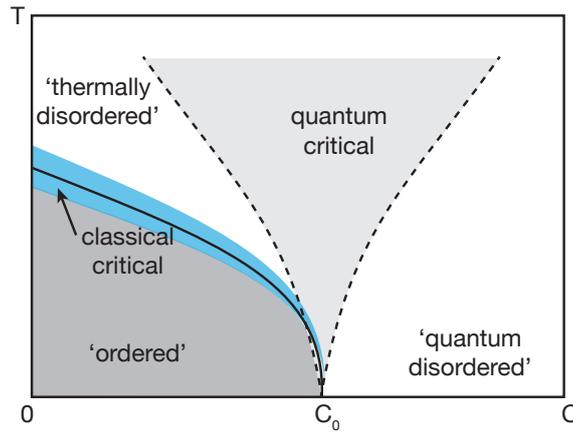
Figure 6.1: Schematic of a phase diagram close to a typical quantum critical point: Schematic of a phase diagram close to a typical quantum critical point with a control parameter C and temperature T. In this example, an ordered phase at low enough temperatures shows a classical transition to a disordered phase at high enough temperatures. Also, a disordered phase can be reached by tuning the control parameter at $T = 0$ through the quantum critical point at C_0 [73].

these fluctuations usually referred to as the correlation length ξ diverges when approaching the critical point as

$$\xi \sim |\delta|^{-\nu}, \tag{6.1}$$

where $\delta \sim (C - C_0)$ is the distance to the critical point C_0 for the control parameter C, and ν is the critical exponent. The fluctuations are further associated with a typical timescale τ that they decay in, which is given by

$$\tau \sim \xi^z, \tag{6.2}$$

where z is the dynamical critical exponent. The divergence of typical timescales close to the transition is known as 'critical slowing down'. Especially, critically slow timescales result in very long equilibration times when a system is driven over the phase transition.

Due to the divergence of ξ and τ at the critical point, fluctuations in the order parameter happen on all time- and length scales. Hence, the system becomes scale-invariant (i.e. rescaling all lengths does not change the physical properties) and the microscopic details of the Hamiltonian become unimportant. As a consequence, all observables simply depend on the external control parameters via power-laws, given by the critical exponents that characterize the transition.

In classical phase transitions, the fluctuations driving the transition are thermal, and the control parameter is often the temperature $C = T$. Quantum phase transitions are, in contrast, driven by quantum fluctuations coming from the uncertainty principle [73]. Which type of fluctuations are dominant for a transition at finite temperatures can be decided by comparing the typical energy scale of quantum fluctuations $\hbar\omega \sim 1/\tau$ to the thermal energy $k_B T$. As the energy scale of the quantum fluctuations goes to zero at the transition, it is easy to recognize that a purely quantum transition can only occur at $T = 0$

in the ground state. Hence, the temperature can also not serve as a control parameter, which instead has to be a parameter of the Hamiltonian. A typical phase diagram in which a control parameter in the Hamiltonian C, as well as the temperature T, can be varied is illustrated in Fig. 6.1. In this example, an ordered phase (i.e. a phase where the order parameter is finite) exists if the control parameter is $C < C_0$ and the temperatures are low enough. From this ordered phase, a classical phase transition, which is driven by thermal fluctuations, leads to a phase where the order is destroyed thermally. Upon approaching the transition at low temperatures, the classical critical regime becomes narrower, until at $T = 0$ the transition turns into a quantum phase transition. If the control parameter is larger than C_0, the system is in a quantum disordered phase. Above the critical point is a large quantum critical regime, which extends to finite temperatures, where the behavior of the system is set by both quantum and thermal fluctuations. The boundaries of this regime are accordingly given by $k_B T > \hbar\omega \sim |C - C_0|^{\nu z}$. More information on typical phase transitions can be found in e.g. Refs. [73, 181].

6.2 Previous results on the transition in randomly disordered systems

In recent years, the focus of research on the topic of MBL has shifted from the properties of the localized phase to the transition itself. Especially, the transition in random systems has received a lot of interest (see e.g. Refs. [36–38] for reviews), while the transition in quasi-periodic systems has been neglected until recently. However, even the transition in random systems is still poorly understood. Relatively certain is, though, that the MBL localization transition does not fit into the concepts of typical quantum phase transitions discussed above. Instead, it is a novel kind of eigenstate phase transition [28, 33], where eigenstates obeying the ETH change in a singular manner to being non-thermal at the transition. This is true for eigenstates over a large range of energy densities and hence the MBL transition is quantum not only in the ground state but also at elevated temperatures. The transition is, furthermore, a dynamical phase transition in the sense that it shows singularities only in dynamical quantities but lacks thermodynamic signatures. Gaining insights into the transition is difficult, as large-scale simulations via e.g. density-matrix renormalization group (DMRG) calculations are only reliable deep in the localized phase. Numerical simulations of the microscopic Hamiltonians are thus currently limited to exact diagonalization (ED) calculations, which severely restricts the accessible system sizes.

6.2.1 The renormalization group picture

An effective picture of the MBL transition in random systems was recently developed via coarse-grained renormalization group (RG) studies [39, 40, 182]. These studies have focused on the thermal side of the transition and managed to apply some concepts of typical phase transitions to the MBL transition. Especially, they have found the transition to be
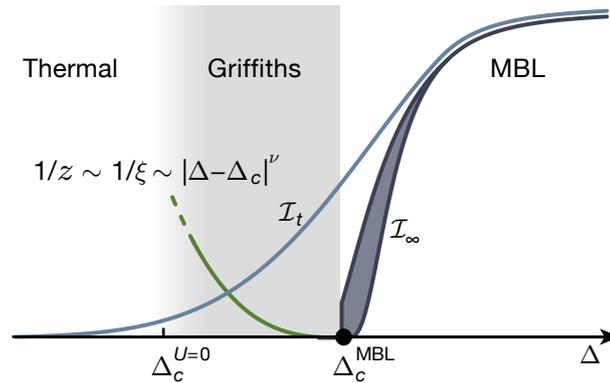
Figure 6.2: Schematic of the phase transition in random systems: In systems with random dis-
order, a Griffiths phase is expected on the thermal side of the transition, where rare-regions that are
locally in the localized phase dominate the dynamics. This is described via the dynamical exponent
z, which is proportional to the correlation length ξ. Hence, $1/z$ vanishes continuously at the transition
with a universal exponent that was found to be $\nu = 3$ by RG studies [39, 40]. The imbalance decays
as a power-law and is hence finite at finite times. At infinite times, the imbalance is only finite in the
localized phase. It is, however, not clear whether it rises continuously or jumps to a finite value at the
transition.

continuous with a critical exponent of $\nu \approx 3$. The developed effective picture is based on
rare 'Griffiths' regions [183]. These are (small) subsystems, which are locally 'in the other
phase', e.g. localized or critical in a globally thermal system. These subsystems emerge
due to the random nature of the disorder potential. In a random potential, naturally,
some regions appear with an untypically large disorder strength, thereby creating a local-
ized subsystem. The probability of such regions is suppressed exponentially in their size,
i.e. they appear with a probability density

$$p(L) \sim \frac{1}{\xi} e^{-L/\xi}. \tag{6.3}$$

This can be understood as $p(L)$ denoting the probability, that a given lattice site is part of
a localized subsystem of size L. Here, ξ denotes the typical size of a localized inclusion.
When the disorder strength is increased towards the critical disorder strength $\Delta \to \Delta_c^{MBL}$,
the probability of creating larger inclusions has to increase, which in this model happens
due to an increasing ξ. At the transition, when the entire system becomes localized, the
probability of a localized inclusion of infinite size consequently needs to be one, and hence
ξ has to diverge at the transition. Hence, ξ takes the role of the correlation length.

Below the transition, any localized inclusions will be thermalized by the globally ther-
mal system. The timescale of this thermalization process τ is exponentially long in the
size of the inclusion

$$\tau \sim e^{L/x_0}. \tag{6.4}$$

Here, the length is compared to a microscopic length scale x_0, which can be understood as
a localization length. Importantly, while x_0 does depend on the disorder strength, it does

not behave critically (i.e. diverges or vanishes) at the transition. Combining the exponential distributions of inclusion size and thermalization time results in a broad power-law distribution of relaxation timescales present in the system

$$p(\tau) \sim (1/\tau)^{1+1/z}, \tag{6.5}$$

where $z = \xi / x_0$. This distribution of timescales was argued to be visible in e.g. the imbalance. This becomes clear if one estimates the imbalance $\mathcal{I}$ at time t as the fraction of sites that belong to inclusions with relaxation times $\tau > t$:

$$\mathcal{I} \sim \int_t^\infty p(\tau) d\tau \sim t^{-1/z}. \tag{6.6}$$

The RG studies have found, that the correlation length ξ diverges with a universal exponent of $\nu \approx 3$ as

$$\xi \sim \left| \Delta - \Delta_c^{\mathrm{MBL}} \right|^{-\nu} \tag{6.7}$$

at the transition. Hence, $1/z \sim 1/\xi$ vanishes at the MBL transition. Following equation (6.6) one would thus expect power-law decays of the imbalance in the thermal phase, which gradually become slower when the transition is approached. The onset of the MBL phase would then be marked by the imbalance being stationary. The RG studies [39, 40] further showed that z denotes the dynamical exponent, which is associated with transport. As $1/z$ vanishes continuously at the transition, this suggests that on the thermal side of the transition a regime with sub-diffusive dynamics can be found.

A schematic illustration of the behavior of the dynamical exponent z and the imbalance $\mathcal{I}$ in the presented picture is given in Fig. 6.2. This schematic additionally illustrates the expected behavior of the imbalance. As the imbalance is expected to decay as a power-law, at finite times t it can be non-zero even in the thermal phase. This directly shows that the short time analysis presented in chapter 5 is potentially problematic close to the transition. Note that the illustration includes both the possibility of a continuous behavior of the infinite time imbalance, as well as the possibility of a discontinuous jump. While the RG simulations would predict a continuous behavior, the question of whether the transition is indeed continuous is not yet solved [48].

6.2.2 Numerical results

A major point of criticism of the RG simulations is that they do not start out from the microscopic Hamiltonian, but rely on a set of assumptions on the behavior of the system at larger scales. Due to the rapidly spreading entanglement in thermal systems, a direct simulation of the microscopic Hamiltonian is, however, only possible via exact diagonalization (ED). Such ED studies are in agreement with many of the predictions made by the RG-studies. Especially, a regime of sub-diffusive dynamics has been found in the thermal phase [169, 184, 185], and power-law relaxation processes of local quantities have been observed in numerical models [169, 184, 186–188]. Fig. 6.3 shows an example, where
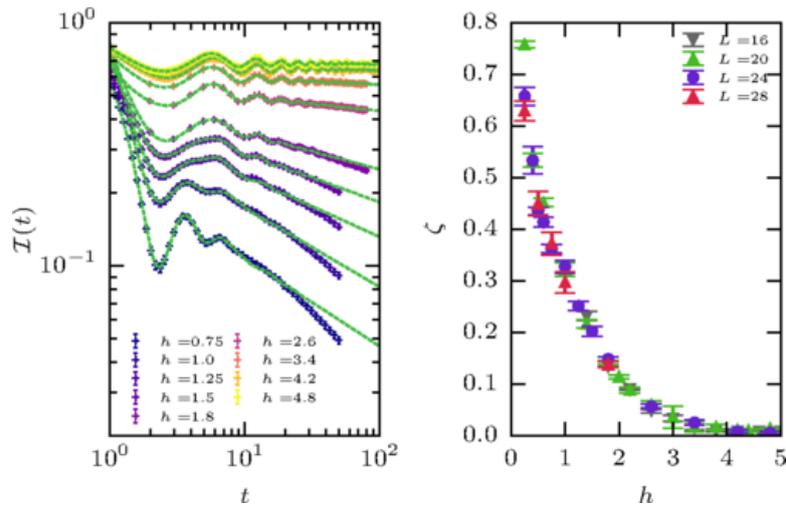
Figure 6.3: Imbalance dynamics in a system with random disorder: Decay of the spin imbalance in a randomly disordered spin system on a log-log plot. After a short initial decay, a longer timescale becomes visible, which can be fitted with a power-law. The power-law relaxation becomes stronger when the disorder strength h is increased. At around $h = 4$, the imbalance becomes steady, indicating that the system is localized. The exponents of the power-laws ζ are shown on the right and continuously go to zero. Figure reused from Ref. [169] with permission. Copyrighted by the American Physical Society.

the spin imbalance is calculated as a function of time [169]. The spin imbalance is closely related to the imbalance used in the experiment but is generalized to be usable in spin-systems with arbitrary initial states. Its time evolution reveals the same fast initial decay that is also observable in our experiments. This is followed by a much slower, further decay, which was argued to be best describable with power-laws. Upon increasing the disorder strength, the decay is becoming slower until the imbalance eventually becomes stationary, thereby indicating that the system is many-body localized. The extracted exponents, presumably corresponding to $1/z$, are found to vanish continuously when the transition is approached.

While the observations of the slow dynamics are in good agreement with the RG results, the determination of the universal exponent ν consistently gives different values of $\nu \approx 1$ in numerical (ED) simulations [166, 170, 189], as compared to $\nu \approx 3$ in RG. This numerical result violates the Harris-Chayes criterion [190–192], which states that the universal exponent in a disordered system has to be at least $\nu \geq 2$. This violation, and the difference to the RG result, likely emerge due to severe finite size limitations in ED. In fact, ED simulations are restricted to system sizes of about $L = 28$ sites in spin models and even smaller sizes of about $L = 20$ in Hubbard models, which likely restricts the access to the universal scaling regime.

A recent ED study [48] compared the universal scaling behavior in random systems to that in quasi-periodic systems. Through this comparison, the study found evidence that for the system sizes achievable in ED, the randomness in the disorder pattern does not yet

dominate the universal scaling behavior. This can e.g. be understood as the system being too small to form the increasingly large Griffiths regions when approaching the transition. In this case, the universal scaling would be similar to that of a system that cannot form rare inclusions due to a systematic detuning pattern, such as a quasi-periodic system. Hence, for the small system sizes considered in ED, the random system would not need to obey the Harris-Chayes criterion. In a following publication [41], this idea was further developed by the suggestion that two different universality classes exist: One class for large, randomly disordered systems that need to fulfill the Harris-Chayes bound, and another class for detuned, but not random (e.g. quasi-periodic) systems. In this picture, a small random system would be closer to the non-random universality class. Upon increasing its size, it would move towards the random universality class. However, it remains unclear how large of a system would need to be simulated in order to obtain a good estimate of the critical exponent in large, random systems. Definitely, such system sizes are not currently accessible for ED studies and will likely never be.

The analysis of Refs. [41, 48] suggests, that there are two major mechanisms at play at the many-body localization transition in random systems. The first mechanism is responsible for localizing particles at a given local disorder strength. This mechanism dominates the transition in small and/or quasi-periodic systems and seems to give a universal scaling exponent of $\nu \approx 1$. The second mechanism is that of Griffiths inclusions slowly being thermalized by the global system. This mechanism ultimately dominates the transition in large random systems and, according to RG, gives a universal exponent of $\nu \approx 3$. While the Griffiths mechanism is hard to study numerically, a deeper understanding of the local mechanism dominating the behavior of small systems can be achieved using current numerical techniques. The local mechanism is, however, more cleanly accessible in a non-random system, further motivating a more detailed study of the transition in quasi-periodic systems. Here, the many-body localization transition has barely been investigated to date, and hence even less is known than for the case of random disorder. It is clear though, that the effective RG picture developed for the random transition does not apply in the quasi-periodic case, as Griffiths regions in the disorder pattern are a-priori absent [193].

6.3   Slow dynamics close to the quasi-periodic transition

Experimentally, we attempt to collect additional information on the transition in our quasi-periodic system by analyzing the slow dynamics that are expected in its vicinity. Instead of extracting a steady state value of the imbalance reached after few tunneling times (as in chapter 5), we will look for additional, potentially much slower dynamics ensuing after the initial decay. For long times, we expect that couplings to external baths will dominate the behavior of the system (see chapter 7) and hence we will focus on an intermediate time range of up to $40\,\tau$.

Fig. 6.4 shows a measurement of such intermediate timescale dynamics for both an interacting system at an interaction strength of $U = 4J$, and a non-interacting system at
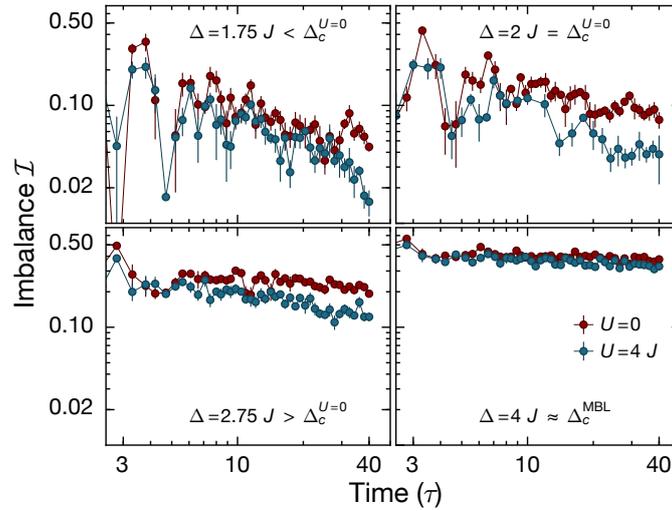
Figure 6.4: Interacting and non-interacting time traces close to the transition: Comparison of the interacting ($U = 4\,J$) and non-interacting ($U = 0$) dynamics for various detuning strengths close to the known transition point in the non-interacting system at $\Delta = 2\,J$. Points are averaged over 6 realizations of the detuning pattern ϕ, errorbars show the standard deviation of the mean. The quick initial decay of the imbalance during the first $3\,\tau$ is omitted and a double-log scale is chosen to clearly visualize the intermediate timescale dynamics.

$U = 0$. The graphs are plotted on a log-log scale, which is best suited for visualizing the dynamics. The fast initial decay of the imbalance from its starting value during the first $3\,\tau$ is omitted. We do not show a trace for a detuning strength of $\Delta = 0$, as here the imbalance already decays to below the noise limit within the first three tunneling times. Experimentally resolvable slow dynamics can only be observed for detuning strengths above $\Delta = 1.75 J$, which is just below the single-particle transition at $\Delta_c^{U=0} = 2 J$. Here, all single-particle states (and accordingly also all many-body states) are extended, and we find that the interacting and the non-interacting system behave similarly. The fast initial decay results in an imbalance of around $\mathcal{I} \approx 0.1$, and is followed by a slower, but still comparatively fast, further decay. This further decay likely continues until the imbalance has reached zero, indicating a delocalized system.

At the single-particle transition ($\Delta_c^{U=0} = 2 J$) we still observe decaying dynamics in the non-interacting system, although now slightly slower than before. This is the expected behavior of a system that displays critical slowing down. Note that at the transition point the imbalance is still expected to decay to zero. The interacting system shows a slightly faster decay than the non-interacting system, suggesting that interactions help to relax the imbalance.

Sufficiently far above the single-particle transition, the non-interacting imbalance becomes stationary, as one would expect in the localized phase. However, the interacting imbalance still shows ongoing decays. Postulating that the observed decay continues until the imbalance reaches zero, the interacting system will indeed still be thermal. Hence,
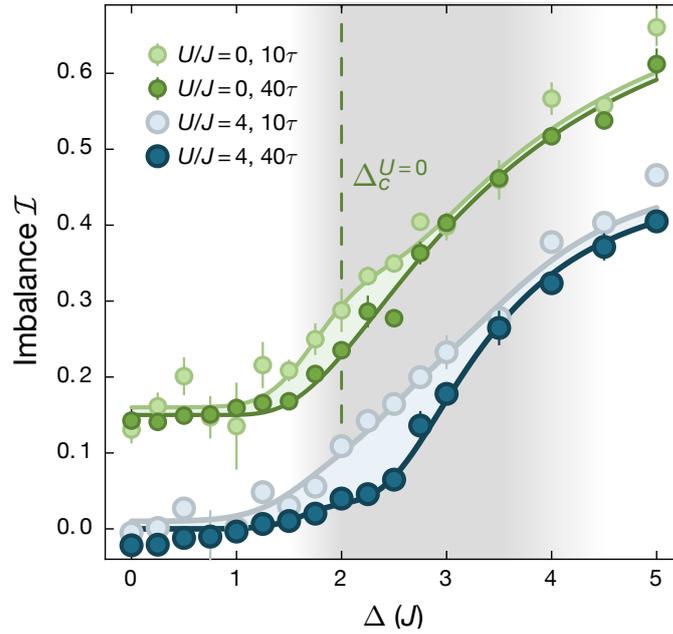
Figure 6.5: Finite-time imbalances: Comparison of the finite-time imbalances at evolution times of $10\,\tau$ and $40\,\tau$ for the interacting ($U = 4\,J$) and the non-interacting ($U = 0$) system as a function of the detuning strength Δ. Points are averaged over six realizations of the detuning pattern ϕ. Errorbars denote the standard deviation of the mean. The non-interacting data is vertically offset by 0.15 for clarity. The solid lines are guides-to-the -eye and the blue (green) shaded region indicates the detuning strengths at which slow, intermediate time-scale dynamics are present.

at these parameters, the interactions destabilize and thermalize the underlying single-particle localized system.

Only at much deeper detuning strengths do the decays of the interacting system also vanish, indicating that the interacting system is many-body localized. The interacting imbalance lies slightly below the non-interacting imbalance, which is likely due to a larger localization length in the many-body case, and consistent with the measured 'W'-shape of the stationary imbalance as a function of the interaction strength in section 5.3.2. Note though, that the lower imbalance in the interacting system could also be explained via other mechanisms, such as e.g. a faster background decay in the interacting system [69]. Also, logarithmically slow decays on intermediate timescales towards the true steady-state imbalance could be present in the many-body localized phase [194].

## 6.3.1 Validity of finite-time investigations

In order to show the presence/absence of slow dynamics on an intermediate timescale over a larger range of detuning strengths, we compare finite-time measurements of the imbalance after $10\,\tau$ (short) to those after $40\,\tau$ (long) in Fig. 6.5. The two times are chosen to be at the beginning and end of the dynamic range of the time traces shown

in Fig. 6.4. As expected from the observed dynamics, for both the interacting and the non-interacting system we find a regime where the imbalance after $40\,\tau$ is significantly below the imbalance after $10\,\tau$, indicating the presence of slow dynamics. Above and below this regime, we find that the short and long-term imbalances agree well, suggesting the absence of slow dynamics. There, the system is either fully delocalized or deep in the localized phase. Comparing these results to the analysis used in chapter 5, where the phase diagram was mapped out using a single finite time measurement of the imbalance after $\sim 20\,\tau$, suggests that the general picture of an extended and a localized phase shown in Fig. 5.4a is accurate. Only close to the transition the finite-time analysis does not capture the full picture, likely resulting in an inaccurate estimation of the critical detuning strength. A more accurate prediction needs to consider the slow dynamics.

The two finite-time measurements in Fig. 6.5 can already serve to give additional insights into the transition. Comparing the interacting and non-interacting regime of slow dynamics (i.e. disagreeing short and long-time imbalance), we find that both begin at approximately the same detuning strength of $\Delta \approx 1.5\,J$. However, the interacting regime of slow dynamics extends to much larger detuning strengths of approximately $\Delta \approx 3.5\,J$, as compared to the non-interacting regime which ends at $\Delta \approx 2.5\,J$, suggesting that the many-body critical detuning strength is indeed larger than that in the single-particle case. Also, the maximum observable difference of $\mathcal{I}_{10\,\tau} - \mathcal{I}_{40\,\tau}$ is much larger in the interacting system, suggesting that the dynamics are faster in the presence of interactions.

The slow dynamics regime in the non-interacting case is symmetric around the known transition point of $\Delta_c^{U=0} = 2J$. On the delocalized side of the transition, the dynamics are due to a slow spreading of individual particles until the imbalance is zero. This is in contrast to the localized side, where the dynamics are not expected to continue until the imbalance is zero. Instead, the dynamics should only be observable on intermediate timescales and end at a finite imbalance. The mechanism behind these dynamics is the slow spreading of particles until they reach their localization length. Just above the transition, the localization length is comparatively large and hence significant intermediate dynamics are observable. Upon increasing the detuning strength further, the localization length shrinks and once it is on the order of a single lattice site, no dynamics are observable anymore.

Based on the analysis of the transition in random systems shown in Fig. 6.3, a slightly different picture emerges for the interacting system. In the interacting system, we expect the thermal phase to be much more robust than the many-body localized phase, as even small thermal inclusions might be able to destabilize an otherwise localized system. In systems with random disorder, such regions emerge as thermal Griffiths inclusions due to the randomness in the disorder pattern. Hence, the transition is usually expected where no dynamics are observable on intermediate timescales anymore [169], as was discussed in Fig. 6.3. Such estimates of the transition point are in quantitative agreement with other methods, such as finite size scalings of the entanglement entropy, the level spacing statistics or the participation ratios [170]. Additionally, any relaxation dynamics towards a finite imbalance in the MBL phase were predicted to be logarithmically slow and hence
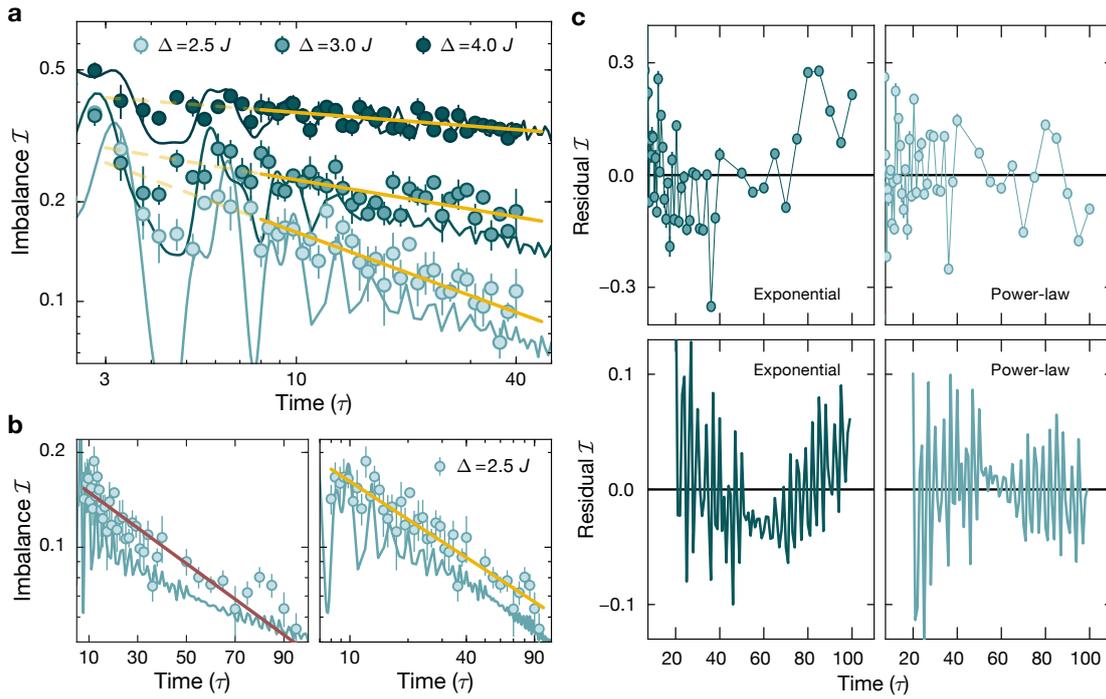
Figure 6.6: Many-body dynamics close to the transition: a) Interacting ($U = 4\,J$) time-traces of the imbalance close to the transition. Points are averaged over 6 realizations of the detuning pattern ϕ. Errorbars indicate the standard deviation of the mean. Solid lines are theoretical simulations of the experimental system performed on $L = 20$ sites. Yellow lines indicate power-law fits to the experimental data. Traces are plotted on a log-log scale and omit the initial decay of the imbalance from its starting value. b) Decay of the imbalance at $\Delta = 2.5\,J$, where we have the largest accessible dynamical range. The left panel shows the data on a logarithmic y-axis with an exponential fit (red line), the right panel on a double-log scale with a power-law fit (yellow line). c) Residuals of the exponential and power-law fits to the experimental (top) and numerical (bottom) data at $\Delta = 2.5\,J$. Numerical simulations were performed by Fabien Alet [108].

should not be visible on the accessed timescales [194]. Based on these arguments, we would expect the interacting transition to lie not in the center, but on the top end of the interacting regime of slow dynamics. To further investigate the transition in the interacting systems, we will present a detailed analysis of its dynamics in the following section.

6.4 Analysis of the slow dynamics in the interacting system

To further investigate the dynamics in the interacting system, we record time-traces for various detuning strengths above the single-particle transition, three examples of which are shown in Fig. 6.6a. The traces are again plotted on a double-log scale and the initial decay of the imbalance during the first three tunneling times is omitted. We find that the decays on intermediate timescales (as shown in Fig. 6.4) systematically become slower

when the detuning strength is increased. Our experimental observations are in very good agreement with theoretical calculations, which simulate our experimental setup on $L = 20$ sites. The calculations use an initial state where odd sites are empty and even sites are randomly populated by one atom of either spin, such that the total spin is zero. As the experiments are performed using repulsive loading, this is the exact description of the initial state, except for $\sim 10\%$ doublons and holes in the experimental initial state. Due to imperfections in the loading and detection sequence, the initial imbalance in the experiment is only about $\mathcal{I}_\text{init} \approx 0.9$. To match the theoretical simulations to the experiment, their results are rescaled by this factor.

Comparing the experimentally observed dynamics in our quasi-periodic system to those numerically observed in randomly disordered systems (Fig. 6.3), we find strong similarities. This is surprising, as the mechanism of Griffiths regions possibly responsible for the dynamics observed in random systems should not apply in our quasi-periodic setting. In the random system, the dynamics were found to be best described using a power-law fit [169]. Also, the experimental and numerical data for the quasi-periodic system seems to be describable by power-laws. In order to get further insights into the functional form, in Fig. 6.6b we show the imbalance time-trace at a detuning strength of $\Delta = 2.5 J$ on a logarithmic y-axis and on a double-log plot to slightly longer times of $100\,\tau$. At this detuning strength, the system displays one of the largest accessible dynamic ranges in both imbalance and time, as the detuning strength is low enough for a fast decay of the imbalance but large enough for the imbalance to stay above the noise floor even after $100\,\tau$. We compare an exponential description (red line) to a power-law description (yellow line). Both fits characterize the data well, but the power-law description appears to be slightly better suited. The experimental points scatter more evenly above and below the fitted line, and the theory line is straighter on the double-log plot. Fig. 6.6c shows the residuals of the fits to theory and experiment. The residuals also show a slight preference to the power-law description, as the residuals for the exponential fit show a stronger systematic trend. However, the accessible dynamic range in the experiment is not large enough to reach a definite conclusion on the functional shape. A similar analysis of the intermediate time dynamics has also been performed in Ref. [195], which comes to the same conclusion.

6.4.1 Characterization via power-laws

Based on the analysis presented above, we choose to characterize the dynamics via power-law fits

$$\mathcal{I}(t) \sim t^{-\alpha}, \tag{6.8}$$

for which we choose a time window of $8-40\,\tau$ for the experimental data. Fitting at shorter times would pick up the oscillations that are initially present in the imbalance. In the theoretical simulations, these oscillations are slightly longer lived. Hence, we perform
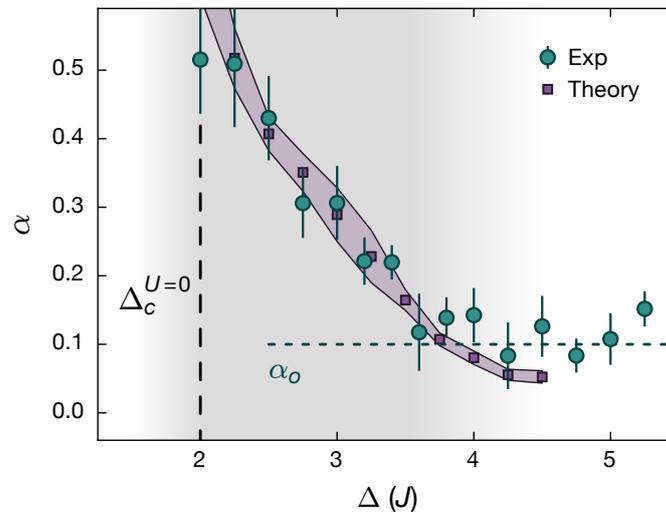
Figure 6.7: Power-law exponents of the interacting dynamics: Fitted exponents to the power-law behavior of the imbalance time traces on intermediate times. Points mark experimental data with the errorbars indicating the uncertainty of the fit. Upon increasing the detuning strength, the experimental exponents saturate at a finite value of α_o. The result of the fits to theoretical simulations are indicated as purple squares. The purple shaded region marks the uncertainty, which is estimated via the difference of the simulations with a size of $L = 20$ and $L = 16$. At large detuning strengths, the decays become too slow for an accurate fit and our method likely significantly underestimates the error. Numerical simulations were performed by Fabien Alet [108].

the fits at slightly longer times of $20 - 80\,\tau$. In order to emphasize all points equally, the fits are performed by fitting a linear relationship to the logarithm of the data, i.e.

$$\log(\mathcal{I}) = A - \alpha \log(t). \tag{6.9}$$

The fitted exponents are shown in Fig. 6.7. We find very good agreement between theory and experiment. The exponents decrease continuously when the detuning strength is increased and eventually settle to a finite offset value α_o. Even though we have restricted the accessed timescales to $40\,\tau$, this offset is likely due to the background decays that are present in the experimental system. A more detailed analysis of this can be found in section 6.4.3. The theoretical exponents also seem to saturate at a non-zero value, which is likely a finite-size effect. However, also potential intermediate decays happening in the localized phase [194] could contribute to these exponents.

In principle, the extracted exponents can be used to estimate the transition point as the detuning strength where the exponents become zero. However, due to the background decay induced offset in the exponents, this is not directly possible. Especially, estimations are difficult as the interplay between the external decays and the internal relaxation dynamics is completely unknown. Considering the exponents, two limiting scenarios are possible: In a first possible scenario, the effect of the background decays simply is to be added onto the closed system's exponents α_{closed}, i.e.

$$\alpha_{\text{closed}} = \alpha - \alpha_o. \tag{6.10}$$

In this scenario, the two processes would be fully independent of each other and the critical detuning strength could be estimated as the detuning strength where the exponents become compatible with the background. This value also serves as a lower bound for the transition of $\Delta_c^{\text{MBL}} > 3.5\,J$. However, the theoretical simulations already do indicate that the actual transition point is located at a slightly larger detuning strength. In the other limiting scenario, the background decays would simply mask the behavior of the exponents once the internal relaxation becomes too slow. In this case the closed system's exponents would be given by

$$\alpha_{\text{closed}} = \begin{cases} \alpha & \text{if } \alpha > \alpha_o \\ \text{unknown} & \text{else.} \end{cases} \tag{6.11}$$

Estimating the transition in this scenario is barely possible, as the transition point would depend largely on the functional form of the exponents. Assuming a universal scaling, this functional form would be given by the scaling exponent ν in

$$\alpha_{\text{closed}} = |\Delta - \Delta_c^{\text{MBL}}|^\nu. \tag{6.12}$$

As a best estimation in this case, we will use the theoretically suggested exponent of $\nu \approx 1$, as was discussed in section 6.2. This gives an estimation of the transition point of $\Delta_c^{\text{MBL}} \approx 4.5\,J$. This estimation is still in the limits of a previously found upper bound in
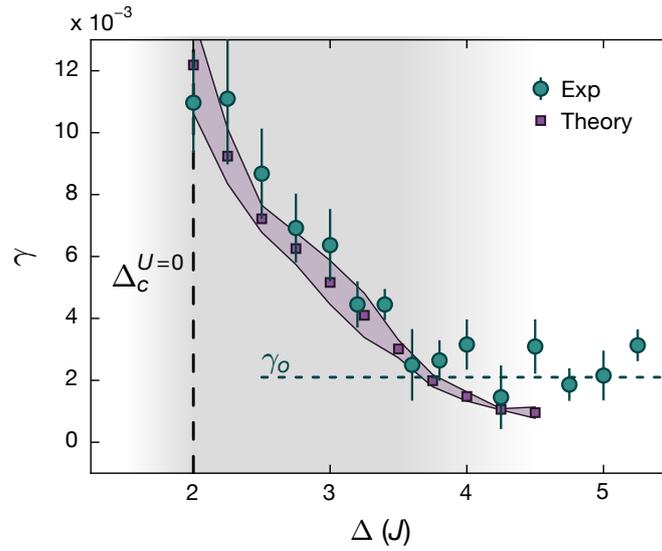
Figure 6.8: Exponential decay rate analysis: Analysis of the interacting dynamics via the decay rate γ of exponential fits, equivalent to Fig. 6.7. All observations, including the background decay and the estimations of the critical detuning strengths remain the same. Numerical simulations were performed by Fabien Alet.

Ref. [110]. There, DMRG simulations showed a steady imbalance up to very long times at $\Delta = 5J$.

We note, that the estimations of the critical disorder strength do not depend on the power-law fitting. The same values can also be obtained by fitting an exponential decay $\mathcal{I} \sim e^{-\gamma t}$ and evaluating its decay rate γ instead of the exponent α as is shown in Fig. 6.8. Equivalent to the power-law analysis, the fits of the exponentials were performed as linear fits of $\log(\mathcal{I})$ vs. t.

6.4.2 Interaction dependence of the transition point

So far, the dynamics have been investigated at an interaction strength of $U = 4J$. Estimating the transition point as a function of the interaction strength U would, in principle, require a full measurement of the relaxation exponents α versus the detuning strength Δ at various interaction strengths. However, an indication of how the transition behaves with different interaction strengths can be gained by simply scanning the interaction strength at a single detuning strength. Fig. 6.9 shows the interaction dependence of the power-law exponents at a detuning strength of $\Delta = 2.5J$. The exponents clearly reveal that the highest critical detuning strength is expected at intermediate interaction strengths of about $U \sim 5J$. In the hard-core limit, the exponents are similar to those in the absence of interactions, which is expected due to an exact mapping from hardcore to non-interacting Fermions in the absence of doublons [43]. The shape of the curve is consistent with
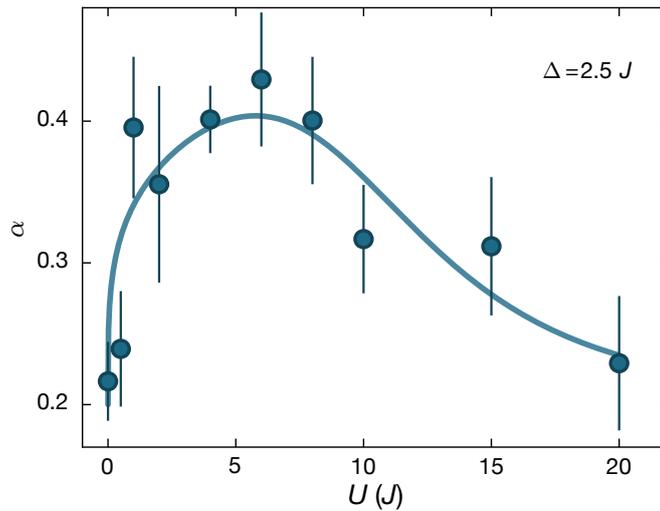
Figure 6.9: Interaction dependence of the power-law exponent: Experimentally extracted power-law exponent α as a function of the interaction strength U at a detuning strength of $\Delta = 2.5\,J$. Errorbars denote uncertainty of the fit. The solid line is a guide-to-the-eye.

the earlier found 'W'-shape of the finite time imbalances as a function of the interaction strength (see section 5.3.2).

6.4.3   Effects of external couplings

In the analysis of the slow dynamics (section 6.3), the longest accessed time was limited to $40\,\tau$, as on longer times the dynamics are increasingly strongly affected by background decays. Still, the exponents in Fig. 6.7 settle to a finite value $\alpha_o \approx 0.1$, indicating that the decay of the imbalance does not completely stop in the localized phase. While some decays on intermediate timescales could be present also in the localized phase [194], the dominant contribution to these decays is likely the background decays, as our experimental MBL system couples to external baths. In the localized phase, the effects of such external decays are usually well described by stretched exponential decays (see e.g. [69, 70, 196])

$$\mathcal{I}(t) \sim e^{-(t/\tau_{bg})^\beta} \tag{6.13}$$

with a background decay time τ_{bg} and a stretching exponent β. Experimentally, an often found value for the stretching exponent is $\beta \approx 0.6$ [69, 70], and hence this value is chosen for the following analysis. Fig. 6.10a shows stretched exponential decays corresponding to various background decay times. In order to assess the effects of a stretched exponential decay on the power-law exponents, the decay curves are evaluated at 10 different times in the experimental measurement interval of $8-40\,\tau$. The points are equally spaced on a logarithmic timescale. Then, a power-law is fitted to those points by fitting a linear behavior of the form

$$\log(\mathcal{I}) = A - \alpha_o \log(t), \tag{6.14}$$
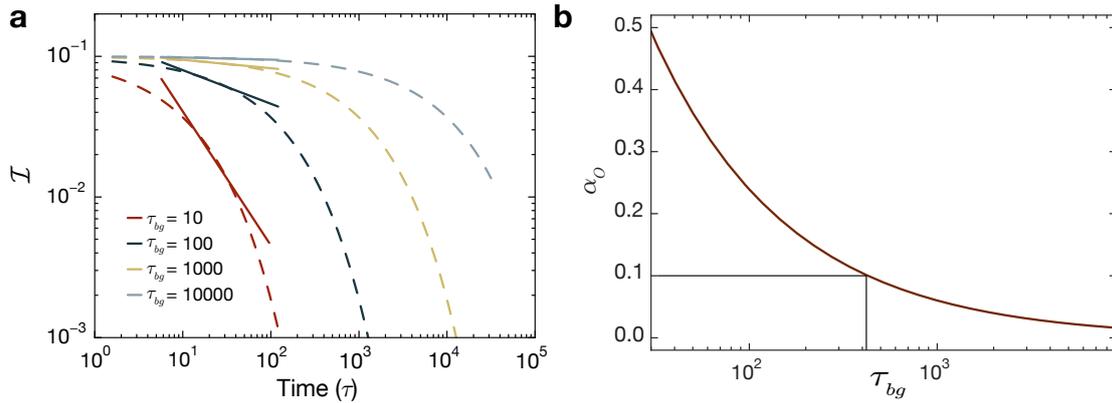
Figure 6.10: Exponent offset derived from background decays: a) The expected offset to the power-law exponents α_o is calculated by fitting a power-law (solid lines) to stretched exponential decays (dashed lines) in the experimentally relevant timescale of $8 - 40\,\tau$ for different imbalance lifetimes τ_{bg}. For the stretched exponential decay, a stretching exponent of $\beta = 0.6$, which was often found experimentally [69, 70], was chosen. b) The epected exponent offset as a function of the imbalance lifetime τ_{bg}. The experimentally found background of $\alpha_o \approx 0.1$ is indicated by solid black lines and yields an imbalance lifetime of several hundred tunneling times.

where α_o directly gives the power-law exponent that is expected due to the stretched exponential background decay. The fitted power-laws are indicated as solid lines. Since the plot is on a double-logarithmic axis, they appear as straight lines. It is clearly visible, that for background decay times of $\tau_{bg} \gtrsim 100\,\tau$ the stretched exponentials are well approximated by power-laws in the relevant time frame. Hence, on the accessed timescales, the experimentally measured time-traces would continue to appear linear on a double-log plot even if the behavior was dominated by a stretched exponential decay.

The extracted exponent offsets α_o are shown in Fig. 6.10b as a function of the background decay time. As is illustrated by the black lines, the experimentally found value of $\alpha_o \approx 0.1$ would correspond to a background decay time of $\sim 400\,\tau$, which is approximately the lifetime of the imbalance we expect at such low detuning strengths in the presence of interactions (see chapter 7).

6.5   Interpretation

We have experimentally and numerically found that the dynamics in the quasi-periodic system are fairly similar to those numerically observed in randomly disordered systems [169] (see Fig. 6.3). This is unexpected, as from the RG-picture (see section 6.2) the power-law decays in the random system were expected due to Griffiths inclusions which are absent in the quasi-periodic system. The similarity of the observed dynamics does, however, suggest a common underlying mechanics. Such an idea is further supported by the results of Ref. [41], which suggest that the apparent similarity in ED simulations

between random and quasi-periodic systems might be due to ED failing to capture the effects of Griffiths regions due to severe finite size restrictions. These results suggest that the dynamics in random systems (shown in Fig. 6.3) is at least not entirely due to the relaxation of Griffiths inclusions.

An alternative idea on the origin of the dynamics was suggested together with the first observation of the slow dynamics in randomly disordered systems [169]. The authors noted, that the slow dynamics span a much larger regime of disorder strengths than would be expected from the Griffiths picture, and speculated that this might be due to randomness in the initial state. This randomness could give rise to additional rare-region effects, as subsystems with a lower (higher) local energy density might localize at different disorder strengths. Such effects would indeed also be present in our quasi-periodic experimental setup, due to the initially randomly distributed spins. In our case, subsystems might localize at different detuning strengths depending on the magnetization

$$M_{sub} = 2S_{sub}/N_{sub} \tag{6.15}$$

of the subsystem, where S_{sub} and N_{sub} denote the total Spin and particle number in the subsystem. For example, a subsystem with a magnetization of $M_{sub} = +1$ or $M_{sub} = -1$ would only have one spin species in it. Hence, it would locally appear non-interacting and serve as a localized enclosure above the single-particle localization transition. While such rare-region effects in the initial state could explain the observed dynamics on intermediate timescales, they are fundamentally different from Griffiths regions emerging from the disorder pattern: As the particles are mobile and the regions will rearrange and thermalize over time, rare-regions in the initial state will not result in power-law dynamics on long timescales. Instead, the dynamics should become faster than power-law. In the experimental system, there is an additional effect that limits the impact of such regions to intermediate timescales, which is the delocalized spin sector [177]. As exchange processes between neighboring spins are resonant, spins can diffuse even through regions where the particles are localized and hence change the magnetization of subsystems.

In recent numerical studies, slow power-law dynamics on intermediate timescales have also been found in quasi-periodic systems without randomness in the initial state [195, 197]. This further suggests that the mechanism of rare-regions in the initial state is at least not the sole cause of the observed dynamics. An alternative explanation presented in Ref. [197] is based on anomalous transition rates between single-particle eigenstates, the combination of which also gives rise to a power-law behavior. However, the microscopic origin of such atypical transition rates is not clear. A similar mechanism had already been used to explain the results of an earlier experiment, which observed sub-diffusive spreading of bosonic atoms in a quasi-periodic geometry [136]. These experiments were performed at a detuning strength where our system would already be deep in the localized phase. However, in this experiment, no lattices were employed along the orthogonal directions. Hence, atoms were free to move and interact in two-dimensional discs, which were able to serve as a bath, likely causing the observed dynamics.
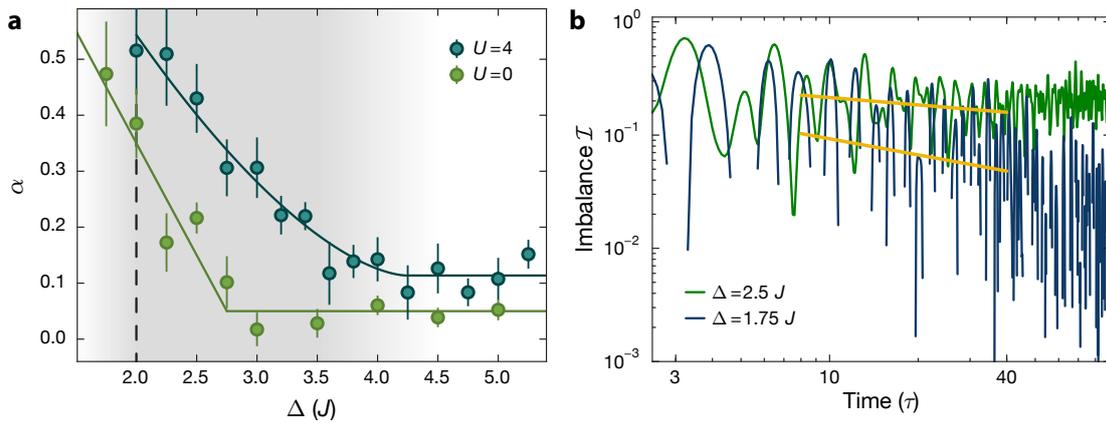
Figure 6.11: Non-interacting power-law exponents: a) Comparison of the non-interacting ($U = 0$) versus the interacting ($U = 4\,J$) power-law exponents. Errorbars denote the uncertainty of the fit. Solid lines are guides-to-the-eye. b) Non-interacting simulations of the time traces at two different detuning strengths. Yellow lines correspond to the power-law fits that were done on experimental data. Numerical simulations were performed by Fabien Alet.

Recently, it was also suggested that the observed regime of slow dynamics might only be a finite size effect [198] and that in the thermodynamic limit the dynamics in quasi-periodic systems would discontinuously jump from diffusive relaxation to localization. In randomly disordered systems, the continuously slowing dynamics were argued to persist.

In conclusion, an effective picture of the transition in quasi-periodic systems, which might also dominate the numerically observed dynamics in randomly disordered systems, is still missing. Hence, also the origin of the observed dynamics is at present unclear. This also raises the question whether the observed dynamics will continue at longer times and if (and how) they relate to universal properties of the transition. Potentially, a renormalization group study of quasi-periodic systems could give further insight. Additionally, a recently proposed approximate method for simulating thermalizing dynamics in quantum systems up to very long times and large system sizes [199] gives hopes to be usable also in the presence of (quasi-periodic) disorder, potentially enabling simulations of much larger system sizes.

6.6 Additional discussions and information

6.6.1 Non-interacting power-law exponents

In Fig. 6.11 the power-law exponents of the interacting system (as in Fig. 6.7) are compared to those obtained by fitting power-laws to the non-interacting dynamics. A significant difference is observable in the exponents. Clearly, the analysis performed to find the interacting critical point would vastly overestimate the known non-interacting transition at $\Delta_c^{U=0} = 2J$. This is due to intermediate dynamics of single particles relaxing until
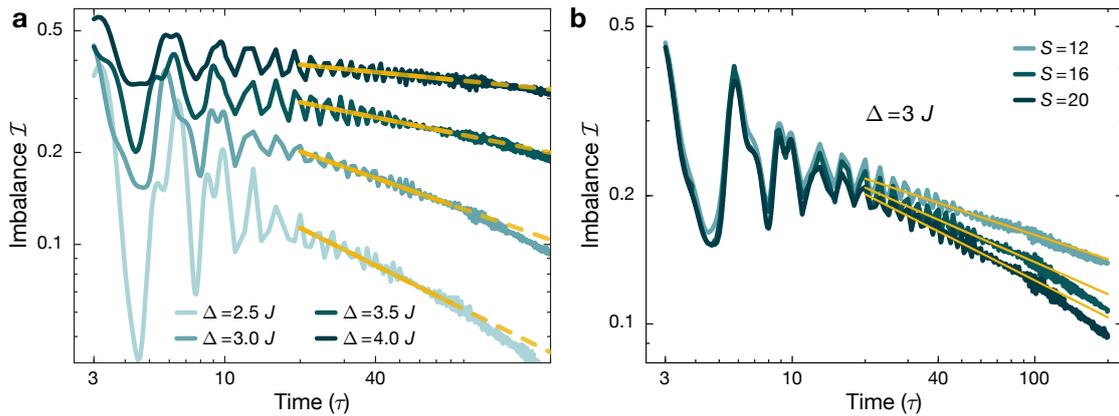
Figure 6.12: Interacting time traces calculated from exact diagonalization simulations: a) Simulations of the experimental system on $S = 20$ sites at an interaction strength of $U = 4\,J$ for different detuning strengths. Thickness of the lines denotes the statistical uncertainty of the numerical results. Yellow lines illustrate power-law fits between $20 - 80\,\tau$ used for the theoretical values of the exponents in Fig. 6.12. b) Finite size scaling of the theoretical simulations with power-law fits at a detuning strength of $\Delta = 3\,J$ and an interaction strength of $U = 4\,J$.

they reach their localization length also in the single-particle localized phase. At longer times, the imbalance would become stable at a finite value. The finite exponents in the single-particle localized phase can thus be considered a finite-time effect. In the interacting system, such dynamics on the localized side are expected to be much weaker (possibly logarithmic [194]) and hence likely do not play a role.

Comparing the non-interacting exponents to theoretical simulations is surprisingly more difficult than in the interacting case, as the non-interacting system exhibits strong oscillations on the investigated timescales, which make accurate fits impossible. Exemplary time traces are shown in Fig. 6.11b. In the experiment, such oscillations dephase much quicker due to the influence of trapping potentials and the averaging over neighboring systems with slightly different tunneling strengths J. However, an approximate comparison of theory and experiment is still performed in the figure, which shows the result of the power-law fit to the experimental data on top of the calculated time traces. It is clearly visible, that the approximate slopes fit well. Note, however, that the power-law behavior will not continue on longer timescales, at least in the non-interacting case. Hence, these power-laws are only observable due to the small dynamic range.

6.6.2   Details of the theoretical simulations

The theoretical simulations of the experimental system are carried out on $S = 20$ sites. The total atom number is 10 due to the charge-density wave initial state. The 5 atoms of each spin species are randomly distributed over Wannier states on the even lattice sites, the formation of doubly occupied sites is not allowed. All results are averaged over a minimum of 80 combinations of different initial states and detuning realizations ϕ. Note

that $S = 20$ is the maximum system size that is numerically accessible in Hubbard models today. Fig. 6.11a shows exemplary time traces of the imbalance $\mathcal{I}$ for different detuning strengths, as well as the power-law fits used to extract the exponents plotted in Fig. 6.12. In the theoretical simulations, the fits are performed in between $20 - 80\,\tau$, as on earlier timescales the system still displays oscillations which make the fit inaccurate. We find that the fit describes the time traces well, especially at large detuning strengths. At lower detuning strengths, however, one can see that the decays become faster than power-law at longer times. This is likely not a finite-size effect, as is shown in Fig. 6.12b, as the faster decays at longer times become more prominent at larger system sizes. Further, the performed finite-size scaling shows that the theoretical simulations are not yet converged at $S = 20$. The difference between the system sizes does, however, decrease. The error of the fitted exponent in Fig. 6.7 is calculated as the difference between the fits at $S = 16$ and $S = 20$. At larger detuning strengths, this error becomes very small. However, at these detuning strengths, we cannot access large enough times and system sizes to correctly estimate the exponent, and hence the uncertainty should be on the order of the exponent itself. The faster than power-law dynamics found in the theoretical simulations strongly suggest that the power-laws do not continue to infinite times. In the picture of rare-regions in the initial state, this could be due to rearrangements of the atom cloud, or due to diffusion in the mobile spin-sector [177]. However, the mechanism causing the faster dynamics at later times is still to be explored.

Signatures of many-body localization in open systems

Many-body localization is an effect that is usually studied and discussed in the context of a system that is fully isolated from its environment. In such fully isolated systems, the MBL phase is separated via a sharp transition from the thermalizing phase and the dynamics of the system are fully coherent. However, this setting is merely relevant in the context of describing the behavior of disordered/detuned quantum systems occurring in nature, or the behavior of experiments on MBL. This is because any real system will couple to its surroundings to at least some extent. As these surroundings can be considered to act as a bath, they give rise to external effects that will dephase the system with a rate γ with which the system couples to its environment. The interplay of many-body localized systems with various kinds of external baths has indeed been the focus of many studies [69–72, 75, 196, 200–208]. Generally, it was found that any coupling of a bath to a many-body localized system will eventually result in the full thermalization of the combined system, thereby destroying the localization in the MBL system. As experiments will never be fully isolated from their environments, true localization on very long timescales cannot be achieved. This was already visible in previous chapters, where external baths resulted in a decay of the imbalance at long times, visible in e.g. Fig. 5.3, as well as the offset in the decay exponents in Fig. 6.7. Especially the offset of the decay exponents limited the experiment's accuracy in determining the MBL critical point. Hence, understanding the external baths that couple to the presented setup, and studying their effects, is vital to understand the experimental results and potentially enable an extrapolation to the behavior of completely closed MBL systems.

An a-priori unexpected, but dominant decay mechanism resulting from the coupling of neighboring identical systems in our experimental setup (see section 7.1) has already been identified and thoroughly studied [69, 115]. However, further external processes corresponding to the traditional heating sources in cold-gases systems are expected to serve as external baths as well, such as frequency and amplitude noise on the lattice and dipole potentials [209, 210], collisions with the hot background gas in the vacuum chamber and the scattering of off-resonant photons from the optical potentials [211, 212]. While recent experiments on periodically driven MBL systems [110] suggest that slight
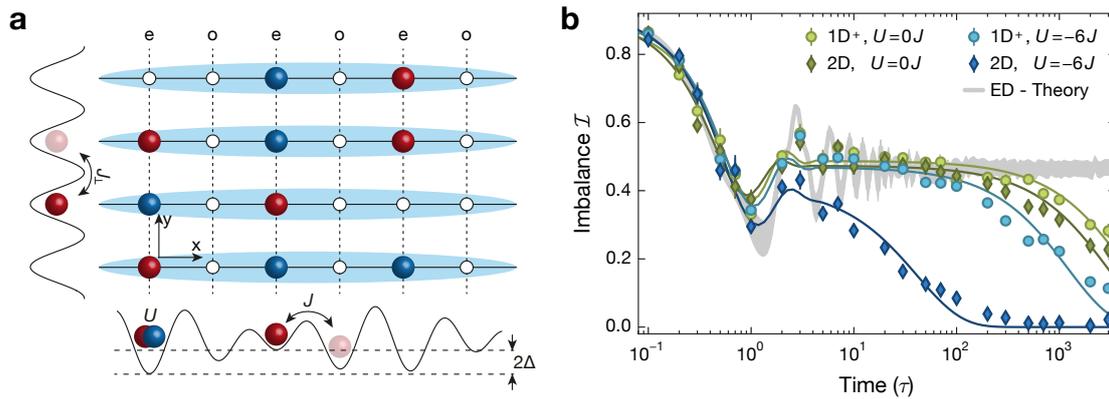
Figure 7.1: Effects of coupling identical tubes: a) Schematic illustration of coupling between identical tubes. In the experimental setup, neighboring tubes have the same quasi-periodic pattern, and hence tunneling along the orthogonal directions is resonant. Typically, the tunneling within the tubes J is much stronger than the tunneling between the tubes $J_\perp$. b) Long-term time traces of the imbalance for different interaction strengths in the $1D^+$ (2D) case with $J_\perp \approx 10^{-3}\,J$ ($J_\perp = J$). At long times the traces show decays that are not present in a closed system, as is illustrated by the ED-calculation for the non-interacting system. Points are averaged over six realizations of the quasi-periodic pattern ϕ. Errorbars denote the standard error of the mean. Lines are fitting functions with stretched exponential tails to extract the imbalance lifetime.

amplitude modulations of the optical potentials only contribute small heating rates, and typical timescales of background gas collisions exceed the decay timescales present in our MBL system by far, the scattering of photons could indeed contribute another major decay channel. To systematically study the effects of external baths in general, and specifically the effects of a photon bath, we implement a new technique of scattering near-resonant photons from a dedicated scattering beam which is shone onto the MBL system during the evolution time. These close-to-resonant photons effectively implement the effects of 'dephasing' studied in Refs. [196, 204, 206–208].

Before presenting the experimental results on the effects of photon scattering, we will briefly discuss a previous result on external baths obtained on our experimental setup. We will also give a detailed description of the experimental implementation of the photon bath. Note that this photon bath can be used to implement controlled external couplings also beyond the context of MBL. Detailed reviews of both previous theoretical and experimental investigations on dissipative quantum systems can be found in Refs. [107, 213].

7.1　Openness due to coupling between identical systems

In this section, we will briefly comment on a previous result on external decays obtained on our setup [69, 115]. In this previous experiment, the dominant decay mechanism present in our experiments was investigated and found to be the result of a reminiscent coupling

of (identical) one-dimensional tubes along the orthogonal directions (see Fig. 7.1a). This mechanism is always present and hence poses challenges to the study of other decay mechanisms as disentangling the respective contributions is potentially difficult.

The fundamental idea behind the 'coupling' mechanism is illustrated in Fig. 7.1a. In the experimental setup, the one-dimensional characteristics of the tubes, in which the experiments are performed, is created by deep lattices along the orthogonal directions. This strongly suppresses the tunneling between neighboring tubes to $J_\perp \approx 10^{-3} J$, where J denotes the tunneling rate within the tubes. Hence, the system behaves one-dimensional on short timescales, but on long timescales particles can also tunnel along the orthogonal directions. Since the quasi-periodic pattern is identical between the tubes, the tunneling along the orthogonal directions is resonant and can serve as a bath to thermalize the MBL systems realized in the tubes.

The effects of external decays are most directly accessible via a measurement of the lifetime of the steady-state imbalance in the MBL phase. Time traces for the cases of $J_\perp \approx 10^{-3} J$ (called 1D$^+$) and $J_\perp = J$ (called 2D) are shown in Fig. 7.1b. We find that in the absence of interactions the 1D$^+$ and the 2D case have similar lifetimes. This is easily explained by the separability of the overall Hamiltonian along the spatial directions, which is only broken in the presence of interactions. Hence, in the absence of interactions, the coupling mechanism is ineffective and the imbalance lifetime is limited by other mechanisms, the most likely candidate being the scattering of photons from the dipole and lattice beams. In the presence of interactions, however, we find significantly shorter lifetimes of the imbalance in the 2D case of strong coupling as compared to the 1D$^+$ case. This is due to interactions breaking the separability of the system, thereby allowing for a thermalization of the MBL systems via the resonant tunneling along the orthogonal directions. The shown time traces illustrate the limits of the experimentally accessible parameter regime and directly show how potent the coupling mechanism is in thermalizing the MBL systems. Additionally, also the 1D$^+$ case shows a shorter lifetime than in the absence of interactions. While this could simply be due to interactions enhancing the effects of the decay mechanism limiting the non-interacting lifetimes, we can show that it is indeed dominantly due to the coupling mechanism: This becomes visible via the lifetimes of the imbalance, which show a continuous increase when approaching the 1D$^+$ case in an interacting system [69]. This suggests that an even lower tunneling along the orthogonal direction would give even longer lifetimes of the imbalance and therefore the coupling mechanism limits the achievable interacting lifetimes even in the 1D$^+$ case.

In the context of investigating the effect of photon scattering on the MBL system, the observed coupling-induced decays are problematic. The most intuitive way of characterizing the effect of photon scattering would be to vary e.g. the orthogonal lattice depths, thereby controlling the scattering rate. In a naive picture, lower lattice depths would result in less scattering and should give longer lifetimes. However, this behavior is completely dominated and reversed by the coupling-effects. Hence, investigating the effects of photon scattering by directly using the lattice beams in not possible.

7.2   Theoretical description of open systems

In theoretical analysis, a Hamiltonian description of a (small) system coupled to a bath cannot usually be captured using Hamiltonian dynamics. It is easy to write down a generic Hamiltonian

$$\hat{H} = \hat{H}_S + \hat{H}_B + \hat{H}_\gamma, \tag{7.1}$$

with the system's and the bath's Hamiltonians $\hat{H}_S$ and $\hat{H}_B$, as well as the coupling term $\hat{H}_\gamma$. In this setting, the full system would be described by the density matrix $\hat{\rho}_{SB}$. However, typical external baths are too complicated to allow for a full quantum description and hence usually only the system is treated by considering the reduced density matrix $\hat{\rho}_S = \mathrm{Tr}_B(\hat{\rho}_{SB})$. Note that while $\hat{\rho}_{SB}$ is pure and its dynamics is unitary, the density matrix of the small system $\hat{\rho}_S$ will typically be in a mixed state. Also, its dynamics will usually be non-unitary, as the coupling to the bath introduces decoherence. The incoherent dynamics of the system can be described by the Lindblad master equation [214]

$$\dot{\hat{\rho}}_S = -i\left[\hat{H}_S, \hat{\rho}_S\right] + \gamma \sum_i \left(\hat{L}_i \hat{\rho}_S \hat{L}_i^\dagger - \frac{1}{2}\left\{\hat{L}_i^\dagger \hat{L}_i, \hat{\rho}_S\right\}\right). \tag{7.2}$$

Here, the first term describes the unitary evolution of the closed system. The second term captures the effects of the bath, where γ denotes the coupling strength and the $\hat{L}_i$ are the jump-operators that describe the action of the bath on the system. In the context considered here, the $\hat{L}_i$ are operators of the system. In a quantum trajectory picture, the effect of the bath can be thought of as a continuous measurement of the operators $\hat{L}_i$ [215, 216].

In the context of MBL, dissipation is usually studied on the example of the particle number operators for site i: $\hat{L}_i = \hat{n}_i$ (see e.g. [196, 204, 206–208]). This corresponds to a continuous measurement of the particle number on each lattice site. Effectively, this transfers states consisting of coherent superpositions of Wannier states into incoherent mixtures of the same Wannier states with the same probabilities, and is hence often referred to as 'dephasing'. Another interesting, but much harder operator to study theoretically is the annihilation operator $\hat{L}_i = \hat{a}_i$, which describes particle loss from the system (see e.g. Refs. [196, 217]).

Experimentally, the scattering of photons directly implements the jump operators $\hat{L}_i = \hat{n}_i$ and $\hat{L}_i = \hat{a}_i$, as has been shown for both bosons [211] and fermions [218]. Intuitively, this can be understood as the scattered photon providing information to the environment about the location of the atom, effectively resulting in a measurement of the position of the atom (see Fig. 7.2). This will project the atom initially in a quantum state $|\Psi_{\mathrm{init}}(x)\rangle$ onto a new wavefunction $|\Psi_{\mathrm{fin}}(x - x_0)\rangle$, which is localized around a location x_0 on the length scale $\lambda_{ph}/2\pi$, where λ_{ph} denotes the scattered photons wavelength. In this simplified picture, the probability for the location x_0 can be estimated via the overlap of the wavefunctions before and after scattering the photon.

$$P(x_0) = |\langle \Psi_{\mathrm{init}}(x)|\Psi_{\mathrm{fin}}(x - x_0)\rangle|^2. \tag{7.3}$$
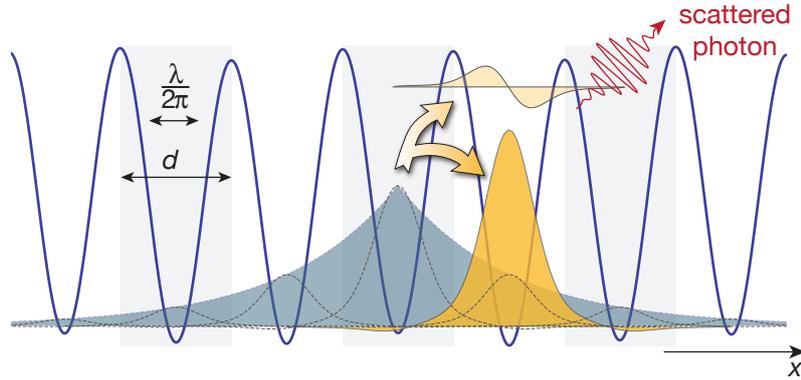
Figure 7.2: Schematics of scattering a photon: An atom in an initially coherent superposition (blue) of several Wannier states (dashed black lines) scatters a photon. As a result, the atom will localize on a length scale of $\lambda_{ph}/2\pi$, where λ_{ph} is the wavelength of the scattered photon. If this length scale is smaller than the lattice spacing d, the atom will become localized onto a single lattice site. Since the Wannier state of the ground band is the most localized state that can be constructed without any admixture of higher bands, localization on length scales smaller than d will necessarily result in the excitation of higher bands.

In an optical lattice, this will result in the localization of an atom onto a single lattice site if the lattice spacing d is smaller than the length scale the atom gets localized to $\lambda_{ph}/2\pi < d$ (see Fig. 7.2). Hence, the scattering process can be described as a measurement of the particle-number operator $\hat{n}_i^b$, where the index i labels the lattice site and b the band index. Most theoretical descriptions neglect higher bands and consider only the ground band, resulting in the 'dephasing' mechanism. Especially if $\lambda/2\pi \ll d$, however, higher bands will be excited, as a wavefunction that is localized on a length scale smaller than the ground band Wannier function can only be composed using admixtures from higher bands. Atoms that do get excited to higher bands will usually be delocalized due to much faster tunnel couplings. These faster tunneling rates allow the atoms to quickly tunnel out of the system. In this case, excitations to higher bands can be treated as particle loss, described by the annihilation operator.

7.3 Experimental implementation of controlled dissipation

In this section, we will describe in detail the experimental approach to implement a controlled external bath via photon scattering. We note, that this approach is not only relevant in the context of MBL, but can directly be used to study the effects of dissipation in other phases of matter as well.

We implement dissipation by scattering near-resonant photons on the D_2-line of ^{40}K. The level structure and the relevant excitation and decay processes are illustrated in Fig. 7.3. The experiments are performed at magnetic field strengths close to the Feshbach resonance of the two spin components $|\downarrow\rangle \equiv |F = 9/2, m_F = -9/2\rangle$ and
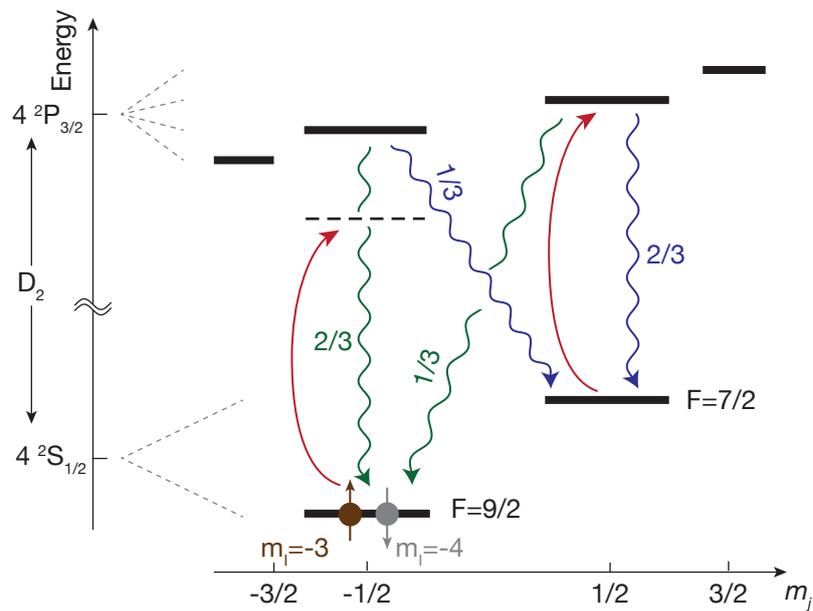
Figure 7.3: Level scheme of ^{40}K: Schematics of the atomic hyperfine structure and the transitions that are relevant for the scattering of near-resonant photons on the D_2-line. States are labeled via the quantum numbers m_J and m_I, which are good quantum numbers in the Paschen-Back regime. The external photons are marked as red arrows, spontaneous decay channels are indicated as wavy lines, together with the respective branching ratios.

$|\!\uparrow\rangle \equiv |F = 9/2, m_F = -7/2\rangle$ at about $210\,\mathrm{G}$ [100]. At this magnetic field strength, the excited state manifold $4\ ^2\mathrm{P}_{3/2}$ is already deep in the Paschen-Back regime, where the components of the total angular momentum $F = J + I$ decouple, and hence the projections of the electronic angular momentum J and the nuclear spin I, m_J and m_I, become good quantum numbers. The ground state manifold is not completely in the Paschen-Back regime, but using the quantum numbers m_J and m_I is already a sufficiently good approximation. Corrections due to this approximation will be discussed in section 7.3.2. In the Paschen-Back approximation, we can think of the spins of the particles $|\!\uparrow\rangle$, $|\!\downarrow\rangle$ to be characterized solely by the nuclear spin component $|\!\downarrow\rangle \equiv |m_I = -4\rangle$ and $|\!\uparrow\rangle \equiv |m_I = -3\rangle$. Since the m_I do not couple to optical transitions, the spins are conserved during the scattering of photons. Additionally, shifts in the energy levels between different m_I are negligible compared to those between different m_J. Hence, the schematic level structure in Fig. 7.3 is accurate for both spin states, which can be treated separately (but equally).

The electronic angular component m_J splits the ground state manifold $4\ ^2\mathrm{S}_{1/2}$ with $J = 1/2$ into 2 states. The $|m_J = -1/2\rangle$ (corresponding to $|F = 9/2\rangle$ at low magnetic fields) is the ground state and is detuned from the higher lying $|m_J = 1/2\rangle$ (or $|F = 7/2\rangle$ at low magnetic fields) by about $1.3\,\mathrm{GHz}$. The excited state manifold $4\ ^2\mathrm{P}_{3/2}$ has an electric angular momentum of $J = 3/2$ and is hence split into 4 states. The respective detunings between the states are on the order of $\sim 10\,\mathrm{MHz}$ and are hence not significant relative to the detuning in the ground state manifold.

Implementing dissipation via scattering of photons requires that after scattering a photon an atom will return to its initial state. This is important, as atoms in other states might see different lattice depths (due to different Stark shifts) or might interact differently with neighboring atoms. Also, the process of scattering a photon should happen on a timescale that is short compared to the microscopic timescale of the investigated Hamiltonian, which in our case is the hopping time τ. Additionally, the scattering rate from the ground state, which will ultimately define the coupling strength to the bath γ, needs to be easily controllable and be in a regime that is large compared to the tunneling time $1/\gamma \gg \tau$. This ensures that experiments are performed in the limit of weak couplings. In the opposite regime of a strong coupling, quantum Zeno effects would result in the localization of all atoms (see e.g. Ref. [219]).

In our system, these criteria can be met by choosing π-polarized light that is resonant with the transition from the higher lying ground state with $m_J = 1/2$ (indicated as red arrows). Atoms initially in the ground state see the light detuned by about $1.3\,\mathrm{GHz}$, and hence intensities of around $I_{\mathrm{scatt}} \sim 1\,\mu\mathrm{W/cm}^2$ result in scattering rates of about $\gamma \sim 30\,\mathrm{Hz}$, corresponding to approximately one photon every $100\,\tau$. The decay rate from the excited state is on the order of $6\,\mathrm{MHz}$ [117] and hence the duration of scattering a single photon can be neglected compared to the tunneling time. Additionally, the wavelength of the scattered photons of $766\,\mathrm{nm}$ results in a localization of the atoms on a length scale of $766\,\mathrm{nm}/2\pi \approx 120\,\mathrm{nm}$, which is smaller than the lattice spacing of $d = 532\,\mathrm{nm}/2 \approx 260\,\mathrm{nm}$. Hence, atoms will be localized to a single lattice site and higher bands will be excited.

7.3.1   Scattering bursts

Complications to the concept presented above emerge due to the split ground state manifold of ^{40}K: Not all atoms that absorb a photon decay back to the ground state. Instead, there is a probability of 33 % for the atoms to decay to the higher lying $|m_J = 1/2\rangle$ state in the ground state manifold, thereby not ending in the initial state. This problem is solved via the choice of the detuning of the scattering light. From the higher lying state in the ground state manifold, the atoms see the scattering light to be almost resonant (detunings on the scale of 10 MHz as compared to 1.3 GHz in the ground state). Since the absorption rate scales as $1/\delta^2$, where δ denotes the detuning, scattering from the higher lying state happens with a rate of hundreds of kHz, which is much faster than the tunneling time. The fast scattering of photons on this transition will continue until the atom, with a probability of 33 %, falls back into the ground state.

   Hence, after a first absorption from the ground state, atoms will either directly decay back to the initial state or, if they decay to the higher lying ground state, be transferred back to the initial state via the fast scattering of few photons. The total time of this process is much shorter than a tunneling time and hence the dynamics of the many-body lattice system during the burst can be neglected. As a result, considering the effects on the many-body system, the entire scattering process can be seen as the scattering of a single effective photon. This process will be referred to as a 'scattering burst'.

   While a scattering burst can be considered as a single photon considering the position-measurement effect, the number of photons in the burst does change the probability of the atom being excited to a higher band and being lost consecutively. As experimental measurements are always averaged over a large system it is, however, sufficient to consider the effects of an average scattering burst to describe the dissipative many-body system.

Rate of scattering bursts: The coupling strength to the external bath is set by the rate of scattering bursts γ, which can be set experimentally via the intensity of the dedicated scattering beam. This intensity is controlled by a feedback loop, which controls the voltage of a photodiode via an acusto-optic modulator. The photodiode is calibrated to the scattering rate γ in the following way:

   First, the voltage on the photodiode is calibrated on the total power of the scattering beam. Then, the scattering beam is imaged at the location of the atoms, and the total pixel count on the camera calibrated to the photodiode voltage. These pictures are then compared to in-situ images of the atom cloud, giving the intensity at the atoms' location I as a function of the photodiode voltage. The scattering rate corresponding to the intensity can then be calculated as

$$\gamma = \frac{3\pi c^2}{2\hbar\omega_{D_2}^3}\left(\frac{\Gamma_{D_2}}{\delta_{sc}}\right)I,\tag{7.4}$$

where c denotes the speed of light and ω_{D_2} and Γ_{D_2} the transition frequency and linewidth of the D_2 line of ^{40}K. The detuning $\delta_{sc} = 1.3$ GHz refers to the detuning seen by atoms in the ground state before the absorption of the initial photon. As the rate of any further

	$i = 0$	$i = 1$	$i = 2$	$i = 3$	$i = 4$
i_x	0	1	0	0	2
i_y	0	0	0	1	0
i_z	0	0	1	0	0

Table 7.1: Band indices: Spatially resolved band indices for the five lowest bands. Index 0 denotes the ground band.

scattered photons within a burst is orders of magnitude faster than the rate at which initial photons are scattered, they do not need to be considered for the rate of scattering bursts. The simple formula in equ. (7.4) can be used since the detuning to the D_2 line is much smaller than that to the D_1 line and hence the effects of the D_1 line need not be considered. Also, the detuning is large enough that one can assume that the hyperfine levels of the excited state are not resolved.

7.3.2 Band-excitation probabilities

A scattering burst generally has two effects on an atom: It localizes the atom onto a single lattice site, which implements the theoretical concept of dephasing, and it can, with a certain probability, excite the atom to a higher band of the lattice. If atoms in the higher band can tunnel out of the system, this implements a loss channel. In order to accurately understand and model the experimentally realized open quantum system, the respective probabilities of exciting to a higher band or remaining in the ground band have to be known. The simplest possible method to experimentally estimate the respective probabilities would be a measurement of the decay rate of the atom number for different scattering rates. However, as will be discussed later in section 7.3.3, in our setup, not all atoms that are excited to higher bands actually leave the system, rendering such a method unreliable. A more accurate method of determining the excitation probabilities is a detailed theoretical bandstructure calculation for the experimental parameters. First, the excitation probabilities of a single photon need to be calculated. Then, the average excitation probability of a scattering burst can be estimated.

Excitation probabilities for a single photon: The calculations of the excitation probabilities are carried out for the homogeneous system (no detuning lattice) with a $532\,\mathrm{nm}$ lattice along the **x** direction at a depth of $8\,E_r^{532\,nm}$ and two $738\,\mathrm{nm}$ lattices at $36\,E_r^{738\,nm}$ along the **y,z** direction respectively. Note that the calculations are specific to these lattice parameters (and the wavelength of the scattering light). The excitation probability of a single photon can be estimated by considering an atom initially in a Wannier state $|\Psi_{\mathrm{init}}\rangle = |W_i\rangle = |W_{i_x}\rangle|W_{i_y}\rangle|W_{i_z}\rangle$, where $|W_i\rangle$ denotes a Wannier state in the band with index $i \equiv \{i_x, i_y, i_z\}$. The band indices used for the calculation are split along the spatial directions according to table 7.1. In this lattice setup, the first excited band $1 \equiv \{1, 0, 0\}$

$P_{i\leftarrow j}$	$j=0$	$j=1$	$j=2$	$j=3$	$j=4$
$i=0$	0.823	0.103	0.023	0.023	0.016
$i=1$	0.103	0.582	0.003	0.003	0.229
$i=2$	0.023	0.003	0.772	0.000	0.000
$i=3$	0.023	0.003	0.000	0.772	0.000
$i=4$	0.016	0.229	0.000	0.000	0.406
"h_j"	0.011	0.080	0.201	0.201	0.348

Table 7.2: Single-photon band excitation probabilities: Probability $P_{i\leftarrow j}$ of being excited from the j-th to the i-th band by scattering a single photon. The spatially resolved components of the band indices can be found in table 7.1. Note that the second and third excited bands are degenerate, and hence the according excitation probabilities are equal. The values "h_j" sum up the probabilities of being excited to any band higher than the fourth excited band. Calculations were performed by Andrew Daley [70].

corresponds to an excitation along the **x** direction, but the ground band in the orthogonal directions. The second ($2 \equiv \{0,1,0\}$) and third ($3 \equiv \{0,0,1\}$) excited bands then correspond to the ground band in the **x** direction, but an excitation along the **y** or **z** direction, respectively. Due to the symmetry of the lattice setup, the second and third excited band are degenerate.

The probability $P_{i\leftarrow j}$ of starting in band j and being excited to band i after the absorption of a photon and subsequent reemission can be calculated as

$$P_{i\leftarrow j} = \int_{k_{ph}-\text{sphere}} \frac{d\Omega}{4\pi k_{ph}^2} \left| \langle W_{j_z}| \langle W_{j_y}| \langle W_{j_x}| e^{-i\mathbf{k}\cdot\mathbf{r}} e^{ik_{ph}x} |W_{i_x}\rangle |W_{i_y}\rangle |W_{i_z}\rangle \right|^2. \qquad (7.5)$$

This is the wavefunction overlap of the Wannier states of different bands with the operators corresponding to the momentum kick of the absorbed photon $e^{ik_{ph}x}$ and the emitted photon $e^{-i\mathbf{k}\cdot\mathbf{r}}$. Here, $\mathbf{k}$ denotes the wavevector of the respective photon with length $|\mathbf{k}| = k_{ph} = 2\pi/\lambda_{ph}$. Since the dedicated scattering beam is traveling along the **x** direction, the momentum kick of the absorbed photon is only in this direction. The emitted photon can, however, travel in any direction. Hence, the wavefunction overlap is averaged over the surface of the sphere spanned by all possible wavevectors with length k_{ph}. The resulting probabilities are summarized in table 7.2. According to the definition of $P_{i\leftarrow j}$ in equation 7.5, the probabilities of reaching any band in an infinite sized lattice should be one. The calculation, however, only includes the lowest five bands. The probabilities of being excited to any higher bands h_j are summed up in the last row. The values h_j are chosen such that the normalization $\sum_{i=0}^{4} P_{i\leftarrow j} + h_j = 1$ holds.

Average excitation probabilities for a scattering burst: Based on the above calculations for the band-excitation probabilities of a single photon, we can estimate the probabilities for an average scattering burst. As discussed above, a scattering burst can consist of n
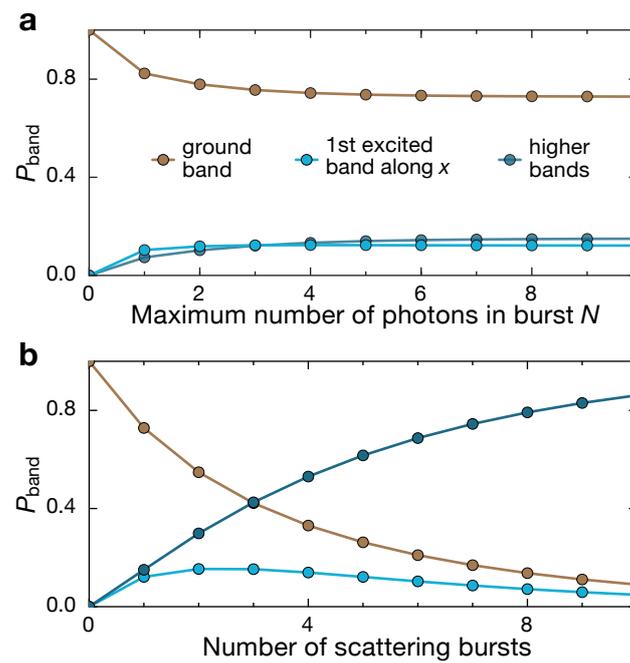
Figure 7.4: Band excitation probabilities of a scattering burst: a) Convergence of the sum in equation 7.6. The average band-excitation probability of a scattering burst is given by the limit of $N \to \infty$, where N is the maximum number of photons in a scattering burst. b) Band excitation probabilities as a function of the number of scattering bursts. The probabilities are shown for the ground and the first excited band. All other populations are summed up and plotted together as 'higher bands'. Calculations were performed by Saubhik Sarkar and Andrew Daley [70].

individual photons, where $n \in [1, 2, 3, 4, ...]$. The first photon is scattered from the ground state. With a probability of 2/3, the atom decays back into the ground state, thereby ending the scattering burst. With a 1/3 probability, however, the atom decays into the higher lying state in the ground state manifold, from which it can quickly cycle an arbitrary number of photons. Each photon will bring the atom back to the ground state with a 1/3 probability (see section 7.3.1 for a detailed discussion). The average band-excitation probability $P_{i \leftarrow j}^{\text{burst}}$ of a scattering burst can be calculated as the sum of the excitation probabilities after scattering n photons, weighted by the probability $P_{\#}(n)$ to scatter n photons in a scattering burst

$$P_{i \leftarrow j}^{\text{burst}} = \sum_{n=0}^{N \rightarrow \infty} P_{\#}(n) \, (P_{i \leftarrow j})^n. \qquad (7.6)$$

Here, $P_{i \leftarrow j}$ is the transition matrix containing the single-photon band-excitation probabilities shown in table 7.2. The probability of scattering n photons in a burst can easily be derived as

$$P_{\#}(n) = \begin{cases} \dfrac{2}{3}, & n = 1 \\ \dfrac{1}{9}\left(\dfrac{2}{3}\right)^{n-2}, & n \geq 2 \end{cases} \qquad (7.7)$$

which quickly converges to zero for large n. Hence, the sum in equation 7.6 also quickly converges. Note that since the transition matrix $P_{i \leftarrow j}$ is only calculated up to the fourth band, return processes from any higher bands are not considered, potentially slightly changing the probabilities $P_{i \leftarrow j}^{\text{burst}}$. However, due to the low occupations in the higher bands, this should result in corrections below 1 %.

Fig. 7.4a shows the probabilities $P_{i \leftarrow 0}^{\text{burst}}$ of remaining in the ground band $\{0, 0, 0\}$ and being excited to the first excited band $\{1, 0, 0\}$ by a scattering burst, starting in the ground band, as a function of the number of photons N considered in the sum in equation 7.6. It is clearly visible, that the sum quickly converges. The limit of $P_{0 \leftarrow 0}^{\text{burst}}$ for $N \rightarrow \infty$ of remaining in the ground band is the average probability of a scattering burst to result in dephasing, and hence the dephasing rate γ_{deph} in the system is given as

$$\gamma_{\text{deph}} \approx 0.7 \gamma. \qquad (7.8)$$

Fig. 7.4b shows the probabilities of finding an atom in different bands as a function of the number of scattering bursts, starting in the ground band. We see, that the probability of an atom being excited to higher bands quickly increases. After about 10 scattering bursts, the chance of an atom remaining in either the ground or first excited band is almost zero. Hence, the implemented method for studying dissipation can only address the weak scattering limit, as a too strong scattering will lose atoms too quickly.

Probability of a spin-flip: An additional mechanism that has so far not been considered, is the potential flipping of the spins $|\downarrow\rangle \equiv |m_I = -4\rangle$ and $|\uparrow\rangle \equiv |m_I = -3\rangle$ during the scattering of photons. In the Paschen-Back regime, where the quantum numbers I and J are uncoupled, the m_I should be conserved during optical transitions. However, the ground
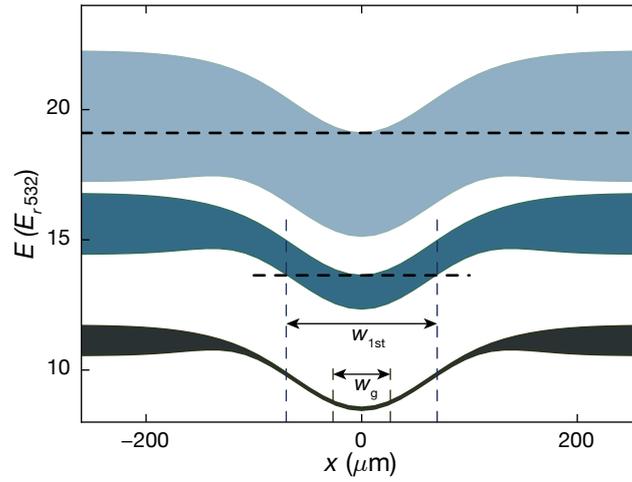
Figure 7.5: Spatial Bandstructure: Upper and lower band-edge of the bands with indices $i =$ 0, 1, 4 along the **x** direction at $y, z = 0$. The structure emerges due to the Gaussian shape of the lattice and dipole beams. The experimentally measured size of the atom cloud in the ground band is denoted as w_g. The horizontal dashed lines illustrate the criterion of whether a band is trapped or not, showing that the first excited band is indeed trapped. The width w_{1st} that an atom cloud in this band is expected to expand to is in good agreement with in-situ absorption images of the atom cloud.

state manifold is, at the magnetic fields of around 200 G used in the presented experiments, not fully in the Paschen-Back regime yet. Hence, there is a remaining coupling between m_J and m_I resulting in the flipping of spins. The probabilities can be calculated by including the nuclear spin and considering the exact hyperfine structure in the calculation of the branching ratios. The probabilities for a spin flip are found to be 4 % for $|\downarrow\rangle$ and 10 % for $|\uparrow\rangle$. Most of the occurring spin flips convert atoms between those two spin states, which will on average not alter the global system too much. However, also atoms with $m_I = -2$ can be created. These atoms would have a significantly different interaction strength with the other spin states. Due to the small probability of creating these atoms, however, the effects are expected to be minimal, and indeed spin-resolved images of the cloud never showed a measurable fraction of atoms in the $m_I = -2$ state.

7.3.3 Atom-loss mechanism

Atom loss due to photon scattering relies on not only atoms being excited to higher bands, but also on these atoms quickly tunneling out of the system. Generally, the quasiperiodic potential seen by atoms in the excited bands will be much weaker and the tunneling rates much higher. Hence, excited band atoms will be both delocalized and fast. In order to leave the system, however, atoms additionally need to be untrapped. This is a similar criterion as for the expansion of a cloud, discussed in section 2.4.2. Namely, the kinetic energy of an atom, given by the bandwidth, needs to be larger than the depth of the harmonic confinement. This criterion is illustrated in Fig. 7.5 for the lowest three
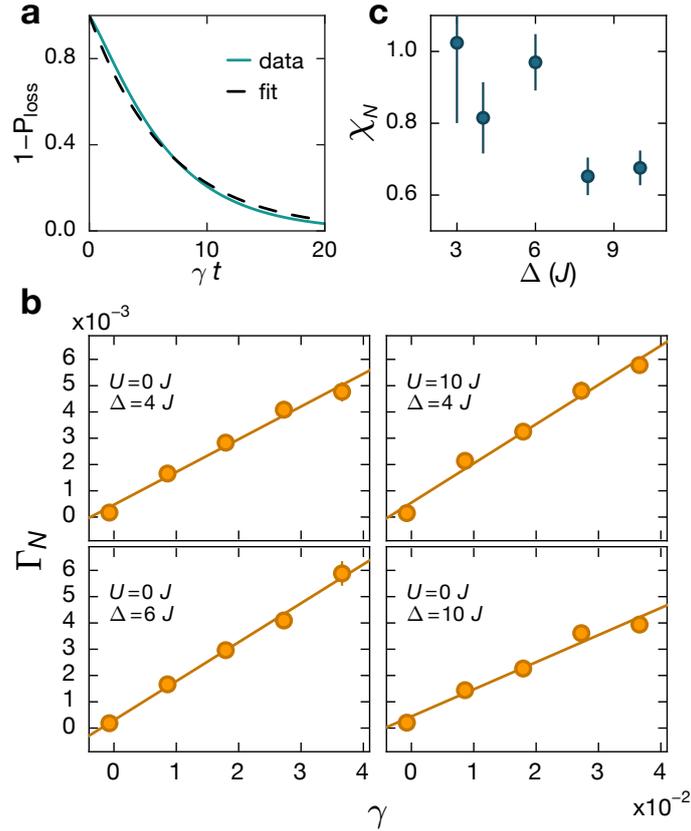
Figure 7.6: Atom losses: a) Calculated probability of remaining in the system based on the excitation probability to beyond the second excited band along **x** $\{2, 0, 0\}$. The dashed line indicates an exponential fit to extract γ_{loss}. b) Linear relationship of the measured atom number lifetime Γ_N versus the scattering rate γ for different parameters of the system. The slope of a linear fit can be used to extract χ_N. c) Experimentally measured values of χ_N for different strengths of the detuning lattice Δ. Ideally, $\chi_N = 1$ for all Δ.

bands of the primary 532 nm lattice $\{0,0,0\}$, $\{1,0,0\}$ and $\{2,0,0\}$ (i.e. bands with indices $i = 0,1,4$ according to table 7.1). While the $\{2,0,0\}$ band is clearly untrapped, the first excited band $\{1,0,0\}$ is still trapped, and hence atoms will not be able to leave the system. This calculation was experimentally confirmed by deliberately loading atoms into the first excited band and monitoring their time evolution. It was found that the lifetimes in the second band are only slightly smaller than those in the first band. Additionally, the atom cloud expanded to a width of $w_{1st} \approx 150\,\mu$m, which agrees well with the prediction by the calculation. Bandstructure calculations have further shown, that bands with excitations only in the **y** and **z** direction (especially $\{0,1,0\}$ and $\{0,0,1\}$), remain trapped as well. These bands are less relevant though since the number of atoms excited into them is comparatively small. Still, a significant number of atoms can occupy these bands, as at the edges of the system they are resonant with the first excited band in the **x** direction $\{1,0,0\}$. This is also checked experimentally by loading atoms into the first excited band and imaging after bandmapping. Indeed, it was found that atoms redistribute between these bands. Likely, this is also the reason why the second band atoms do not dominantly show up on the bandmapped images taken to extract the imbalance (see e.g. Fig. 2.7).

Due to the first excited band $\{1,0,0\}$ being trapped, the rate at which atoms leave the ground band is not equal to the rate at which atoms get lost from the system. Instead, a significant amount of atoms will remain in the delocalized first excited band. The theoretically expected population of this band as a function of the number of scattering bursts per atom is shown in Fig. 7.4b.

In order to estimate the rate at which atoms actually get lost from the system, we need to consider the rate at which atoms are excited to the $\{2,0,0\}$ band (or higher). The probability for an atom being lost as a function of time can hence be estimated by the probability of an atom being excited to the $\{2,0,0\}$ band after n scattering bursts, weighted by the probability $P_{\text{burst}}(n,t)$ of having n scattering bursts up to time t, which is given by a Poisson distribution

$$P_{\text{burst}}(n,t) = \frac{(\gamma t)^n e^{-\gamma t}}{n!}. \tag{7.9}$$

The result is plotted in Fig. 7.6a. While the decay does not precisely follow an exponential, it can be well estimated by one, as is indicated by the dashed black line. As a result of this fit, we get an estimate of the expected loss rate γ_{loss} of

$$\gamma_{\text{loss}} = 0.17\gamma. \tag{7.10}$$

In order to check this estimation, we define an atom number susceptibility to the photon scattering

$$\chi_N = \frac{d\Gamma_N}{d\gamma_{\text{loss}}}, \tag{7.11}$$

where Γ_N is the atom-number decay rate. This quantity can be measured experimentally by monitoring the atom number decay in a system exposed to photon scattering for different scattering rates γ. The atom number decay rate Γ_N can then be extracted using an

exponential fit. As illustrated in Fig. 7.6b, a linear behavior is found between Γ_N and γ. The atom number susceptibility can be calculated from the slope. By definition, we would expect $\chi_N = 1$, if our model for atom loss is accurate. Experimentally measured values for different strengths of the incommensurate potential are shown in Fig. 7.6c. The values show a strong scatter but are roughly consistent with $\chi_N = 1$. Overall, the experiment slightly underestimates χ_N, suggesting that even fewer atoms are lost than is expected from the calculations. This could be due to an uncertainty in the extraction of Γ_N itself. As time-resolved measurements have been taken primarily to investigate the behavior of the imbalance, they have not been taken to long enough times for the atom number to fully decay. This could make the exponential fits to the atom number unreliable, explaining the large amount of scatter and the systematic error.

## 7.4   Experimental results on the open system

In this section, we will present results on open MBL systems that we obtained by applying the developed method of scattering near-resonant photons (see section 7.3) to our MBL system. Our experimental results will be compared to numerical simulations of the corresponding Lindblad equation (see section 7.2). We will focus on the fully localized MBL phase. A study of the effects of external baths in the regime of slow dynamics on the thermal side of the phase transition has not been attempted yet.

To investigate the effects of the controlled photon scattering on an MBL system, we measure long-term time traces of both the imbalance $\mathcal{I}$ and the atom number N for various detuning and interaction strengths. Fig. 7.7 shows exemplary data at an interaction strength of $U = 4J$ and a detuning strength of $\Delta = 4J$. We find that generally any added scattering results in a faster decay of both the imbalance $\mathcal{I}$ and the atom number N. This is consistent with the picture of external couplings destroying localization and can be explained based on the picture described in section 7.3 (compare also Fig. 7.2): Scattering a photon will localize an atom on the length scale of the wavelength of the scattered photon $\lambda/2\pi$. In our system, this length scale compares to the lattice spacing d as $\lambda/(2\pi d) \approx 0.45$. Hence, an atom can either be localized to a Wannier state in the ground band, or it can be excited to a higher band. As we choose low scattering rates γ of only a few photons every $100\,\tau$ per atom, an atom can time evolve under the closed system's Hamiltonian between successive scattering events. The time evolution of an atom after being re-located resembles the time evolution of atoms after the initial quench. Since, however, the starting Wannier state can be different, the scattering induced relocation of atoms in the lowest band essentially re-enables hopping. Atoms excited to higher bands will ideally leave the system, as the excited bands have stronger tunnel couplings and are delocalized. Scattering can hence be described as a dephasing rate $\gamma_{dp} = p_{dp} * \gamma$ which describes the rate at which atoms are localized to Wannier states within the lowest band, and an excitation rate to higher bands $\gamma_{ex} = (1 - p_{dp})\gamma$. Here $p_{dp} \approx 0.7$ denotes the probability of a scattering event resulting in dephasing. The ratio of dephasing and excitation rate is given by
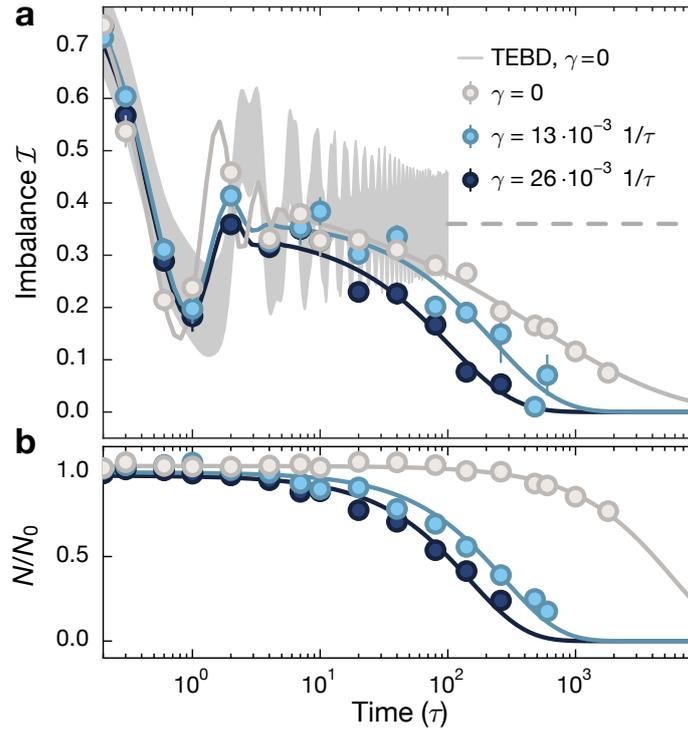
Figure 7.7: Imbalance and Atom number decay in the presence of photon scattering: a) Time evolution of the imbalance at $\Delta = 4\,J$ and $U = 2\,J$ for various scattering rates γ on a logarithmic time axis. Points denote experimental data, averaged over six realizations of the quasi-periodic pattern ϕ with the errorbars indicating the uncertainty of the mean. Lines are stretched exponential fits to extract the lifetime of the imbalance. The gray shaded region marks the result and statistical uncertainty of TEBD simulations on the closed system ($\gamma = 0$). The dashed line extrapolates its mean value. b) Time evolution of the relative atom number, fitted by simple exponential fits to extract the atom number lifetime. TEBD simulations were performed by Mark Fischer and Ehud Altman [70].

a

b
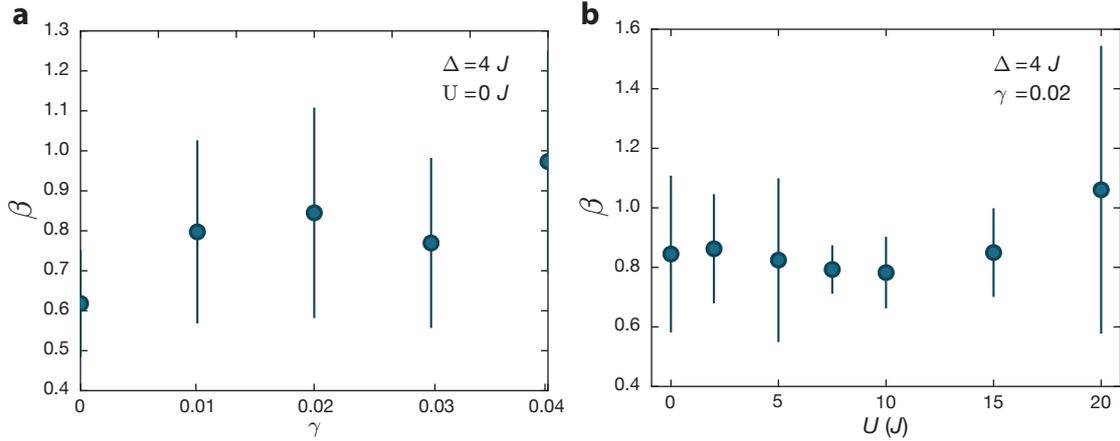
Figure 7.8: Fitted stretching exponents: a) Stretching exponents β at $\Delta = 4\,J$, $U = 0$ as a function of the scattering rate γ. Errorbars denote the uncertainty of the fit to the imbalance time traces. b) Stretching exponent at a fixed scattering rate of $\gamma = 0.02/\tau$ as a function of the interaction strength U.

the wavelength of the scattered photons and the lattice geometry and is hence not easily adjustable in the experiment. In our experiments, it is fixed at $\gamma_{dp}/\gamma_{ex} \approx 2.3$. This value is obtained from ab-initio calculations for our system, which were discussed in section 7.3.2. Note that in our system the excitation rate does not directly give the atom number loss rate as atoms in the first excited band are trapped in the system by the dipole trap (see section 7.3.3).

To analyze the time traces, we extract the atom number decay rate Γ_N via simple exponential fits. An analysis of the atom number lifetimes is given in section 7.3.3. The decay rate of the imbalance $\Gamma_\mathcal{I}$ is extracted via a fit to the function

$$\mathcal{I}(t) = \left(A\cos(\omega t)\, e^{-\Gamma_1 t} + o \right) \times e^{-(\Gamma_\mathcal{I} \times t)^\beta} \tag{7.12}$$

where ω and Γ_1 describe the initial oscillating decay to the plateau value o. This function is wrapped in a stretched exponential envelop with the stretching exponent β, describing the effects of the external decays. The stretched exponential fits are motivated by previous theoretical analysis, which commonly found this functional form (see e.g. [208]). Intuitively, the stretched exponential form can be understood as a superposition of external decays with slightly different timescales [196]. In systems with random disorder, different timescales can emerge due to variations in the local disorder strength, which also underly the Griffiths mechanism. Note, however, that the very local action of a photon bath does not require these variations to be present on large length scales. Instead, it is sufficient if close-by sites show different energy differences, which is present also in quasi-periodic systems.

Experimentally, we found that stretched exponential decays fit the imbalance data slightly better than simple exponential decays. Fig. 7.8 shows exemplary exponents as a function of the interaction strength U and the coupling rate γ. The extracted stretching
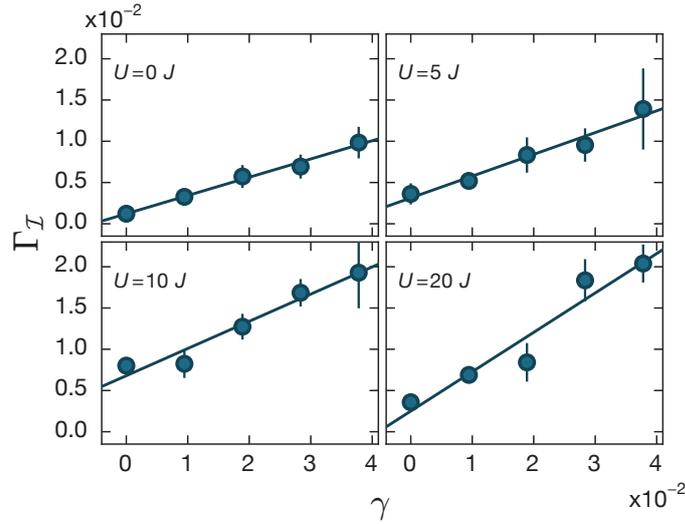
Figure 7.9: Imbalance decay rate versus scattering rate: Experimentally extracted decay rates of the imbalance as a function of the scattering rate γ for various interaction strengths U at $\Delta = 4\,J$. Errorbars show the uncertainty of the stretched exponential fit. Solid lines are the linear fits used to extract the susceptibility.

exponents do not show any significant trend with the detuning or the interaction strength and scatter strongly between values of approximately $\beta \approx 0.5$ and $\beta \approx 1$. This is likely because the stretching exponents are mostly determined by the decay at longer times, where the imbalances are already low and hence the signal to noise ratio becomes poor. Additionally, we have found that the value of the fitted stretching exponent is not strongly influencing our data analysis. This can e.g. be seen in Fig. 7.10, where we compare data extracted using the described fitting procedure to the data extracted using simple exponential fits (i.e. a fixed $\beta = 1$) and only find minor differences.

Definition of the susceptibility: As is illustrated in Fig. 7.9 for different interaction strengths at $\Delta = 4J$, we find an approximately linear behavior of the imbalance decay rate with the scattering rate. This behavior is present for all values of Δ and U in the localized phase. The slope of the linear behavior, as well as the offset, depend heavily on Δ and U. While the varying offset is already well understood as being dominated by the coupling between neighboring tubes (see section 7.1), the slope describes the susceptibility of the system to photon scattering. To investigate the effects of photon scattering without crosstalk from the coupling mechanism, we define the susceptibility χ of the system to the effects of photon scattering as

$$\Gamma_{\mathcal{I}} = \chi \gamma + \Gamma_{bg}, \qquad (7.13)$$

where Γ_{bg} denotes the offset due to other decay mechanisms. The susceptibility can hence be extracted as the slope of linear fits to the imbalance decay rate, which are indicated as solid lines in Fig. 7.9. Note that this model implies that the effects of photon scattering
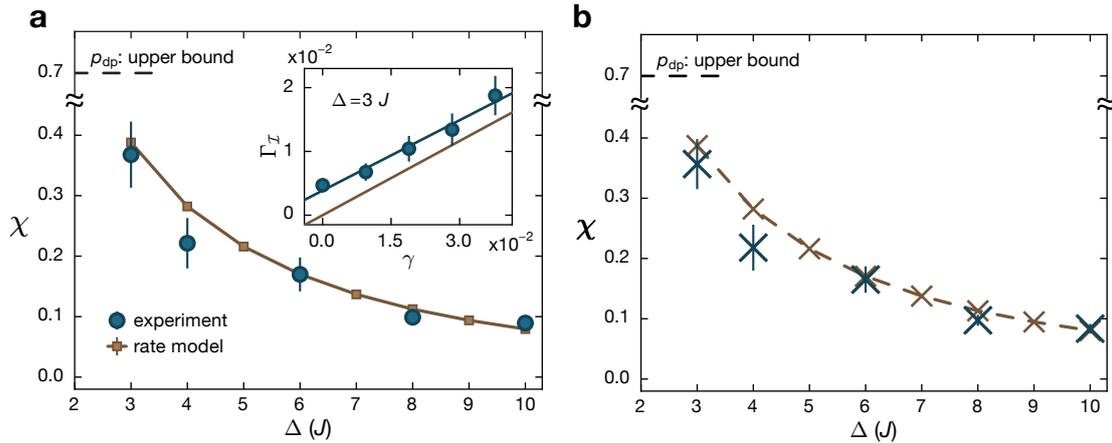
Figure 7.10: Non-interacting susceptibility vs. detuning strength: a) Experimental and theoretical susceptibility at $U = 0$ for various detuning strengths. Errorbars denote the uncertainty of the fit. The theoretical results are extracted from a rate model [196]. The black dashed line indicates the theoretical upper bound of the susceptibility in the extended phase. The inset shows the linear behavior of the imbalance decay rate with the scattering rate. The solid line indicates the linear fit used to extract the susceptibility. The theoretical rate model yields the same slope but has an offset relative to the experiment. This is due to other decay mechanisms present in the experiment (see section 7.1). b) Susceptibilities as in a) but extracted using simple-exponential fits instead of stretched exponential fits. Numerical simualtions were performed by Mark Fischer and Ehud Altman [70].

and any other decay mechanisms are independent and do not influence each other. While, in general, this need not be true, the linear slopes found experimentally suggest that it is a sufficiently good approximation.

7.4.1   Single-particle results

In order to check the modeling of our photon bath described in section 7.3, we first analyze the non-interacting system. In the absence of interactions, numerical simulations are easily performable, which allows us to crosscheck the obtained results. Fig. 7.10 shows the extracted non-interacting susceptibilities as a function of the detuning strength Δ. We find that the susceptibility decreases with increasing detuning strength. This is in very good agreement with the numerical simulations, which are performed using the rate equation model presented in Ref. [196]. Since this model only implements the effects of dephasing, its scattering rate is rescaled by the factor $p_{dp} = 0.7$. This should give an exact prediction of the experimental result, as in the absence of interactions we expect that band excitations (atom loss) have no effect on the imbalance. This is because loss processes occur on even and odd sites with identical rates. The inset of Fig. 7.10 shows an exemplary comparison of the extraction of the susceptibility between the experiment and the rate model. As expected, the rate model displays the same linear relationship between imbalance decay rate and scattering rate as the experiment. However, its linear

behavior does not show any offset, as no additional decay mechanisms are present. Good agreement regarding the effects of photon scattering is thus present if the linear fits are parallel, i.e. have the same slope and hence yield the same susceptibility. Indeed, we find very good agreement between the rate model and the experiment.

The lower susceptibility at larger detuning strengths can be easily understood via a simple model that was also described in Ref. [196]. The susceptibility essentially depends on the probability of a scattering event transferring a particle, described by a localized wavefunction around a central lattice site, to a neighboring site. If at very large detuning strengths, the localization length is so small that the wavefunction overlap of the particle with the neighboring lattice sites is essentially zero, a scattering event can only result in the localization back onto the same Wannier state, resulting in a vanishing susceptibility. At lower detuning strengths, however, where the localization length is large and hence neighboring lattice sites strongly contribute to the wavefunction of the particle, the probability of a scattering event transferring a particle to a neighboring site is comparatively large and hence the susceptibility is high. This picture also allows for the derivation of a simple upper bound for the non-interacting susceptibility in the extended phase. In the extended phase, every particle is completely delocalized, and hence a scattered photon will result in the localization of a particle onto an even or an odd site with equal probability. Hence, every atom will have an imbalance of zero after a single scattering event. The imbalance thus decays with a rate γ_{dp}, giving an upper bound for the susceptibility of $\chi_{max} = p_{dp}$. In our system, we cannot access this limit, as the imbalances become too small below a detuning strength of $\Delta = 3J$ and hence the stretched exponential fits used to extract the imbalance decay rates are not reliable anymore.

7.4.2 Many-body results

In the presence of interactions, we expect the susceptibility to be generically larger than in the single-particle case. This is due to e.g. a larger spreading of the interacting wavefunction at the same detuning strength, as well as interacting dephasing events possibly affecting close-by atoms. Additionally, also atom losses might perturb atoms in their surroundings [196]. Hence, we do not expect the upper bound of the susceptibility derived for non-interacting particles to hold. A further increase of the susceptibility may arise due to an effect that is rather specific to our setup: In the presence of interactions also the atoms trapped in the first excited band (see section 7.3.3) can contribute a decay mechanism, as they are delocalized and can hence serve as an additional bath.

The experimentally extracted interacting susceptibilities are shown in Fig. 7.11 as a function of the interaction strength for two different detuning strengths close to the transition ($\Delta = 4J$) and well in the localized phase ($\Delta = 6J$). We find that interactions show almost no effect on the susceptibility deep in the localized phase, but find a pronounced effect at $\Delta = 4J$. This observation is consistent with the picture that interactions play an important role close to the transition, but show little effect deep in the localized phase. Close to the phase transition the susceptibility continuously increases with the interaction
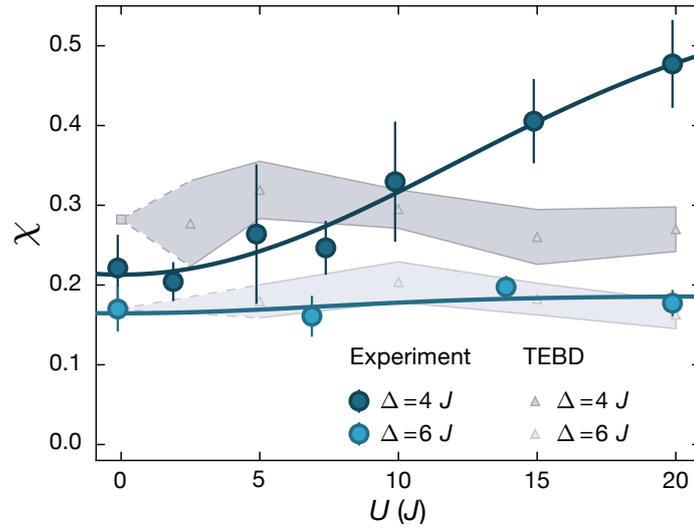
Figure 7.11: Susceptibility vs. interaction strength: Experimentally measured susceptibilities as a function of interaction strength U for different detuning strengths Δ. Errorbars indicate the uncertainty of the fit. Solid lines are guides-to-the-eye. The gray shaded regions show the result and statistical uncertainty of numerical TEBD simulations that do not include particle loss. TEBD simulations were performed by Mark Fischer and Ehud Altman [70].

strength U. We expect this increase to saturate in the hard-core limit. The experimental susceptibilities are compared to numerical simulations. Since the rate model [196] was only developed for the non-interacting case, we use TEBD simulations that implement dephasing via a Lindblad equation (see section 7.2). Implementing the effects of atom loss was not possible, as the simulations close to the phase transition would have been too demanding. Hence, for the shown simulations the scattering rate of the numerical simulations has been rescaled by p_{dp} (as in the non-interacting case) and the effect of atom losses are not considered. Still, our TEBD simulations show large truncation errors and hence need to be interpreted with care. Note that a further theoretical study has managed to investigate the combined effect of both particle loss and dephasing in a randomly disordered spin system [217]. Deep in the localized phase, numerics and experiment agree very well and neither shows an effect of interactions. This suggests, that atom loss is unimportant in this regime, which is to be expected if interactions generally show no large effect. Close to the phase transition, both experiment and numerics show an increased susceptibility at intermediate interaction strengths. However, in the regime of strong interactions, we observe deviations between the experiment and the numerics. The numerical susceptibilities come back to their non-interacting value in the hard-core limit, which is the expected result if particle numbers are conserved. The experiment, where particle loss is present, shows a dramatically different behavior. Hence, the difference likely reflects the effects of particles being lost from the ground band. That the effects of particle loss become increasingly relevant with increasing interaction strength is consistent with the results of

Ref. [217]. Further investigating the interplay of dephasing and atom loss experimentally is not possible, since the ratio of dephasing to loss events in our setup is fixed.

We note, that close to the phase transition at $\Delta = 4J$, the lifetimes of the imbalance and the atom number become comparable in the presence of scattering. Thus, the system is subjected to a significant change in the density during the decay of the imbalance. As a lower density also implies that interaction effects become less significant, we would also expect a change in the functional form of the imbalance decay rate with time, i.e. a faster decay rate at short times, where the density is large and hence atom number loss significantly affects the imbalance, but a slower tail where the density is low and the problem effectively becomes non-interacting. However, from our data, we cannot resolve such an effect. This is likely due to the measurement of the imbalance being less reliable when the atom numbers are low. Additionally, the described effect might not be cleanly resolvable, as the decay of the imbalance is not given only by the scattering of photons, but also limited by other effects (see section 7.1).

Another difference between the experiment and the numerics are the effects of the particles trapped in the first excited band in the experiment. Understanding their mechanism is closely related to understanding the effects of a 'small' bath [51, 52, 76], which describe finite delocalized systems coupled to a many-body localized system. Gaining a better understanding of the effects of trapped second band atoms is thus a very interesting task for future works.

7.5   Discussion

Truly many-body localized systems have to be completely isolated from the environment. However, this is not possible in nature, which raises the question how the study of MBL is important in any practical context. This question is similar to the question of the relevance of ground state quantum phase transitions when practical situations always happen at finite temperatures. In this case, it was found that although quantum critical points only exist at zero temperature, their presence can influence a system even at finite temperatures (compare Fig. 6.1). Based on our findings on the response of the MBL systems to coupling and photon scattering in the localized phase, as well as the influence of external couplings on the power-law decays found on the thermalizing side (see section 6.4.1), a similar picture emerges, as is illustrated in Fig. 7.12. While true many-body localization can only exist in a fully isolated quantum system, its properties can remain relevant on intermediate timescales even in the presence of a bath. This is because signatures of an MBL system are destroyed on a timescale that is inversely proportional to the coupling strength of the bath. In a weak coupling regime, the properties of the MBL system thus dominate the short time response of the system. The definition of 'short times' here depends on the susceptibility of the system. Close to the phase transition, where the system is more susceptible, even weak coupling strengths can e.g. erase the imbalance on rather short timescales. Deep in the localized phase, a small coupling might only erase the imbalance after $\sim 1000\,\tau$.
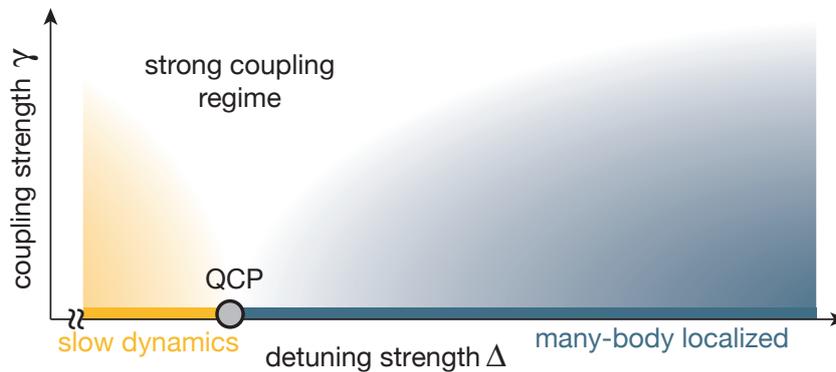
Figure 7.12: Schematic phase diagram of an open MBL system: Coupling an MBL system to a bath destroys the signatures of the system on a timescale that depends on the coupling strength γ. Signatures might e.g. be a persistent imbalance in the MBL phase or a power-law decay of the imbalance in the thermalizing phase. The yellow and blue shaded regions indicate the regimes where those quantities are still accessible. In the white regime of strong couplings, the bath dominates the dynamics of the system completely. The true phases and an actual transition exist only at $\gamma = 0$. The diagram is reminiscent of the phase diagrams of ground state quantum phase transitions with the temperature on the y-axis.

The blue and yellow shading in the figure directly correspond to the discernibility of the imbalance and the power-law decays in the weak scattering limit. Outside of these regions, the external bath thermalizes the system on extremely short timescales and properties of the underlying MBL system are unimportant. The coupling strength at which the MBL system's properties become unimportant reduces close to the phase transition. This is a consequence of the increased susceptibility that was found when approaching the transition. Indeed, we speculate that the susceptibility in an interacting system might even diverge at the phase transition in the limit of weak scattering. This is, however, not observable in the experiment, as the definition of weak scattering implies that the rate of scattering is slow compared to intrinsic system timescales, which also diverge at the phase transition. Hence, any experimental scattering rate will eventually leave the weak scattering limit.

On the thermal side of the transition, the shading is oriented on the discernibility of the power-law decays and is directly related to the power-law exponent α (see chapter 6). When the transition is approached, the internal power-law decays become slower (the exponent decreases) and hence the imbalance decay resembles an exponential decay. Further away from the transition, where the internal dynamics are fast, much stronger coupling strengths are required to influence these decays. A systematic study of the effect of photon scattering on the slow dynamics on the thermal side has not been performed yet but is a worthy goal for future work.

Conclusion and outlook

In this thesis, we have described in detail how cold atoms in quasi-periodic optical lattices can be used to study localization phenomena both in a single particle and a many-body context. We gave the relevant background of earlier studies, mostly theoretical, and presented new experimental results based on measurements of out-of-equilibrium observables. Specifically, we characterized a single-particle mobility edge in our quasi-periodic lattice and investigated the thermalization dynamics close to the MBL phase transition in the context of the Aubry-André model. Furthermore, we described a newly developed method to implement a controlled bath to cold atom experiments and used it to study MBL in an open quantum system.

In part I, **chapter 2**, we described the experimental setup in detail and compared its Hamiltonian to both the Aubry-André and the Anderson model, which are typically studied in the context of localization. We showed that our system should map onto the Aubry-André model in the tight-binding limit of nearest neighbor hopping and discussed the dominant corrections to this mapping. Furthermore, we introduced the imbalance and the expansion as our dynamical observables and gave a basic overview of their experimental implementation. In **chapter 3**, we discussed how the expansion and the imbalance can be used to sensitively detect the presence of extended and localized single-particle states respectively, and used this property to map out the full phase diagram of the non-interacting quasi-periodic lattice. We found an intermediate phase, where a single-particle mobility edge is present, separating the fully localized from the fully extended phase. In the tight-binding regime, the intermediate phase was found to vanish. This is expected as here the lattice model should be well described by the Aubry-André model, which does not have an intermediate phase, and indeed measurements of the imbalance showed good agreement with calculations based on the AA model, suggesting an accurate mapping.

In part II, we contrasted many-body localization, i.e. the localization of interacting particles in highly excited states, to the generically expected behavior of thermalization. After briefly discussing the current understanding of the respective thermal and MBL phase in **chapter 4**, the experimental implementation of interactions was introduced in **chapter 5**. Here, the basic experimental signatures of the MBL phase were discussed and the influence of the doublon fraction, density, and temperature of the initial state were shown. Based on these observations, we chose the initial state with lowest doublon fraction and

temperature, as well as the highest achievable density to be best suited for studying MBL in the following chapters.

Using this initial state, in **chapter 6**, we investigated the dynamic behavior of the imbalance close to the MBL phase transition. On the thermalizing side, we found increasingly slow relaxation dynamics when approaching the transition. These dynamics were similar to those numerically observed in randomly disordered systems. This is surprising, as in disordered systems such slow dynamics are possibly based on the relaxation of rare Griffiths regions, which cannot exist in quasi-periodic settings. We discussed possible reasons for this similarity, including Griffiths regions in the initial state and anomalous distributions of transition rates between single-particle eigenstates. Furthermore, we argued that the detuning strength where the observed relaxation dynamics stop can be used as an estimate of the phase transition point and gave bounds on the transition point from the experimental data.

In **chapter 7**, we described a newly developed method for implementing a controlled bath to cold atom systems via the scattering of near-resonant photons. These photons cause both a localization of the particles to the length scale of the scattered photon, as well as the loss of particles. We compare ab-initio calculations to experimental results and show a good understanding of both the coupling rate to the photon bath, as well as the ratio of localization to loss events. Challenges remain in the understanding of the loss channels, as in our system particles excited to the first excited band of the optical lattice remain trapped in the system. We further apply the developed method of implementing controlled baths to the MBL phase, where we find a linear dependence between the relaxation rate of the imbalance and the coupling rate. We characterize this linear dependence by introducing the susceptibility, for which we find very good agreement between theory and experiment in the absence of interactions. In the presence of interactions, the experiment shows a strong influence of atom loss on the imbalance decay rate, which could not be assessed numerically.

8.1   Outlook

The works presented in this thesis (as well as those presented in earlier theses in Refs. [114, 115]) experimentally show the existence of MBL, as well as many intriguing phenomena, such as the thermalization dynamics close to the phase transition. However, all experimental results in this thesis were also accessible using current numerical techniques. While a full calculation of the experimental system is never numerically feasible, deep in the MBL phase only small system sizes are required to reproduce the behavior, and approximate methods such as DMRG can readily be employed. Close to the phase transition, where larger system sizes are required to access the critical scaling regime, current experiments fail to access the necessary long times due to couplings to external baths. Thus, even though the limitations are very different in nature, the accessible physics is currently very similar in both experiment and theory. Future experiments need to aim to

break these barriers by improving the systems' lifetimes. The lifetimes are currently mostly limited by a coupling between adjacent tubes [69], however, increasing orthogonal lattice depths only give marginal improvements and would result in an enhanced scattering rate of lattice photons. Solutions hence have to be looked for in either removing orthogonal planes (as e.g. in Ref. [64] in two dimensions) or by decreasing the effectiveness of the orthogonal directions as baths by e.g. adding detunings. Further, optical lattices need to be created from very far detuned wavelengths to limit the number of scattered photons, and tunneling times need to be reduced. This can e.g. be achieved via shorter lattice spacings or by employing atoms with a lower mass. In our system, another possible improvement can be achieved in the relative motion of the primary versus the detuning lattice by locking the two lasers relative to each other.

Much of the interesting behavior that is currently not understood appears at long evolution times, and in regimes where the imbalance will likely ultimately decay to zero. An improvement of the lifetimes of the imbalance can hence only be exploited when a simultaneous improvement in the detection of the imbalance is achieved. Here, both an increased accuracy in the absolute value, as well as a reduction of the noise are necessary.

Given that significant improvements in the lifetime and detection accuracy can be achieved, the presented setup can be used to explore a large variety of MBL phenomena that are inaccessible to numerics due to finite size restrictions. Most of these phenomena are related to the problem of small baths, which describes the interaction between an MBL system and a small bath with a finite number of degrees of freedom. This problem arises not only in the obvious context of many-body localization in the presence of a single-particle mobility edge [53] and the question of the existence of a many-body mobility edge [80], but also in the context of Griffiths regions close to the phase transition [38]. Generally, one could expect that any extended states generically delocalize the MBL states, resulting in a purely thermal behavior. This is, however, only necessarily the case if the thermal states are topologically protected [72, 75] and the coupling rate is outside of the quantum Zeno regime. Otherwise, numerical studies have pointed to the possibility that indeed also the MBL phase can, in some cases, localize the extended states, thereby stabilizing the MBL phase [51, 52, 76, 146, 202]. This phenomenon was termed the many-body localization proximity effect [202]. In the following, we will discuss the possibility of studying the effects of small baths in our experimental system.

8.1.1 Experimental prospects for studying small baths

Generally, the question of the effects of a small bath appears in any setting, where a localized system interacts with a second, thermal system of similar size. However, the answer to the effects of small baths can heavily depend on the exact setting. In our setup, a coupling between localized and extended states can be achieved in a variety of interesting settings.

Interaction coupling singe-particle localized and extended states: In this thesis, we have studied the effects of interactions only in the context of the AA-model, where the underlying single-particle system does not exhibit an SPME. However, adding interactions to our system at lower depths of the primary lattice, where an SPME is present, is straight-forward. In this setting, next-to-nearest-neighbor hopping terms are present and hence experimentally showing the existence of a full MBL phase, i.e. a regime where all many-body states are localized, is already a worthy goal. Note, though, that full MBL is only expected to occur far above the single-particle intermediate phase, where all single-particle states are already localized. Whether or not the intermediate phase survives in the presence of interactions, or on which timescale the interaction coupling delocalizes the single-particle localized states are very intriguing questions.

Limitations to studying the effects of small baths using an SPME appear due to the small width of the intermediate phase in our system: Interactions couple not only the single-particle extended to the single-particle localized states, but also localized to localized, as well as extended to extended states. In case of a slim intermediate phase, the interaction coupling between localized states could already be sufficient to delocalize all states and hence the coupling to single-particle extended states would not dramatically change the system's properties.

Coupling a localized ^{87}Rb system to a delocalized ^{40}K bath: A slightly cleaner option of studying the effects of small baths exists by loading a mixture of ^{40}K atoms and ^{87}Rb atoms into the quasi-periodic system. In this setting, the much heavier ^{87}Rb atoms would localize at a much smaller depth of the detuning lattice and therefore take the role of the localized system. By loading only one spin-species of ^{40}K, both the localized and the delocalized system would individually appear non-interacting, as the large background scattering length of ^{87}Rb will result in a fermionization of the bosons for sufficiently deep primary and orthogonal lattices. Via a Feshbach resonance, the interactions between the two species are tunable without making the individual systems interacting. Thus, a full (de)localization can only occur via a crosstalk between the two systems. Here, also a coexistence of the localized and the delocalized system is a possibility.

Using a superlattice to prepare and read-out a charge-density wave state of ^{87}Rb has been done before [104]. However, it is not clear whether or not the ^{40}K atoms will also form a CDW state in this case and whether a simultaneous read-out is possible. In the preparation of the initial state, it is important to remove doublons formed by ^{87}Rb atoms to achieve the fermionization. Technically, the most demanding requirement is the magnetic field stability required to address the Feshbach resonance, which is located at magnetic field strengths of $B \approx 550$ G but only $\delta B \approx 3$ G wide [119]. In our system, we can achieve long-term stable magnetic fields to an accuracy of $\sim \pm 5$ mG, which, at reasonable lattice depths, would correspond to an uncertainty of the interaction strength of $\delta U_{K-Rb} \approx \pm 1 J_{RB}$, where J_{RB} denotes the tunneling of the Rb atoms.

Interaction coupling different bands: A similar scenario as with a mixture of ^{40}K and ^{87}Rb atoms can also be achieved by loading atoms not only into the ground but also into the first excited band. In the first excited band, tunnel-couplings are much stronger than in the ground band, and hence it will localize only at much higher detuning strengths. If the two bands would be selectively populated by different spin-species of ^{40}K, this system would create the same Hamiltonian as above. Should both bands contain both spin-species, the system would realize a coupled many-body Hamiltonian to an interacting bath. In contrast to the scenario of using an SPME, however, in this case, the localization transitions of the two bands would be separated far enough to achieve MBL in the ground band while the first band is still localized. Note, however, that a controlled loading of atoms into the second band is non-trivial.

Currently, it is not clear which of the presented settings is best suited to gain insights into the aspects of small baths that are relevant for e.g. the existence of many-body mobility edges or the Griffiths mechanism. Each setting is, however, already interesting in its own right. I hope that at least some of these possibilities will indeed be experimentally realized in the near future and give insights that can, at least currently, not be obtained from small-scale numerics.

Details of the experimental sequence

Fig. A.1 gives the details of an exemplary sequence used to load atoms into the optical lattice, prepare the CDW initial state, initiate the time evolution and read out the imbalance. This sequence is subject to minor changes depending on the exact experiment. For example, the magnetic field during the loading of the lattice depends on the wanted doublon fraction. For the experiments with photon scattering, the additional scattering beam is switched on only during the evolution time.

The sequence used to measure the expansion of the cloud is similar and only differs after the time evolution, as the CDW state is always employed. In this case, the atoms' motion is frozen out by increasing the depth of the 532 nm and 1064 nm lattice as usual. Afterwards, however, the magnetic field is switched off as quickly as possible (~ 1 ms). Then all optical potentials are removed and the cloud is imaged in-situ. Note that this sequence can only be employed for imaging atoms in-situ if no doublons are present, as by switching off the magnetic field, the interactions ramp over the Feshbach resonance, thereby creating molecules. As these molecules do not absorb the imaging light, this would distort the images. In our case, this is not a problem, as all expansion measurements have been performed either with a spin-polarized mixture or with an initial state that suppresses the formation of doublons. Due to the low density in our system, we do not expect that a significant number of doublons is formed dynamically.
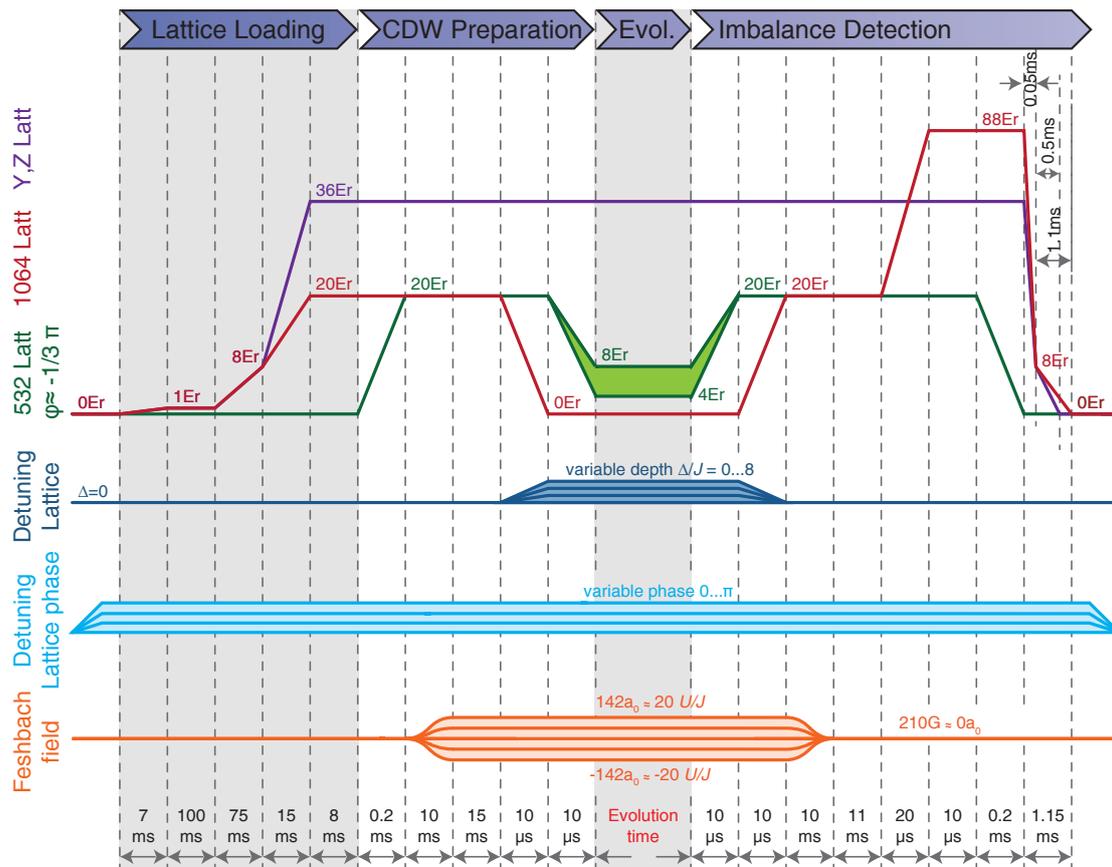
Figure A.1: Charge-density wave preparation and readout: Exemplary experimental sequence for the preparation and readout of the CDW state. The drawing is not to scale.

Implementation of the averaging over neighboring tubes in numerics

In chapter 3, we have explained the difference between the experimental results for the expansion and the numerical results by an averaging over many neighboring, one-dimensional systems, which is inherently present in the experiment. Due to the finite extent of the beams creating the optical lattices, these neighboring systems (tubes) experience slightly different lattice depths. Specifically, tubes on the outside of the cloud have lower lattice depths than those in the center.

Considering this effect in the numerics is performed by simulating the system with various multipliers for the lattice depths V_p and V_d, and then averaging these results with weights based on the number of atoms subjected to the corresponding lattice depth multiplier. The used multipliers are given with the respective relative weights in Fig. B.1. The values are calculated from the Gaussian widths of the lattice beams of $150\,\mu$m, as well as the extent of the atom cloud in the optical lattice in the orthogonal directions of $42\,\mu$m horizontally and $12\,\mu$m vertically. Note that this effect is only considered in the single-particle case. In the presence of interactions, the additional numerical effort would be unjustified, as the imbalance is influenced much less than the expansion. Also, additional effects like e.g. the decreasing density and the increasing entropy on the edges of the cloud would need to be considered.
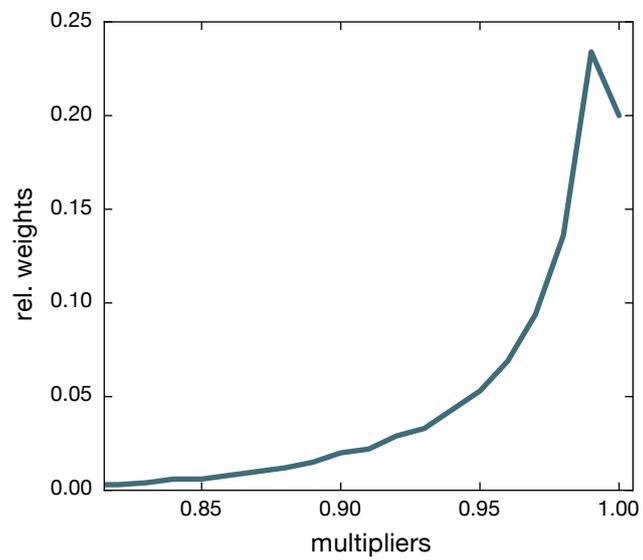
Figure B.1: Averaging over tubes: Used multipliers and their respective weights. The multiplier of '1' corresponds to the central tube.

Bibliography

[1] P. W. Anderson. *Basic notions of condensed matter physics*. Benjamin-Cummings (1984). Cited on page: 1

[2] P. Kapitza. *Viscosity of liquid helium below the λ-point*. Nature **141**, 74 (1938). Cited on page: 1

[3] J. F. Allen and A. D. Misener. *Flow of liquid helium II*. Nature **141**, 75 (1938). Cited on page: 1

[4] H. K. Onnes. *The resistance of pure mercury at helium temperatures*. Commun. Phys. Lab. Univ. Leiden **12**, 1 (1911). Cited on page: 1

[5] J. Bardeen, L. N. Cooper, and J. R. Schrieffer. *Theory of Superconductivity*. Phys. Rev. **108**, 1175–1204 (1957). Cited on page: 1

[6] M. Greiner, O. Mandel, T. Esslinger, T. W. Hänsch, and I. Bloch. *Quantum phase transition from a superfluid to a Mott insulator in a gas of ultracold atoms*. Nature **415**, 39–44 (2002). Cited on pages: 1, 3

[7] P. C. Hohenberg. *Existence of Long-Range Order in One and Two Dimensions*. Phys. Rev. **158**, 383–386 (1967). Cited on page: 1

[8] N. D. Mermin and H. Wagner. *Absence of Ferromagnetism or Antiferromagnetism in One- or Two-Dimensional Isotropic Heisenberg Models*. Phys. Rev. Lett. **17**, 1133–1136 (1966).

[9] S. Coleman. *There are no Goldstone bosons in two dimensions*. Commun. Math. Phys. **31**, 259–264 (1973). Cited on page: 1

[10] K. Sengupta, S. Powell, and S. Sachdev. *Quench dynamics across quantum critical points*. Phys. Rev. A **69**, 053616 (2004). Cited on page: 1

[11] J. Berges, S. Borsányi, and C. Wetterich. *Prethermalization*. Phys. Rev. Lett. **93**, 142002 (2004).

[12] M. Rigol, V. Dunjko, and M. Olshanii. *Thermalization and its mechanism for generic isolated quantum systems*. Nature **452**, 854–858 (2008). Cited on pages: 1, 43, 46, 47

[13] J. Lux, J. Müller, A. Mitra, and A. Rosch. *Hydrodynamic long-time tails after a quantum quench*. Phys. Rev. A **89**, 053608 (2014). Cited on pages: 1, 21

[14] G. Gallavotti. *Statistical mechanics: A short treatise*. Springer Science & Business Media (2013). Cited on page: 1

[15] N. S. Krylov. *Works on the foundations of statistical physics*. Princeton University Press (2014). Cited on pages: 1, 45

[16] J. M. Deutsch. *Quantum statistical mechanics in a closed system*. Phys. Rev. A **43**, 2046–2049 (1991). Cited on pages: 1, 43, 45, 47

[17] M. Srednicki. *Chaos and quantum thermalization*. Phys. Rev. E **50**, 888–901 (1994). Cited on pages: 1, 43, 47

[18] T. Kinoshita, T. Wenger, and D. S. Weiss. *A quantum Newton's cradle*. Nature **440**, 900–903 (2006). Cited on pages: 2, 3

[19] P. W. Anderson. *Absence of Diffusion in Certain Random Lattices*. Phys. Rev. **109**, 1492–1505 (1958). Cited on pages: 2, 9, 15, 19

[20] E. Abrahams, P. W. Anderson, D. C. Licciardello, and T. V. Ramakrishnan. *Scaling Theory of Localization: Absence of Quantum Diffusion in Two Dimensions*. Phys. Rev. Lett. **42**, 673–676 (1979). Cited on pages: 28, 38

[21] J. Billy, V. Josse, Z. Zuo, A. Bernard, B. Hambrecht, P. Lugan, D. Clément, L. Sanchez-Palencia, P. Bouyer, and A. Aspect. *Direct observation of Anderson localization of matter waves in a controlled disorder*. Nature **453**, 891–894 (2008). Cited on pages: 2, 3, 15, 19, 20, 24, 25, 38

[22] D. M. Basko, I. L. Aleiner, and B. L. Altshuler. *Metal-insulator transition in a weakly interacting many-electron system with localized single-particle states*. Ann. Phys. **321**, 1126–1205 (2006). Cited on pages: 2, 49

[23] V. Oganesyan and D. A. Huse. *Localization of interacting fermions at high temperature*. Phys. Rev. B **75**, 155111 (2007). Cited on page: 50

[24] J. Z. Imbrie. *On Many-Body Localization for Quantum Spin Chains*. J. Stat. Phys. **163**, 998–1048 (2016). Cited on pages: 2, 49

[25] M. Serbyn, Z. Papić, and D. A. Abanin. *Local Conservation Laws and the Structure of the Many-Body Localized state*. Phys. Rev. Lett. **111**, 127201 (2013). Cited on pages: 2, 50

[26] D. A. Huse, R. Nandkishore, and V. Oganesyan. *Phenomenology of fully many-body-localized systems*. Phys. Rev. B **90**, 174202 (2014). Cited on page: 50

[27] J. Z. Imbrie, V. Ros, and A. Scardicchio. *Local integrals of motion in many-body localized systems*. Ann. Phys. **529**, 1600278 (2017). Cited on pages: 2, 50, 51

[28] D. A. Huse, R. Nandkishore, V. Oganesyan, A. Pal, and S. L. Sondhi. *Localization-protected quantum order*. Phys. Rev. B **88**, 014206 (2013). Cited on pages: 2, 69

[29] B. Bauer and C. Nayak. *Area laws in a many-body localized state and its implications for topological order*. J. Stat. Mech. **2013**, P09005 (2013). Cited on pages: 50, 51

[30] Y. Bahri, R. Vosk, E. Altman, and A. Vishwanath. *Localization and topology protected quantum coherence at the edge of hot matter*. Nat. Commun. **6**, 7341 (2015).

[31] A. Chandran, V. Khemani, C. R. Laumann, and S. L. Sondhi. *Many-body localization and symmetry-protected topological order*. Phys. Rev. B **89**, 144201 (2014).

[32] R. Vosk and E. Altman. *Dynamical Quantum Phase Transitions in Random Spin Chains*. Phys. Rev. Lett. **112**, 217204 (2014).

[33] D. Pekker, G. Refael, E. Altman, E. Demler, and V. Oganesyan. *Hilbert-Glass Transition: New Universality of Temperature-Tuned Many-Body Dynamical Quantum Criticality*. Phys. Rev. X **4**, 011052 (2014). Cited on pages: 2, 69

[34] R. Nandkishore and D. A. Huse. *Many-Body Localization and Thermalization in Quantum Statistical Mechanics*. Annu. Rev. Condens. Matter Phys. **6**, 15–38 (2015). Cited on page: 2

[35] E. Altman and R. Vosk. *Universal Dynamics and Renormalization in Many-Body-Localized Systems*. Annu. Rev. Condens. Matter Phys. **6**, 383–409 (2015). Cited on page: 2

[36] S. A. Parameswaran, A. C. Potter, and R. Vasseur. *Eigenstate phase transitions and the emergence of universal dynamics in highly excited states*. Ann. Phys. **529**, 1600302 (2017). Cited on pages: 2, 69

[37] D. J. Luitz and Y. B. Lev. *The ergodic side of the many-body localization transition*. Ann. Phys. **529**, 1600350 (2017). Cited on page: 52

[38] K. Agarwal, E. Altman, E. Demler, S. Gopalakrishnan, D. A. Huse, and M. Knap. *Rare-region effects and dynamics near the many-body localization transition*. Ann. Phys. **529**, 1600326 (2017). Cited on pages: 2, 69, 115

[39] R. Vosk, D. A. Huse, and E. Altman. *Theory of the Many-Body Localization Transition in One-Dimensional Systems*. Phys. Rev. X **5**, 031032 (2015). Cited on pages: 2, 69, 70, 71

[40] A. C. Potter, R. Vasseur, and S. A. Parameswaran. *Universal Properties of Many-Body Delocalization Transitions*. Phys. Rev. X **5**, 031033 (2015). Cited on pages: 69, 70, 71

[41] V. Khemani, D. N. Sheng, and D. A. Huse. *Two Universality Classes for the Many-Body Localization Transition*. Phys. Rev. Lett. **119**, 075702 (2017). Cited on pages: 2, 10, 73, 83

[42] S. Iyer, V. Oganesyan, G. Refael, and D. A. Huse. *Many-body localization in a quasiperiodic system*. Phys. Rev. B **87**, 134202 (2013). Cited on page: 2

[43] M. Schreiber, S. S. Hodgman, P. Bordia, H. P. Lüschen, M. H. Fischer, R. Vosk, E. Altman, U. Schneider, and I. Bloch. *Observation of many-body localization of interacting fermions in a quasirandom optical lattice*. Science **349**, 842–845 (2015). Cited on pages: 3, 5, 16, 29, 39, 52, 61, 62, 63, 64, 65, 81

[44] V. Mastropietro. *Localization of Interacting Fermions in the Aubry-André Model*. Phys. Rev. Lett. **115**, 180401 (2015). Cited on page: 2

[45] M. Y. Azbel. *Quantum Particle in One-Dimensional Potentials with Incommensurate Periods*. Phys. Rev. Lett. **43**, 1954–1957 (1979). Cited on page: 2

[46] S. Aubry and G. André. *Analyticity breaking and Anderson localization in incommensurate lattices*. Ann. Israel Phys. Soc. **3** (1980). Cited on pages: 9, 15, 16, 36, 38

[47] G. Roati, C. D'Errico, L. Fallani, M. Fattori, C. Fort, M. Zaccanti, G. Modugno, M. Modugno, and M. Inguscio. *Anderson localization of a non-interacting Bose-Einstein condensate*. Nature **453**, 895–898 (2008). Cited on pages: 2, 3, 4, 13, 16, 24, 25

[48] V. Khemani, S. P. Lim, D. N. Sheng, and D. A. Huse. *Critical Properties of the Many-Body Localization Transition*. Phys. Rev. X **7**, 021013 (2017). Cited on pages: 2, 71, 72, 73

[49] S. Das Sarma, S. He, and X. C. Xie. *Mobility Edge in a Model One-Dimensional Potential*. Phys. Rev. Lett. **61**, 2144–2147 (1988). Cited on pages: 2, 28, 38

[50] D. J. Boers, B. Goedeke, D. Hinrichs, and M. Holthaus. *Mobility edges in bichromatic optical lattices*. Phys. Rev. A **75**, 063404 (2007). Cited on pages: 2, 28

[51] X. Li, S. Ganeshan, J. H. Pixley, and S. Das Sarma. *Many-Body Localization and Quantum Nonergodicity in a Model with a Single-Particle Mobility Edge*. Phys. Rev. Lett. **115**, 186601 (2015). Cited on pages: 2, 111, 115

[52] R. Modak and S. Mukerjee. *Many-Body Localization in the Presence of a Single-Particle Mobility Edge*. Phys. Rev. Lett. **115**, 230401 (2015). Cited on pages: 111, 115

[53] D.-L. Deng, S. Ganeshan, X. Li, R. Modak, S. Mukerjee, and J. H. Pixley. *Many-body localization in incommensurate models with a mobility edge*. Ann. Phys. **529**, 1600399 (2017). Cited on pages: 2, 115

[54] D. S. Wiersma, P. Bartolini, A. Lagendijk, and R. Righini. *Localization of light in a disordered medium*. Nature **390**, 671–673 (1997). Cited on pages: 3, 20

[55] Y. Lahini, R. Pugatch, F. Pozzi, M. Sorel, R. Morandotti, N. Davidson, and Y. Silberberg. *Observation of a Localization Transition in Quasiperiodic Photonic Lattices*. Phys. Rev. Lett. **103**, 013901 (2009). Cited on page: 16

[56] T. Schwartz, G. Bartal, S. Fishman, and M. Segev. *Transport and Anderson localization in disordered two-dimensional photonic lattices*. Nature **446**, 52–55 (2007). Cited on page: 3

[57] S. S. Kondov, W. R. McGehee, J. J. Zirbel, and B. DeMarco. *Three-Dimensional Anderson Localization of Ultracold Matter*. Science **334**, 66–68 (2011). Cited on pages: 3, 15, 24

[58] F. Jendrzejewski, A. Bernard, K. Müller, P. Cheinet, V. Josse, M. Piraud, L. Pezze, L. Sanchez-Palencia, A. Aspect, and P. Bouyer. *Three-dimensional localization of ultracold atoms in an optical disordered potential*. Nat. Phys. **8**, 398–403 (2012). Cited on pages: 3, 15, 28, 38

[59] B. Deissler, M. Zaccanti, G. Roati, C. D'Errico, M. Fattori, M. Modugno, G. Modugno, and M. Inguscio. *Delocalization of a disordered bosonic system by repulsive interactions*. Nat. Phys. **6**, 354–358 (2010). Cited on page: 3

[60] B. Gadway, D. Pertot, J. Reeves, M. Vogt, and D. Schneble. *Glassy Behavior in a Binary Atomic Mixture*. Phys. Rev. Lett. **107**, 145306 (2011).

[61] C. D'Errico, E. Lucioni, L. Tanzi, L. Gori, G. Roux, I. P. McCulloch, T. Giamarchi, M. Inguscio, and G. Modugno. *Observation of a Disordered Bosonic Insulator from Weak to Strong Interactions*. Phys. Rev. Lett. **113**, 095301 (2014). Cited on page: 24

[62] S. S. Kondov, W. R. McGehee, W. Xu, and B. DeMarco. *Disorder-Induced Localization in a Strongly Correlated Atomic Hubbard Gas*. Phys. Rev. Lett. **114**, 083002 (2015). Cited on pages: 3, 15

[63] M. Ovadia, D. Kalok, I. Tamir, S. Mitra, B. Sacépé, and D. Shahar. *Evidence for a Finite-Temperature Insulator*. Sci. Rep. **5**, 13503 (2015). Article. Cited on page: 3

[64] J.-y. Choi, S. Hild, J. Zeiher, P. Schauß, A. Rubio-Abadal, T. Yefsah, V. Khemani, D. A. Huse, I. Bloch, and C. Gross. *Exploring the many-body localization transition in two dimensions*. Science **352**, 1547–1552 (2016). Cited on pages: 3, 20, 24, 115

[65] J. Smith, A. Lee, P. Richerme, B. Neyenhuis, P. W. Hess, P. Hauke, M. Heyl, D. A. Huse, and C. Monroe. *Many-body localization in a quantum simulator with programmable random disorder*. Nat. Phys. **12**, 907–911 (2016). Letter. Cited on page: 3

[66] G. Kucsko, S. Choi, J. Choi, P. C. Maurer, H. Sumiya, S. Onoda, J. Isoya, F. Jelezko, E. Demler, N. Y. Yao, and M. D. Lukin. *Critical thermalization of a disordered dipolar spin system in diamond*. arXiv:1609.08216 (2016). Cited on pages: 3, 15

[67] K. X. Wei, C. Ramanathan, and P. Cappellaro. *Exploring Localization in Nuclear Spin Chains*. arXiv:1612.05249 (2016). Cited on page: 3

[68] P. Roushan, C. Neill, J. Tangpanitanon, V. M. Bastidas, A. Megrant, R. Barends, Y. Chen, Z. Chen, B. Chiaro, A. Dunsworth, A. Fowler, B. Foxen, M. Giustina, E. Jeffrey, J. Kelly, E. Lucero, J. Mutus, M. Neeley, C. Quintana, D. Sank, A. Vainsencher, J. Wenner, T. White, H. Neven, D. G. Angelakis, and J. Martinis. *Spectral signatures of many-body localization with interacting photons*. arXiv:1709.07108 (2017). Cited on page: 3

[69] P. Bordia, H. P. Lüschen, S. S. Hodgman, M. Schreiber, I. Bloch, and U. Schneider. *Coupling Identical one-dimensional Many-Body Localized Systems*. Phys. Rev. Lett. **116**, 140401 (2016). Cited on pages: 3, 5, 29, 30, 57, 62, 75, 82, 83, 89, 90, 91, 115

[70] H. P. Lüschen, P. Bordia, S. S. Hodgman, M. Schreiber, S. Sarkar, A. J. Daley, M. H. Fischer, E. Altman, I. Bloch, and U. Schneider. *Signatures of Many-Body Localization in a Controlled Open Quantum System*. Phys. Rev. X **7**, 011034 (2017). Cited on pages: 3, 5, 55, 57, 62, 82, 83, 98, 99, 105, 108, 110

[71] B. Nowak, J. J. Kinnunen, M. J. Holland, and P. Schlagheck. *Delocalization of ultracold atoms in a disordered potential due to light scattering*. Phys. Rev. A **86**, 043610 (2012). Cited on page: 3

[72] R. Nandkishore and S. Gopalakrishnan. *Many body localized systems weakly coupled to baths*. Ann. Phys. (2016). Cited on pages: 3, 89, 115

[73] S. Sachdev. *Quantum Phase Transitions*. Cambridge University press (2001). Cited on pages: 3, 68, 69

[74] N. F. Mott. *Conduction in non-crystalline systems*. Philos. Mag. **17**, 1259–1268 (1968). Cited on page: 3

[75] D. A. Huse, R. Nandkishore, F. Pietracaprina, V. Ros, and A. Scardicchio. *Localized systems coupled to small baths: From Anderson to Zeno*. Phys. Rev. B **92**, 014203 (2015). Cited on pages: 3, 89, 115

[76] K. Hyatt, J. R. Garrison, A. C. Potter, and B. Bauer. *Many-body localization in the presence of a small bath*. Phys. Rev. B **95**, 035132 (2017). Cited on pages: 3, 111, 115

[77] W. De Roeck and F. Huveneers. *Stability and instability towards delocalization in many-body localization systems*. Phys. Rev. B **95**, 155129 (2017). Cited on page: 3

[78] S. Inglis and L. Pollet. *Accessing Many-Body Localized States through the Generalized Gibbs Ensemble*. Phys. Rev. Lett. **117**, 120402 (2016). Cited on page: 3

[79] I. Mondragon-Shem, A. Pal, T. L. Hughes, and C. R. Laumann. *Many-body mobility edge due to symmetry-constrained dynamics and strong interactions*. Phys. Rev. B **92**, 064203 (2015). Cited on page: 3

[80] W. De Roeck, F. Huveneers, M. Müller, and M. Schiulaz. *Absence of many-body mobility edges*. Phys. Rev. B **93**, 014203 (2016). Cited on pages: 3, 115

[81] I. Bloch, J. Dalibard, and W. Zwerger. *Many-body physics with ultracold gases*. Rev. Mod. Phys. **80**, 885–964 (2008). Cited on page: 3

[82] I. Bloch, J. Dalibard, and S. Nascimbene. *Quantum simulations with ultracold quantum gases*. Nat. Phys. **8**, 267–276 (2012). Cited on page: 3

[83] R. P. Feynman. *Simulating physics with computers*. Int. J. Theor. Phys. **21**, 467–488 (1982). Cited on page: 3

[84] M. H. Anderson, J. R. Ensher, M. R. Matthews, C. E. Wieman, and E. A. Cornell. *Observation of Bose-Einstein condensation in a dilute atomic vapor*. Science **269**, 198 (1995). Cited on pages: 3, 10

[85] C. C. Bradley, C. A. Sackett, J. J. Tollett, and R. G. Hulet. *Evidence of Bose-Einstein Condensation in an Atomic Gas with Attractive Interactions*. Phys. Rev. Lett. **75**, 1687–1690 (1995).

[86] K. B. Davis, M. O. Mewes, M. R. Andrews, N. J. van Druten, D. S. Durfee, D. M. Kurn, and W. Ketterle. *Bose-Einstein Condensation in a Gas of Sodium Atoms*. Phys. Rev. Lett. **75**, 3969–3973 (1995). Cited on page: 3

[87] B. DeMarco and D. S. Jin. *Onset of Fermi Degeneracy in a Trapped Atomic Gas*. Science **285**, 1703–1706 (1999). Cited on page: 3

[88] F. Schreck, L. Khaykovich, K. L. Corwin, G. Ferrari, T. Bourdel, J. Cubizolles, and C. Salomon. *Quasipure Bose-Einstein Condensate Immersed in a Fermi Sea*. Phys. Rev. Lett. **87**, 080403 (2001).

[89] A. G. Truscott, K. E. Strecker, W. I. McAlexander, G. B. Partridge, and R. G. Hulet. *Observation of Fermi Pressure in a Gas of Trapped Atoms*. Science **291**, 2570–2572 (2001). Cited on pages: 3, 10

[90] D. Jaksch, C. Bruder, J. I. Cirac, C. W. Gardiner, and P. Zoller. *Cold Bosonic Atoms in Optical Lattices*. Phys. Rev. Lett. **81**, 3108–3111 (1998). Cited on pages: 3, 17

[91] J. Hubbard. *Electron Correlations in Narrow Energy Bands*. Proc. Royal Soc. A **276**, 238–257 (1963). Cited on pages: 3, 15, 19, 49, 60

[92] J. Sebby-Strabley, M. Anderlini, P. S. Jessen, and J. V. Porto. *Lattice of double wells for manipulating pairs of cold atoms*. Phys. Rev. A **73**, 033605 (2006). Cited on page: 3

[93] C. Becker, P. Soltan-Panahi, J. Kronjäger, S. Dörscher, K. Bongs, and K. Sengstock. *Ultracold quantum gases in triangular optical lattices*. New J. Phys. **12**, 065025 (2010).

[94] L. Tarruell, D. Greif, T. Uehlinger, G. Jotzu, and T. Esslinger. *Creating, moving and merging Dirac points with a Fermi gas in a tunable honeycomb lattice*. Nature **483**, 302–305 (2012).

[95] G.-B. Jo, J. Guzman, C. K. Thomas, P. Hosur, A. Vishwanath, and D. M. Stamper-Kurn. *Ultracold Atoms in a Tunable Optical Kagome Lattice*. Phys. Rev. Lett. **108**, 045305 (2012).

[96] D. Jaksch and P. Zoller. *The cold atom Hubbard toolbox*. Ann. Phys. **315**, 52 – 79 (2005). Cited on page: 3

[97] D. Jaksch and P. Zoller. *Creation of effective magnetic fields in optical lattices: the Hofstadter butterfly for cold neutral atoms*. New J. Phys. **5**, 56 (2003). Cited on page: 3

[98] M. Aidelsburger, M. Atala, S. Nascimbène, S. Trotzky, Y.-A. Chen, and I. Bloch. *Experimental Realization of Strong Effective Magnetic Fields in an Optical Lattice*. Phys. Rev. Lett. **107**, 255301 (2011). Cited on page: 3

[99] C. Chin, R. Grimm, P. Julienne, and E. Tiesinga. *Feshbach resonances in ultracold gases*. Rev. Mod. Phys. **82**, 1225–1286 (2010). Cited on page: 3

[100] C. A. Regal, C. Ticknor, J. L. Bohn, and D. S. Jin. *Creation of ultracold molecules from a Fermi gas of atoms*. Nature **424**, 47–50 (2003). Cited on pages: 3, 11, 57, 59, 95

[101] C. Weitenberg, M. Endres, J. F. Sherson, M. Cheneau, P. Schausz, T. Fukuhara, I. Bloch, and S. Kuhr. *Single-spin addressing in an atomic Mott insulator*. Nature **471**, 319–324 (2011). Cited on page: 3

[102] R. Jördens, N. Strohmaier, K. Günter, H. Moritz, and T. Esslinger. *A Mott insulator of fermionic atoms in an optical lattice*. Nature **455**, 204–207 (2008). Cited on page: 3

[103] U. Schneider, L. Hackermüller, S. Will, T. Best, I. Bloch, T. A. Costi, R. W. Helmes, D. Rasch, and A. Rosch. *Metallic and Insulating Phases of Repulsively Interacting Fermions in a 3D Optical Lattice*. Science **322**, 1520–1525 (2008). Cited on page: 3

[104] S. Trotzky, Y.-A. Chen, A. Flesch, I. P. McCulloch, U. Schollwock, J. Eisert, and I. Bloch. *Probing the relaxation towards equilibrium in an isolated strongly correlated one-dimensional Bose gas*. Nat. Phys. **8**, 325–330 (2012). Cited on pages: 3, 23, 116

[105] U. Schneider, L. Hackermuller, J. P. Ronzheimer, S. Will, S. Braun, T. Best, I. Bloch, E. Demler, S. Mandt, D. Rasch, and A. Rosch. *Fermionic transport and out-of-equilibrium dynamics in a homogeneous Hubbard model with ultracold atoms*. Nat. Phys. **8**, 213–218 (2012). Cited on pages: 24, 31, 59, 62

[106] D. Pertot, A. Sheikhan, E. Cocchi, L. A. Miller, J. E. Bohn, M. Koschorreck, M. Köhl, and C. Kollath. *Relaxation Dynamics of a Fermi Gas in an Optical Superlattice*. Phys. Rev. Lett. **113**, 170403 (2014). Cited on page: 3

[107] M. Müller, S. Diehl, G. Pupillo, and P. Zoller. *Engineered Open Systems and Quantum Simulations with Atoms and Ions*. Adv. At. Mol. Opt. Phys. **61**, 1 – 80 (2012). Cited on pages: 4, 90

[108] H. P. Lüschen, P. Bordia, S. Scherg, F. Alet, E. Altman, U. Schneider, and I. Bloch. *Observation of Slow Dynamics near the Many-Body Localization Transition in One-Dimensional Quasiperiodic Systems*. Phys. Rev. Lett. **119**, 260401 (2017). Cited on pages: 5, 55, 77, 79

[109] L. et. al. *Exploring Single-Particle Mobility Edges in a Quasiperiodic Optical LAttice*. In preparation (2017). Cited on pages: 5, 33, 35

[110] P. Bordia, H. Lüschen, U. Schneider, M. Knap, and I. Bloch. *Periodically driving a many-body localized quantum system*. Nat. Phys. **13**, 460–464 (2017). Cited on pages: 5, 81, 89

[111] P. Bordia, H. Lüschen, S. Scherg, S. Gopalakrishnan, M. Knap, U. Schneider, and I. Bloch. *Probing Slow Relaxation and Many-Body Localization in Two-Dimensional Quasiperiodic Systems*. Phys. Rev. X **7**, 041047 (2017). Cited on pages: 5, 15

[112] J. P. Ronzheimer. *Non-equilibrium dynamics of ultracold atoms in optical lattices*. PhD thesis, Faculty of Physics, Ludwig-Maximilians-Universität, Munich (2014). Cited on pages: 10, 12, 26, 31

[113] S. Braun. *Negative absolut temperature and the dynamics of quantum phase transitions*. PhD thesis, Faculty of Physics, Ludwig-Maximilians-Universität, Munich (2014).

[114] M. Schreiber. *Observation of Many-Body Localization in One-Dimensions in Quasi-Periodic Optical Lattices*. PhD thesis, Faculty of Physics, Ludwig-Maximilians-Universität, Munich (in preparation). Cited on pages: 12, 28, 63, 114

[115] P. Bordia. *Probing Many-Body Localization with Ultracold Atoms in Optical Lattices*. PhD thesis, Faculty of Physics, Ludwig-Maximilians-Universität, Munich (2017). Cited on pages: 10, 89, 90, 114

[116] R. Grimm, M. Weidemüller, and Y. B. Ovchinnikov. *Optical dipole traps for neutral atoms*. Adv. At. Mol. Opt. Phys. **42**, 95–170 (2000). Cited on page: 11

[117] T. G. Tiecke. *Properties of Potassium*. PhD thesis, University of Amsterdam, The Netherlands (2011). Cited on pages: 11, 95

[118] H. Feshbach. *A unified theory of nuclear reactions. II*. Ann. Phys. **19**, 287–313 (1962). Cited on page: 11

[119] C. Klempt, T. Henninger, O. Topic, J. Will, W. Ertmer, E. Tiemann, and J. Arlt. ^{40}K$-^{87}$Rb *Feshbach resonances: Modeling the interatomic potential*. Phys. Rev. A **76**, 020701 (2007). Cited on pages: 11, 116

[120] U. Schneider. *Interacting Fermionic Atoms in Optical Lattices - A Quantum Simulator for Condensed Matter Physics*. PhD thesis, Faculty of Physics, Johannes Gutenberg-Universität, Mainz (2010). Cited on pages: 12, 31

[121] D. Garbe. *Bichromatic Superlattice for Ultracold fermi-Gases*. PhD thesis, Faculty of Physics, Ludwig-Maximilians-Universität, Munich (2012). Cited on page: 14

[122] F. Görg. *Ultracold Fermionic Atoms in Optical Superlattices*. PhD thesis, Faculty of Physics, Ludwig-Maximilians-Universität, Munich (2014). Cited on pages: 14, 23

[123] M. Wilkinson. *Critical Properties of Electron Eigenstates in Incommensurate Systems*. Proc. Royal Soc. A **391**, 305–350 (1984). Cited on page: 14

[124] L. Fallani, J. E. Lye, V. Guarrera, C. Fort, and M. Inguscio. *Ultracold Atoms in a Disordered Crystal of Light: Towards a Bose Glass*. Phys. Rev. Lett. **98**, 130404 (2007). Cited on page: 14

[125] W. R. McGehee, S. S. Kondov, W. Xu, J. J. Zirbel, and B. DeMarco. *Three-Dimensional Anderson Localization in Variable Scale Disorder*. Phys. Rev. Lett. **111**, 145303 (2013). Cited on pages: 15, 24, 28, 38

[126] G. Semeghini, M. Landini, P. Castilho, S. Roy, G. Spagnolli, A. Trenkwalder, M. Fattori, M. Inguscio, and G. Modugno. *Measurement of the mobility edge for 3D Anderson localization*. Nat. Phys. **11**, 554–559 (2015). Cited on pages: 15, 24, 28, 38

[127] M. Modugno. *Exponential localization in one-dimensional quasi-periodic optical lattices*. New J. Phys. **11**, 033023 (2009). Cited on page: 17

[128] N. W. Ashcroft and N. D. Mermin. *Solid State Physics*. Saunders College, Philadelphia (1976). Cited on page: 17

[129] N. Marzari, A. A. Mostofi, J. R. Yates, I. Souza, and D. Vanderbilt. *Maximally localized Wannier functions: Theory and applications*. Rev. Mod. Phys. **84**, 1419–1475 (2012). Cited on page: 17

[130] V. Guarrera, L. Fallani, J. E. Lye, C. Fort, and M. Inguscio. *Inhomogeneous broadening of a Mott insulator spectrum*. New J. Phys. **9**, 107 (2007). Cited on page: 17

[131] G. Roux, T. Barthel, I. P. McCulloch, C. Kollath, U. Schollwöck, and T. Giamarchi. *Quasiperiodic Bose-Hubbard model and localization in one-dimensional cold atomic gases*. Phys. Rev. A **78**, 023628 (2008). Cited on page: 17

[132] M. Störzer, P. Gross, C. M. Aegerter, and G. Maret. *Observation of the Critical Regime Near Anderson Localization of Light*. Phys. Rev. Lett. **96**, 063904 (2006). Cited on page: 20

[133] J. P. Ronzheimer, M. Schreiber, S. Braun, S. S. Hodgman, S. Langer, I. P. McCulloch, F. Heidrich-Meisner, I. Bloch, and U. Schneider. *Expansion Dynamics of Interacting Bosons in Homogeneous Lattices in One and Two Dimensions*. Phys. Rev. Lett. **110**, 205301 (2013). Cited on pages: 24, 31, 59

[134] L. Vidmar, J. P. Ronzheimer, M. Schreiber, S. Braun, S. S. Hodgman, S. Langer, F. Heidrich-Meisner, I. Bloch, and U. Schneider. *Dynamical Quasicondensation of Hard-Core Bosons at Finite Momenta*. Phys. Rev. Lett. **115**, 175301 (2015).

[135] L. Xia, L. A. Zundel, J. Carrasquilla, A. Reinhard, J. M. Wilson, M. Rigol, and D. S. Weiss. *Quantum distillation and confinement of vacancies in a doublon sea*. Nat. Phys. **11**, 316–320 (2015). Letter. Cited on page: 24

[136] E. Lucioni, B. Deissler, L. Tanzi, G. Roati, M. Zaccanti, M. Modugno, M. Larcher, F. Dalfovo, M. Inguscio, and G. Modugno. *Observation of Subdiffusion in a Disordered Interacting System*. Phys. Rev. Lett. **106**, 230403 (2011). Cited on pages: 25, 84

[137] N. Mott. *On metal-insulator transitions*. J. Solid State Chem. **88**, 5 – 7 (1990). Cited on page: 27

[138] S. Das Sarma, A. Kobayashi, and R. E. Prange. *Proposed Experimental Realization of Anderson Localization in Random and Incommensurate Artificially Layered Systems*. Phys. Rev. Lett. **56**, 1280–1283 (1986). Cited on pages: 28, 38

[139] D. J. Thouless. *Localization by a Potential with Slowly Varying Period*. Phys. Rev. Lett. **61**, 2141–2143 (1988).

[140] S. Das Sarma, S. He, and X. C. Xie. *Localization, mobility edges, and metal-insulator transition in a class of one-dimensional slowly varying deterministic potentials*. Phys. Rev. B **41**, 5544–5565 (1990).

[141] J. Biddle and S. Das Sarma. *Predicted Mobility Edges in One-Dimensional Incommensurate Optical Lattices: An Exactly Solvable Model of Anderson Localization*. Phys. Rev. Lett. **104**, 070601 (2010).

[142] J. Biddle, D. J. Priour, B. Wang, and S. Das Sarma. *Localization in one-dimensional lattices with non-nearest-neighbor hopping: Generalized Anderson and Aubry-André models*. Phys. Rev. B **83**, 075105 (2011).

[143] S. Ganeshan, J. H. Pixley, and S. Das Sarma. *Nearest Neighbor Tight Binding Models with an Exact Mobility Edge in One Dimension*. Phys. Rev. Lett. **114**, 146601 (2015). Cited on pages: 28, 38

[144] P. A. Lee and T. V. Ramakrishnan. *Disordered electronic systems*. Rev. Mod. Phys. **57**, 287–337 (1985). Cited on pages: 28, 38

[145] M. Pasek, G. Orso, and D. Delande. *Anderson Localization of Ultracold Atoms: Where is the Mobility Edge?* Phys. Rev. Lett. **118**, 170403 (2017). Cited on page: 28

[146] X. Li, X. Li, and S. Das Sarma. *Mobility edges in one-dimensional bichromatic incommensurate potentials*. Phys. Rev. B **96**, 085119 (2017). Cited on pages: 28, 36, 115

[147] G. Wang, N. Li, and T. Nakayama. *Appearance of Mobility Edge in Self-Dual Quasiperiodic Lattices*. arXiv:1312.0844 (2013). Cited on page: 38

[148] L. D. Landau and E. M. Lifshitz. *Statistical physics*, Volume 5. Elsevier, Oxford, 3rd edition (1980). Cited on page: 43

[149] E. Fermi, J. R. Pasta, S. Ulam, and M. Tsingou. *Studies of nonlinear problems*. Los Alamos Internal Report LA-1940 (1995). Cited on page: 44

[150] G. P. Berman and F. M. Izrailev. *The Fermi–Pasta–Ulam problem: Fifty years of progress*. Chaos **15**, 015104 (2005). Cited on page: 44

[151] J. P. Eckmann and D. Ruelle. *Ergodic theory of chaos and strange attractors*. Rev. Mod. Phys. **57**, 617–656 (1985). Cited on page: 44

[152] F. Jin, T. Neuhaus, K. Michielsen, S. Miyashita, M. A. Novotny, M. I. Katsnelson, and H. D. Raedt. *Equilibration and thermalization of classical systems*. New J. Phys. **15**, 033009 (2013). Cited on page: 44

[153] J. v. Neumann. *Beweis des Ergodensatzes und desH-Theorems in der neuen Mechanik*. Z. Phys. **57**, 30–70 (1929). Cited on page: 45

[154] A. Peres. *Ergodicity and mixing in quantum theory. I*. Phys. Rev. A **30**, 504–508 (1984). Cited on page: 45

[155] J. R. Garrison and T. Grover. *Does a single eigenstate encode the full Hamiltonian?* arXiv:1503.00729 (2015). Cited on pages: 47, 48

[156] J.-S. Caux and J. Mossel. *Remarks on the notion of quantum integrability*. J. Stat. Mech. **2011**, P02023 (2011). Cited on page: 48

[157] M. Rigol, V. Dunjko, V. Yurovsky, and M. Olshanii. *Relaxation in a Completely Integrable Many-Body Quantum System: An Ab Initio Study of the Dynamics of the Highly Excited States of 1D Lattice Hard-Core Bosons*. Phys. Rev. Lett. **98**, 050405 (2007). Cited on page: 49

[158] A. C. Cassidy, C. W. Clark, and M. Rigol. *Generalized Thermalization in an Integrable Lattice System*. Phys. Rev. Lett. **106**, 140405 (2011).

[159] J.-S. Caux and F. H. L. Essler. *Time Evolution of Local Observables After Quenching to an Integrable Model*. Phys. Rev. Lett. **110**, 257203 (2013). Cited on page: 49

[160] E. H. Lieb and F. Y. Wu. *Absence of Mott Transition in an Exact Solution of the Short-Range, One-Band Model in One Dimension*. Phys. Rev. Lett. **20**, 1445–1448 (1968). Cited on page: 49

[161] E. H. Lieb and F. Wu. *The one-dimensional Hubbard model: a reminiscence*. Physica A **321**, 1 – 27 (2003). Cited on page: 49

[162] H. A. Bethe. *Zur Theorie der Metalle: I. Eigenwerte und Eigenfunktionen der linearen Atom Kette*. Z. Phys. **71**, 205 – 226 (1931). Cited on page: 49

[163] L. Fleishman and P. W. Anderson. *Interactions and the Anderson transition*. Phys. Rev. B **21**, 2366–2377 (1980). Cited on page: 50

[164] B. L. Altshuler, Y. Gefen, A. Kamenev, and L. S. Levitov. *Quasiparticle Lifetime in a Finite System: A Nonperturbative Approach*. Phys. Rev. Lett. **78**, 2803–2806 (1997).

[165] I. V. Gornyi, A. D. Mirlin, and D. G. Polyakov. *Interacting Electrons in Disordered Wires: Anderson Localization and Low-T Transport*. Phys. Rev. Lett. **95**, 206603 (2005). Cited on page: 50

[166] A. Pal and D. A. Huse. *Many-body localization phase transition*. Phys. Rev. B **82**, 174411 (2010). Cited on pages: 50, 51, 52, 72

[167] B. Swingle. *A simple model of many-body localization*. arXiv:1307.0507 (2013). Cited on page: 50

[168] J. Eisert, M. Cramer, and M. B. Plenio. *Colloquium: Area laws for the entanglement entropy*. Rev. Mod. Phys. **82**, 277–306 (2010). Cited on page: 51

[169] D. J. Luitz, N. Laflorencie, and F. Alet. *Extended slow dynamical regime close to the many-body localization transition*. Phys. Rev. B **93**, 060201 (2016). Cited on pages: 52, 67, 71, 72, 76, 78, 83, 84

[170] D. J. Luitz, N. Laflorencie, and F. Alet. *Many-body localization edge in the random-field Heisenberg chain*. Phys. Rev. B **91**, 081103 (2015). Cited on pages: 52, 58, 72, 76

[171] P. Calabrese and J. Cardy. *Evolution of entanglement entropy in one-dimensional systems*. J. Stat. Mech. **2005**, P04010 (2005). Cited on page: 52

[172] G. D. Chiara, S. Montangero, P. Calabrese, and R. Fazio. *Entanglement entropy dynamics of Heisenberg chains*. J. Stat. Mech. **2006**, P03001 (2006).

[173] H. Kim and D. A. Huse. *Ballistic Spreading of Entanglement in a Diffusive Nonintegrable System*. Phys. Rev. Lett. **111**, 127205 (2013). Cited on page: 52

[174] M. Žnidarič, T. c. v. Prosen, and P. Prelovšek. *Many-body localization in the Heisenberg XXZ magnet in a random field*. Phys. Rev. B **77**, 064426 (2008). Cited on page: 52

[175] J. H. Bardarson, F. Pollmann, and J. E. Moore. *Unbounded Growth of Entanglement in Models of Many-Body Localization*. Phys. Rev. Lett. **109**, 017202 (2012). Cited on pages: 52, 53

[176] P. Jordan and E. Wigner. *Über das Paulische Äquivalenzverbot*. Z. Phys. **47**, 631–651 (1928). Cited on page: 56

[177] P. Prelovšek, O. S. Barišić, and M. Žnidarič. *Absence of full many-body localization in the disordered Hubbard chain*. Phys. Rev. B **94**, 241104 (2016). Cited on pages: 57, 84, 87

[178] I. V. Protopopov, W. W. Ho, and D. A. Abanin. *Effect of SU(2) symmetry on many-body localization and thermalization*. Phys. Rev. B **96**, 041122 (2017). Cited on page: 57

[179] L. Vidmar, S. Langer, I. P. McCulloch, U. Schneider, U. Schollwöck, and F. Heidrich-Meisner. *Sudden expansion of Mott insulators in one dimension*. Phys. Rev. B **88**, 235117 (2013). Cited on page: 59

[180] M. Zwolak and G. Vidal. *Mixed-State Dynamics in One-Dimensional Quantum Lattice Systems: A Time-Dependent Superoperator Renormalization Algorithm*. Phys. Rev. Lett. **93**, 207205 (2004). Cited on page: 61

[181] M. Vojta. *Quantum phase transitions*. Rep. Prog. Phys. **66**, 2069 (2003). Cited on page: 69

[182] L. Zhang, B. Zhao, T. Devakul, and D. A. Huse. *Many-body localization phase transition: A simplified strong-randomness approximate renormalization group*. Phys. Rev. B **93**, 224201 (2016). Cited on page: 69

[183] R. B. Griffiths. *Nonanalytic Behavior Above the Critical Point in a Random Ising Ferromagnet*. Phys. Rev. Lett. **23**, 17–19 (1969). Cited on page: 70

[184] M. Žnidarič, A. Scardicchio, and V. K. Varma. *Diffusive and Subdiffusive Spin Transport in the Ergodic Phase of a Many-Body Localizable System*. Phys. Rev. Lett. **117**, 040601 (2016). Cited on page: 71

[185] I. Khait, S. Gazit, N. Y. Yao, and A. Auerbach. *Spin transport of weakly disordered Heisenberg chain at infinite temperature*. Phys. Rev. B **93**, 224205 (2016). Cited on page: 71

[186] K. Agarwal, S. Gopalakrishnan, M. Knap, M. Müller, and E. Demler. *Anomalous Diffusion and Griffiths Effects Near the Many-Body Localization Transition*. Phys. Rev. Lett. **114**, 160401 (2015). Cited on page: 71

[187] Y. B. Lev, G. Cohen, and D. R. Reichman. *Absence of Diffusion in an Interacting System of Spinless Fermions on a One-Dimensional Disordered Lattice*. Phys. Rev. Lett. **114**, 100601 (2015).

[188] E. J. Torres-Herrera and L. F. Santos. *Dynamics at the many-body localization transition*. Phys. Rev. B **92**, 014208 (2015). Cited on page: 71

[189] J. A. Kjäll, J. H. Bardarson, and F. Pollmann. *Many-Body Localization in a Disordered Quantum Ising Chain*. Phys. Rev. Lett. **113**, 107204 (2014). Cited on page: 72

[190] A. B. Harris. *Effect of random defects on the critical behaviour of Ising models*. J. Phys. C **7**, 1671 (1974). Cited on page: 72

[191] J. T. Chayes, L. Chayes, D. S. Fisher, and T. Spencer. *Finite-Size Scaling and Correlation Lengths for Disordered Systems*. Phys. Rev. Lett. **57**, 2999–3002 (1986).

[192] A. Chandran, C. R. Laumann, and V. Oganesyan. *Finite size scaling bounds on many-body localized phase transitions*. arXiv:1509.04285 (2015). Cited on page: 72

[193] S. Gopalakrishnan, K. Agarwal, E. A. Demler, D. A. Huse, and M. Knap. *Griffiths effects and slow dynamics in nearly many-body localized systems*. Phys. Rev. B **93**, 134206 (2016). Cited on page: 73

[194] M. Mierzejewski, J. Herbrych, and P. Prelovšek. *Universal dynamics of density correlations at the transition to the many-body localized state*. Phys. Rev. B **94**, 224207 (2016). Cited on pages: 75, 77, 80, 82, 86

[195] M. Lee, T. R. Look, S. P. Lim, and D. N. Sheng. *Many-body localization in spin chain systems with quasiperiodic fields*. Phys. Rev. B **96**, 075146 (2017). Cited on pages: 78, 84

[196] M. H. Fischer, M. Maksymenko, and E. Altman. *Dynamics of a Many-Body-Localized System Coupled to a Bath*. Phys. Rev. Lett. **116**, 160401 (2016). Cited on pages: 82, 89, 90, 92, 106, 108, 109, 110

[197] Y. B. Lev, D. M. Kennes, C. Klöckner, D. R. Reichman, and C. Karrasch. *Transport in quasiperiodic interacting systems: From superdiffusion to subdiffusion*. EPL **119**, 37003 (2017). Cited on page: 84

[198] F. Setiawan, D.-L. Deng, and J. H. Pixley. *Transport properties across the many-body localization transition in quasiperiodic and random systems*. Phys. Rev. B **96**, 104205 (2017). Cited on page: 85

[199] E. Leviatan, F. Pollmann, J. H. Bardarson, and E. Altman. *Quantum thermalization dynamics with Matrix-Product States*. arXiv:1702.08894 (2017). Cited on page: 85

[200] R. Nandkishore, S. Gopalakrishnan, and D. A. Huse. *Spectral features of a many-body-localized system weakly coupled to a bath*. Phys. Rev. B **90**, 064203 (2014). Cited on page: 89

[201] S. Gopalakrishnan and R. Nandkishore. *Mean-field theory of nearly many-body localized metals*. Phys. Rev. B **90**, 224203 (2014).

[202] R. Nandkishore. *Many-body localization proximity effect*. Phys. Rev. B **92**, 245141 (2015). Cited on page: 115

[203] S. Johri, R. Nandkishore, and R. N. Bhatt. *Many-Body Localization in Imperfectly Isolated Quantum Systems*. Phys. Rev. Lett. **114**, 117401 (2015).

[204] M. Žnidarič. *Relaxation times of dissipative many-body quantum systems*. Phys. Rev. E **92**, 042143 (2015). Cited on pages: 90, 92

[205] S. Banerjee and E. Altman. *Variable-Range Hopping through Marginally Localized Phonons*. Phys. Rev. Lett. **116**, 116601 (2016).

[206] E. Levi, M. Heyl, I. Lesanovsky, and J. P. Garrahan. *Robustness of Many-Body Localization in the Presence of Dissipation*. Phys. Rev. Lett. **116**, 237203 (2016). Cited on pages: 90, 92

[207] M. V. Medvedyeva, T. c. v. Prosen, and M. Žnidarič. *Influence of dephasing on many-body localization*. Phys. Rev. B **93**, 094205 (2016).

[208] B. Everest, I. Lesanovsky, J. P. Garrahan, and E. Levi. *Role of interactions in a dissipative many-body localized system*. Phys. Rev. B **95**, 024310 (2017). Cited on pages: 89, 90, 92, 106

[209] H. Pichler, J. Schachenmayer, J. Simon, P. Zoller, and A. J. Daley. *Noise- and disorder-resilient optical lattices*. Phys. Rev. A **86**, 051605 (2012). Cited on page: 89

[210] H. Pichler, J. Schachenmayer, A. J. Daley, and P. Zoller. *Heating dynamics of bosonic atoms in a noisy optical lattice*. Phys. Rev. A **87**, 033606 (2013). Cited on page: 89

[211] H. Pichler, A. J. Daley, and P. Zoller. *Nonequilibrium dynamics of bosonic atoms in optical lattices: Decoherence of many-body states due to spontaneous emission*. Phys. Rev. A **82**, 063605 (2010). Cited on pages: 89, 92

[212] F. Gerbier and Y. Castin. *Heating rates for an atom in a far-detuned optical lattice*. Phys. Rev. A **82**, 013615 (2010). Cited on page: 89

[213] A. J. Daley. *Quantum trajectories and open many-body quantum systems*. Adv. Phys. **63**, 77–149 (2014). Cited on page: 90

[214] G. Lindblad. *On the generators of quantum dynamical semigroups*. Commun. Math. Phys. **48**, 119–130 (1976). Cited on page: 92

[215] J. Dalibard, Y. Castin, and K. Mølmer. *Wave-function approach to dissipative processes in quantum optics*. Phys. Rev. Lett. **68**, 580–583 (1992). Cited on page: 92

[216] H. J. Carmichael. *Quantum trajectory theory for cascaded open systems*. Phys. Rev. Lett. **70**, 2273–2276 (1993). Cited on page: 92

[217] E. P. L. van Nieuwenburg, J. Y. Malo, A. J. Daley, and M. H. Fischer. *Dynamics of many-body localization in the presence of particle loss*. arXiv:1706.00788 (2017). Cited on pages: 92, 110, 111

[218] S. Sarkar, S. Langer, J. Schachenmayer, and A. J. Daley. *Light scattering and dissipative dynamics of many fermionic atoms in an optical lattice*. Phys. Rev. A **90**, 023618 (2014). Cited on page: 92

[219] Y. S. Patil, S. Chakram, and M. Vengalattore. *Measurement-Induced Localization of an Ultracold Lattice Gas*. Phys. Rev. Lett. **115**, 140402 (2015). Cited on page: 95

Danksagung

Nach vielen Jahren am Lehrstuhl Bloch möchte ich mich bei allen Personen bedanken, die direkt oder indirekt zum Gelingen dieser Arbeit beigetragen haben. Besonders bedanken möchte ich mich bei

- Prof. Immanuel Bloch für die Möglichkeit an seinem Lehrstuhl zu promovieren, für die exzellenten Bedingungen für wissenschaftliches Arbeiten an seinem Lehrstuhl, für viele spannende und lehrreiche Diskussionen, für die Möglichkeit, unsere Resultate auch auf weit entfernten Konferenzen präsentieren zu dürfen, für die Freiheit, eigene Ideen ausprobieren zu können und dafür, dass er mich mit seiner spannenden Vorlesung über ultrakalte Gase für das Thema begeistert hat.

- Ulrich Schneider für das Angebot in seinem Team arbeiten zu dürfen, für seine anschaulichen Erklärungen, für seine Geduld bei der Korrektur von Veröffentlichungen und für die Zeit, die er für uns verwendet hat, auch nachdem er nach Cambridge gezogen war.

Großer Dank gilt auch meinen Kollegen und Freunden, ohne die die Zeit am Lehrstuhl nicht annähernd so viel Spaß gemacht hätte. Insbesondere bedanke ich mich bei

- Pranjal Bordia, mit dem ich die meiste Zeit zusammengearbeitet habe, für seine Erinnerungen, dass manche Dinge einfach schnell funktionieren müssen. Ohne ihn wären die letzten Jahre deutlich weniger produktiv gewesen.

- Michael Schreiber für die Beantwortung all der technischen Fragen, für seinen Perfektionismus beim Aufbau des Experiments und für seine steten Bemühungen mich mit Junkfood zu mästen.

- Martin Reitter für seine Treue zur Mensa.

- Sebastian Scherg für Skiunterricht und das Versenken von kleinen in großen Gläsern.

- Thomas Kohlert für den gratis Schachunterricht.

- Sean Hodgman für seine tolle Einstellung zu den alltäglichen Problemen der Laborarbeit.

- Moritz Höfer dafür, dass ich nie alleine meckern musste.

- Ildiko Kecskesi für das Lösen aller möglichen und unmöglichen organisatorischen Probleme.

- Bodo Hecker für seine Unterweisungen in der Elektronik, die stets zu den spannendsten Momenten im Laboralltag gehörten.

Außerdem möchte ich mich bei meinen Eltern für alles, was sie für mich getan haben, bedanken. Zu guter Letzt bedanke ich mich bei Klara Malinowska für eine wunderbare gemeinsame Zeit und speziell für die vielen Bergtouren, bei denen ich meine Batterien neu laden konnte.